ResearchGate

See discussions, stats, and author profiles for this publication at: https://www.researchgate.net/publication/326588990

Preliminary Structural Study and Design of the SNC's Dream Chaser

Technical Report · February 2018

CITATIONS
0

READS
6,223

3 authors:

Vittorio Alessandro Del Buono
Università di Pisa

1 PUBLICATION 0 CITATIONS

SEE PROFILE

Francesco Maddaluni
Università di Pisa

2 PUBLICATIONS 1 CITATION

SEE PROFILE

Raffaello Bottai
Università di Pisa

1 PUBLICATION 0 CITATIONS

SEE PROFILE

All content following this page was uploaded by Vittorio Alessandro Del Buono on 25 July 2018.

The user has requested enhancement of the downloaded file.

Università di Pisa
Dipartimento di Ingegneria Civile e Industriale
Corso di Laurea Specialistica in Ingegneria Aerospaziale

Preliminary Structural Evaluation and Design of the *Dream Chaser* lifting-body concept

---

Project Report, Code SSM-35

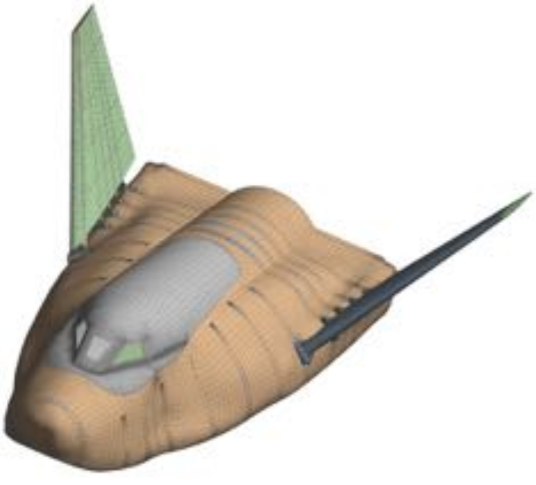

Supervisor:
Prof. Ing. Mario Rosario Chiarelli

Authors:
Raffaello Bottai
Alessandro Del Buono
Francesco Maddaluni

Anno Accademico 2016/2017

Abstract

This report presents a first attempt to provide a preliminary structural evaluation of Sierra Nevada Corporation's (SNC) *Dream Chaser* crewed lifting-body spaceplane, both on the mechanical and technological aspect. Despite the very limited available material, final study results are representative of the expected real structure behaviour for the selected mission loading conditions, such as abort and subsonic aerodynamic maneuver.

Dream Chaser greatest innovation lies in its state-of-the-art concept, which allows unassisted crew egress at any landing site without the need for special equipment. The minimum actions required to quickly remove the vehicle from the runway is enabled by the low toxicity and low hazard levels of the Dream Chaser design, thus minimizing the impact on day-to-day operations at a public-use landing site. Indeed, this cutting-edge characteristic will guarantee SNC to figure prominently on next-generation human/cargo space transportation to low-Earth orbit (LEO) destinations.

Preface presents the project background, as well as the motivations that pushed us to the treatment of such a particular topic. Chapter 1 introduces to the lifting body concept and its main historical milestones that led to the modern Dream Chaser spacecraft development. Chapter 2 provides a detailed description of the vehicle definition from a structural standpoint, categorizing vehicle components of major concern, materials and joint technologies. Chapter 3, instead, shows the first project steps, like informations gathering, first attempts to model the structure geometry and how we jotted down the main study guidelines. Chapter 4 investigates the mission critical loading conditions, where just the most significant are selected as inputs for the design of the vehicle. In Chapter 5, all the analysis methodologies are presented and explained: they consist of a geometrical modeling (for which CATIA V5 R20 was used) and a comparative assessment between structural theory and finite element analysis (FEA) predictions. ANSYS R18.1 MECHANICAL simulation tool was used to perform finite element strength analyses in order to evaluate the integrity of the proposed structural arrangement.
Final chapter is of relevant importance, since the FEA results are promptly discussed and exploited as an aid to detect structural failure regions and criticalities. Some components are optimised in thicknesses, while two improved concepts are proposed for wing-to-fuselage joints and main engines-to-fuselage ribs interfaces.

Contents

1 Introduction **1**
- 1.1 Lifting body historical background . . . 1
  - 1.1.1 Working principle of lifting bodies . . . 3
  - 1.1.2 The lifting body evolution: from NASA M2-F1 to SNC Dream Chaser 4
- 1.2 Dream Chaser state of the art . . . 10
  - 1.2.1 *Dream Chaser Space System* overview . . . 12

2 Vehicle Definition **15**
- 2.1 Concept development philosophy of the HL-20 PLS . . . 15
- 2.2 Dream Chaser structural definition . . . 17
  - 2.2.1 Main features and key subsystems . . . 17
  - 2.2.2 Structural arrangement . . . 19
- 2.3 Our proposal . . . 20
- 2.4 Materials . . . 21
  - 2.4.1 BMI resin . . . 22
  - 2.4.2 Metallic Parts . . . 22
- 2.5 Joints Technology . . . 23

3 Preliminary Studies **25**
- 3.1 Reentry Phase Analysis . . . 26
- 3.2 Preliminary Structural Design . . . 29

4 Vehicle Loading Conditions **33**
- 4.1 Mission Baseline: ISS crew rotation . . . 33
- 4.2 8-g Abort . . . 35
- 4.3 2,5-g Subsonic Aerodynamic Pullup Maneuver . . . 35

5 Structural Analysis **37**
- 5.1 Fundamental Premise to our Approach . . . 37
- 5.2 Geometrical Modeling . . . 38
  - 5.2.1 Primary Structure Components . . . 38
  - 5.2.2 Secondary Structure Components . . . 42
  - 5.2.3 Other Components . . . 44
  - 5.2.4 Fin Structural Design . . . 44

6 Finite Element Analysis **53**
- 6.1 Finite Element Modeling . . . 53
- 6.2 Abort 8g . . . 58
- 6.3 Pullup 2,5g . . . 62
- 6.4 Modal Analysis . . . 67

7 Finite Element Analysis: Optimisation Process 71
7.1 Pressurised Module 71
7.2 Abort 8g 73
7.3 Improved Concepts 78
7.3.1 Thrust Frame 78
7.3.2 Wing Root Fittings 82

8 Conclusions 87

A MATLAB codes 89
A.1 Reentry phase at Mach 10 89
A.2 Preliminary Structural Analysis 92
A.3 Fin Structural Design 94
A.4 Wing Root Fittings Design 98

Bibliografy 100

List of Figures

1.1 Sänger-Bredt Silbervogel spaceplane. 1
1.2 Harry Julian Allen (April 1, 1910 – January 29, 1977). 2
1.3 Alfred J. Eggers Jr. (June 24, 1922 – September 22, 2006). 3
1.4 Graph showing cross range distances in miles plotted against hypersonic lift over drag for several vehicles. Cross-range is an indicator of the achievable landing zone extension, which has a major impact on landing sites that are accessible by the spacecraft on return from orbit. 3
1.5 M2-F1 3-view. 5
1.6 The “flying bathtube" M2-F1. 5
1.7 Three lifting body vehicles at NASA’s Flight Research Center in California in 1969. Left to right: the X-24A, M2-F3, and HL-10. These aircraft helped pave the way for later spaceplane concepts. 6
1.8 X-20 Dyna-Soar specifications (left) and model (right). 6
1.9 Spiral OS 50/50 design and internal structure. 7
1.10 The MIG 105-11. It was nicknamed “Lapot”, or bast shoe for the shape of its nose. 7
1.11 BOR-4 assembling in the factory. 8
1.12 HL-20 design. 8
1.13 The evolution of the HL-20 series. 9
1.14 Dream Chaser Cargo (left) and Space (right) System variants. 11
1.15 ISS Mission Concept of Operations. The Dream Chaser will have frequent deorbit opportunities to landing sites in the United States and the ability to perform runway landings on every orbit during LEO missions. Thus, in case of a medical emergency, the Dream Chaser could land an injured crew member on a runway within a matter of hours. 12
1.16 Details of Dream Chser main mission phases. 13

2.1 HL-20 primary structures (left, crew compartment on top of the heatshield) and subsystem layout (right). 16
2.2 HL-20 cutaway. The crew compartment structural configuration is the result of a study [3] in which it was compared with a “conformal shell" configuration. The performed analyses of both concepts indicate no appreciable weight or load relief advantage of one over the other. Maintainability and operability became therefore the primary discriminator, leading to a choice of a crew compartment configuration. 17
2.3 Dream Chaser cutaway. 19
2.4 Dream Chaser materials setup. 21

3.1 STS-5 reentry parameters as function of elapsed time from reentry. 27

3.2 Body reference frame with positive signs convention at Mach 10 flight regime. 28
3.3 Dream Chaser central structure with pressurized module, body frame and two keel beams [1]. 30
3.4 Model of the central body structure (beams mounted symmetrically with respect to the vertical axis. 30

4.1 Load conditions of the ISS crew rotation baseline mission. 34
4.2 Loading condition during 2.5 g pullup maneuver (adapted from [3]). 36

5.1 Pressurised Module rendering (left) vs. real manufactured piece after curing (right). 39
5.2 Fuselage rib n°6 (left) and 10 (right). 40
5.3 Representation of fuselage skin reference splines. 40
5.4 Primary structure frame assembly (ribs+keel beams). 41
5.5 Scheme of fin's geometry and inner structure (without ribs). 42
5.6 Fin root section geometry. 43
5.7 Beam model of the fin with total lift applied at half of wingspan. 45
5.8 idealized root section of the fin symmetric along x 45
5.9 forces due to ending acting on each boom 46
5.10 schematic draw of attachment system on fin spar with load path from spar to bolts 50
5.11 Renderings of entire wing and spar root fittings. 52

6.1 Final mesh for our Dream Chaser concept (fuselage skin is not showed). . . . 56
6.2 *Abort 8g - global.* 56
6.3 *Abort 8g - local.* 57
6.4 *Pullup 2,5g - global.* 57
6.5 *Pullup 2,5g - local.* 58
6.6 *Pullup 2,5g - local (fin root fittings detail).* 58
6.7 Abort 8g global model - analysis setup (constraints + loads). 59
6.8 Abort 8g global model - deformation patterns. Maximum deflection corresponds to a 5 mm fuselage skin deformation near the thrust point of application. This is due to load transfer from tanks to skin through rib deformation. . . . 59
6.9 Abort 8g global model - equivalent stress patterns. Maximum stress is 272 MPa inside the tanks. 60
6.10 Abort 8g local model - deformation patterns. 61
6.11 Abort 8g local model - equivalent stress patterns. 61
6.12 Pullup 2,5g global model - analysis setup (constraints + loads). 62
6.13 Pullup 2,5g global model - deformation patterns. Max displacement occurs at fins tip, as expected. The figure shows both deformed and undeformed structure shapes to better understand the overall deflections. 63
6.14 Pullup 2,5g global model - deformation patterns (lateral view). 63
6.15 Pullup 2,5g global model - equivalent stress patterns. As expected, again, both fins and fuselage try to strain similarly to a cantilever beam, meaning that bending is the primary cause of deformation critically affecting the structure strength, particularly at the root fittings, where maximum stress of 353 MPa occurs. 64
6.16 Pullup 2,5g local model - deformation patterns. 65
6.17 Pullup 2,5g local model - equivalent stress patterns. 65
6.18 Pullup 2,5g local model - equivalent stress patterns (fittings detail). 66
6.19 Pullup 2,5g local model - equivalent stress patterns (spars caps detail). 66

6.20 Pullup 2,5g local model - fin equivalent stress field. 67
6.21 Pullup 2,5g local model - fin root fitting equivalent stress distribution. 67
6.22 Main mode shapes of main body. 69
6.23 Main mode shapes of fin. 70

7.1 Step 1, 7 mm. 71
7.2 Step 2, 9 mm. 72
7.3 Step 3, 9 mm plus ribs and keel beam. 72
7.4 Abort 8g local model - deformation patterns for 9 mm thickness. 73
7.5 Abort 8g local model - stress patterns for 9 mm thickness 74
7.6 Abort 8g local model - deformation patterns for 11 mm thickness. 74
7.7 Abort 8g local model - stress patterns for 11 mm thickness 75
7.8 Abort 8g local model - detail of stress patterns for 11 mm thickness 75
7.9 Abort 8g local model - diagonal rods layout. 76
7.10 Abort 8g local model - deformation patterns with diagonal rods frame. 76
7.11 Abort 8g local model - equivalent stress patterns with diagonal rods frame. . 77
7.12 Abort 8g local model - direct stress patterns on diagonal rods. 77
7.13 Abort 8g local model - equivalent stress patterns with diagonal rods frame (detail). 77
7.14 Rendering of the Thrust Frame concept. 79
7.15 Lateral view with visible holes on the frames that allow the passage of the diagonal rod. 79
7.16 Top view of the Thrust Frame area. 79
7.17 Schematic view of the forces acting on each part of the Thrust Frame during firing of the engine (only one side shown). Letters A, B, C represents points of attachments between rods and pressurized module 80
7.18 Root bulkhead concept with view of its components (spar sockets not drawn) 82
7.19 Views of loads acting on bulkhead assembly and on junction plates 83
7.20 Representation of force components acting on a fuselage rib lug 83

8.1 Dream Chaser Abort scenarios with possible failures that may cause launch abort and where it could verify along ascent trajectory (adapted from [8]) . . 87

List of Tables

3.1 ISA atmospheric data at 53 250 m. 26
3.2 Results of the reentry phase analysis 29
3.3 Principal dimensions of central structure model. 31
3.4 Results of wall thicknesses of modeled cross-section members. 32

5.1 Fin main geometrical data. 43
5.2 Dimensions of fin root section (wall length are referred to the symmetric upper part of the airfoil). 43
5.3 results of boom area sizing with forces acting on them and cross section dimensions of each spar caps 47
5.4 Output of the iterative procedure and actual thicknesses of spar webs and skin. 48
5.5 Results of fitting interfaces design. 52

6.1 List of material used in structural analyses 54
6.2 Modal analysis results for main body 68
6.3 Modal analysis results for fin. 68

7.1 Pressurised Module sizing loops for thickness and allowable strength evaluation. *Step 3 includes the assembly of fuselage ribs and keel beams. 73

Foreword

The present report is the conclusion of five months of hard work in the effort of **providing a preliminary but faithful structural evaluation and design of the Dream Chaser Space System lifting-body spacecraft**. This project is part of the SPACECRAFT STRUCTURE AND MECHANISMS subject under the Master's Degree course of Aerospace Engineering at the University of Pisa (Italy).
As young students, we were very fascinated by this innovative manned spacecraft concept, a unique and exciting piece of hardware embracing all the fields of engineering. Since the very beginning, we were very keen to study the unconventional shape of the Dream Chaser, understand how it works, and how can such a structure withstand the harsh space environment, especially during hypersonic reentry.

Our persistent obstacle was the lack of reference material, since Dream Chaser is currently under development (the latest glide test took place on November 11, 2017) and it is owned by a private American firm, Sierra Nevada Corporation (therefore all the related specifications are classified). This fact forced us to propose the entire vehicle as the target of our study, and adopt a kind of work-in-progress reverse engineering approach as few and not detailed informations were gradually released to the public. However, few articles and papers were found regarding Dream Chaser design "forerunner", the HL-20 Personnel Launch System. On this base, we started developing our work and we focused on modeling the vehicle structural arrangement. Further findings helped us in shaping its external skin, whereas for the canted fins (the protruding wings) definition we had to rely on conventional aeronautic structural solutions. Anyway, our final results are encouraging, since we managed to figure out how Dream Chaser is made, especially guessing how inner components are interfaced to one another.

The Dream Chaser spacecraft is a multifunctional device for space applications. It is being designed as a multi-mission space utility vehicle that is able to operate as an independent science platform, logistics enabler or orbital servicing vehicle with the ability to deploy, retrieve, repair, refuel or assemble items in space. To support these missions, Dream Chaser can be customized through vehicle configuration, launch site, destination, landing site, duration and a host of other variables.
We do believe Dream Chaser will represent the future of human space transportation, because of its versatility and affordability. Its lifting body design is definitely a way above typical capsule-like configurations, because it offers enhanced abort, reentry and aerodynamic maneuvers capabilities and control. Nevertheless, this kind of vehicle can land anywhere is demanded, even on commercial runways, and immediate access can be performed because of its all non-toxic propellants.
Dream Chaser is born to push forward the boundaries of human endeavours in space, serving the needs of global science and commercial research industries, as well as, the economic development strategies for both international and industry participants. Likely, it will become NASA's primary cargo transportation vehicle to low-Earth orbit as of late 2021.

Chapter 1

Introduction

With the retirement of the Space Shuttle program in 2011, the United States currently does not have its own means of transporting crew into low-Earth orbit (LEO), including the International Space Station (ISS). Sierra Nevada Corp.'s (SNC) *Dream Chaser* is the best solution to this challenge because of its affordability, flexibility, safety, and extensive capabilities that don't exist anywhere else in the world. It offers NASA safe and affordable human access to the ISS for crew and critical cargo transportation. It also offers multi-mission applications, such as orbital science and research, spacecraft repair and retrieval for civil and commercial customers around the world. Essentially, Dream Chaser will help open space for many commercial markets.

The purpose of this chapter is to frame the context of the topic of our report. We present and explain how lifting bodies work, walking us through the main historical milestones that led to the Dream Chaser development. We further provide an overview of the Dream Chaser spacecraft state of the art.

1.1 Lifting body historical background

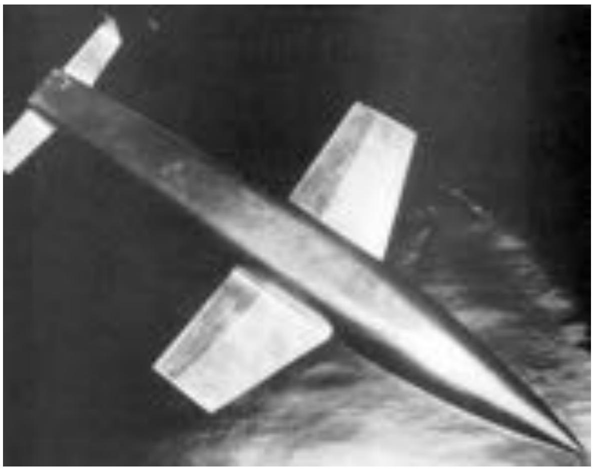

Figure 1.1: Sänger-Bredt Silbervogel spaceplane.

The problem of reentry from space has always been the most important and vexing challenge in the rigorous effort to bring spacecrafts and their crews and cargo home successfully.

Apparently, Dr. ***Eugen Sänger*** (September 22, 1905 – February 10, 1964) had first proposed the concept of a lifting body as early as 1933, remarkably exploited by the suborbital bomber *Silbervogel* ("Silverbird") concept of World War II (see Fig.1.1). Sänger argued that a flat-bottom lifting body would have a higher lift-to-drag ratio (L/D coefficient) at high supersonic speeds than a normal-shape aircraft of similar size. However, he did not pursue this concept to the extent of determining the optimum shape for a lifting body, nor did he prove that such a vehicle should necessarily have a flat bottom.

In the immediate postwar era, three basic vehicle types were being considered for high-speed global flight: *ballistic*, *boost-glide*, and *skip-glide.*

The ballistic vehicle, best exemplified by the long-range missile, leaves the atmosphere and returns as a single maneuver, generally in the form of a parabola. A boost-glider is accelerated to a speed and altitude where the dynamic pressure allows the vehicle to glide at some given L/D coefficient. At this altitude, termed by Sänger the "equilibrium altitude", the aerodynamic lift required for flight is less than the centrifugal force resulting from the curved flight around Earth. The required aerodynamic lift lessens as speed increases, and it becomes zero at orbital velocities. Once at the equilibrium altitude, the vehicle maintains its maximum L/D until aerodynamic drag causes it to slow and lose altitude until it lands.

On the other hand, the trajectory of a skip-glider (such as the Sänger Silverbird) is composed of a succession of ballistic paths, each connected to the next by a skipping phase during which the vehicle enters the atmosphere, negotiates a turn at some given L/D coefficient, and is ejected from the atmosphere by aerodynamic lift. Each upward skip results in a lower peak altitude than the last since the vehicle is unpowered, and this sequence continues until the vehicle no longer has sufficient energy to leave the sensible atmosphere, at which time it glides to a landing.

Early in 1954, ***H. Julian Allen***, ***Alfred J. Eggers Jr.*** and ***Stanford E. Neice*** at the NACA Ames Aeronautical Laboratory put together a theoretical discussion of these different concepts. While they were investigating, Allen compared the likely structural weights of each vehicle. He noted that the apparent advantage of the ballistic missile (a lack of wings) was largely negated by the need for increased propellant tankage since the vehicle could not rely on aerodynamic lift at any point in its trajectory. The ballistic vehicle also experienced the highest aerodynamic loads while entering the atmosphere, adversely affecting structural weight (although the skip-glider suffered a similar flaw). In this regard, a boost-glider, or spaceplane, was the most efficient configuration in terms of structural weight, assuming a suitable, lightweight thermal protection system could be found.

Figure 1.2: Harry Julian Allen (April 1, 1910 – January 29, 1977).

The researchers noted that the three vehicle types reacted to entry heating in vastly different ways. The *blunt-body theory* made it possible to design a ballistic reentry vehicle because the majority of the heat was carried away from the vehicle by shock waves and other aerodynamic phenomena; heat sinks or ablators could handle the residual heat. Obviously, this was impractical for both of the glide vehicles since, by definition, a glider needs a high L/D to increase its range and avoid plunging through the atmosphere. However, a boost-glider could gradually convert its kinetic energy over a longer time than a capsule, radiating much of the heat back into the atmosphere and maintaining comparatively low structural temperatures. Testing by Allen and Eggers revealed that with sufficiently low wing loading, it might be possible to build a glider that could radiate enough heat to maintain a structural temperature under 870 °C, which was within the capability of some available materials. The wing loading had to be kept low since increasing it adversely affected the radiation-equilibrium temperature, resulting in large wings and more thermal protection. Active cooling systems could be employed at the hot spots (nose, wing leading edge, etc.), where the equilibrium temperature exceeded the tolerance of available materials. The skip-glider, on the other hand, seemed to be unworkable. A large fraction of the kinetic energy was converted to heat in a short time during each skip, but the interval between skips was not sufficient to radiate the heat into space. Eggers determined that any skip-glider would need to use an extensive active cooling system, and the weight penalty would probably be so excessive as to rule this vehicle out as impractical, or even impossible, except for very short flights.

Figure 1.3: Alfred J. Eggers Jr. (June 24, 1922 – September 22, 2006).

Despite having discovered the blunt-body theory that made ballistic reentry possible, Eggers became convinced of the overall desirability of a lifting reentry vehicle instead of a ballistic capsule. He was skeptical about the relatively high heating loads and deceleration forces characteristic of ballistic reentry, warning that “the g’s are sufficiently high to require that extreme care be given to the support of an occupant of a ballistic vehicle during atmospheric reentry.” He also pointed out that such an object, entering the atmosphere along a shallow trajectory to hold deceleration down to 7,5 g’s, would generate a surface temperature of at least 1370 °C. Thus, in Eggers’s judgement, “the glide vehicle is generally better suited than the ballistic vehicle for manned flight”. He also saw the difficulty of recovering a ballistic capsule since it was not controllable in the atmosphere and might need a target area of several thousand square kilometers. Of course, several of these challenges were subsequently overcome by providing a small amount of lift, and developing better ablators, for the capsules.

1.1.1 Working principle of lifting bodies

During a lifting reentry, a vehicle generates lift perpendicular to its flight-path, which can then be adjusted to change both vertical motion and flight direction. Practical entry angles have an upper and lower limit. The lower limit, also called the *overshoot boundary*, is the angle at which the vehicle will skip back out of the atmosphere. The upper limit, or *undershoot boundary*, is the load-factor limit established by vehicle-structural, human-tolerance, or operational considerations.

The primary measure for lifting reentry is the **hypersonic lift-to-drag ratio** or L/D ratio. Increasing the L/D has significant effects on decreasing the maximum entry load and increasing the allowable entry corridor depth. Low L/D values (0,5–1,0) produce durations essentially the same as a semiballistic reentry, with survivable g-loads, moderate heating levels, and low maneuverability. Increasing the hypersonic L/D above 1,0 brings only marginal improve-

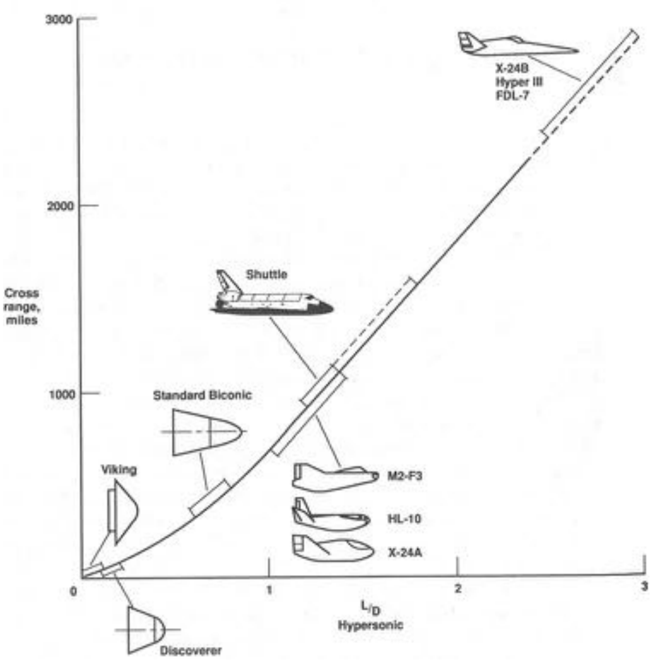

Figure 1.4: Graph showing cross range distances in miles plotted against hypersonic lift over drag for several vehicles. Cross-range is an indicator of the achievable landing zone extension, which has a major impact on landing sites that are accessible by the spacecraft on return from orbit.

ments in entry loads, but extends the cross range as a nonlinear function of the L/D (an L/D of 1,5 might generate a 1600 km cross range, but an L/D of 3 will generate a 6400 km cross range, see Fig. 1.4). High L/D values produce low g-loads and allow significant variations in the flightpath, but they result in long-duration reentries with continuous heating. Although the peak temperatures of a lifting reentry are lower than those of a ballistic reentry, the total heat load (temperature multiplied by duration) is generally higher.

Researchers expected that a spaceplane would land on a preselected runway, like an airplane, and would not require a large recovery force, like capsules. Theoretical and wind tunnel studies, however, showed the aerodynamic configurations that produced the highest L/D during entry did not necessarily produce a high L/D at landing speeds. Long slender cones or wedges without wings were ideal for entry, but the best landing configurations used long, glider-like wings. Engineers soon discovered that by providing two flight modes, one for hypersonic velocities through the transition to subsonic flight, and another for landing, many of the flight-control problems of a spaceplane could be decoupled. Since the majority entry occurs at hypersonic speeds, the engineers decided to concentrate on developing shapes that exhibited adequate stability and control at high speeds, and then they would add the equipment for the decoupled landing mode. A delta wing provided this kind of compromise, but unfortunately thermal protection systems for a spaceplane were a great deal more challenging than for capsules due to the higher total heat load generated by the longer entry time. At the same time, the large surface of the delta wing further exacerbated matters. Needing to maintain a smooth aerodynamic surface added yet another complication.

In spite of any perceived drawbacks, lifting reentry spaceplanes capable of landing on a normal runway were considered necessary to increase human access to space at a reasonable cost, and became the Holy Grail of the aerospace industry. At the time, NASA officials compared the space program's traditional use of expendable launch vehicles with capsules atop to throwing away a rail-road locomotive after every train trip, whereas a reusable spaceplane would offer cost-effective, routine access to space.

1.1.2 The lifting body evolution: from NASA M2-F1 to SNC Dream Chaser

In 1954, ***Meyer M. Resnikoff*** at NACA Ames began looking at the earlier work by Sänger and determined that a lifting body would enjoy a 40 to 100% advantage in L/D over a conventional aircraft at hypersonic velocities. Lacking access to a hypersonic wind tunnel, the study was based instead on formulas derived from Sir Isaac Newton's impact theory.
Resnikoff concluded that "the lower surface of such a body must be flat (thus verifying Sänger's speculation) and rectangular, and that if the maximum available volume is utilized, the minimum drag body... is a wedge".

In March 1958, the winged-craft proposal was overshadowed in favour of capsule-configuration because of the insufficient throw-weight capability of Redstone and Atlas boosters. Nevertheless, the lifting body concept attracted the Air Force, which was interested in a maneuverable intercontinental ballistic missile (ICBM) warhead that could reduce the effectiveness of any antiballistic missile system. The ability of landing in a preselected lauch site away from "prying eyes" was just what a lifting body could offer.
In addition, a lifting body provided a large internal volume compared to a capsule or wing-body shape. However, this would prove misleading because much of the volume was composed of areas with complex curves that did not lend themselves to being efficiently filled with normally square (cube) equipment. Even propellant tanks presented a challenge since they needed

to be odd shapes (often a difficult proposition with cryogenic or high-pressure storage vessels). Ultimately, packaging equipment effectively into a lifting body proved challenging both conceptually and practically.

The pioneering M2-F1

All the efforts and studies by Eggers, Allen, and their associates led to the design known as the *M1* (“M" for “Manned”), a modified 13° half-cone, rounded on the bottom and flat on top, with a blunt, rounded nose to reduce heating. The shape had a hypersonic L/D of 0,5 (only marginally better than a ballistic blunt-body capsule) and demonstrated a pronounced tendency to tumble end over end at subsonic speeds. This design gradually morphed into a blunted 26° cone that offered improved stability, and it became the *M2* shape. Further flattening of the cone top provided additional lift and a hypersonic L/D of 1,4.

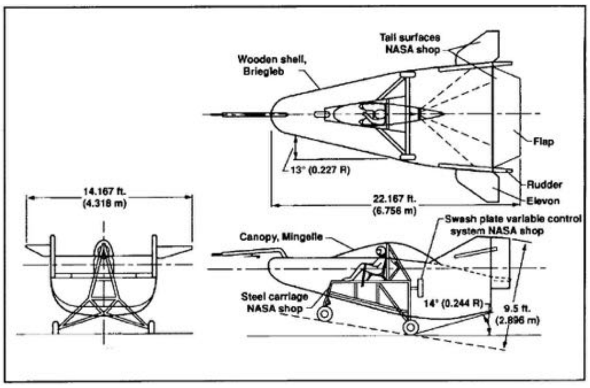

Figure 1.5: M2-F1 3-view.

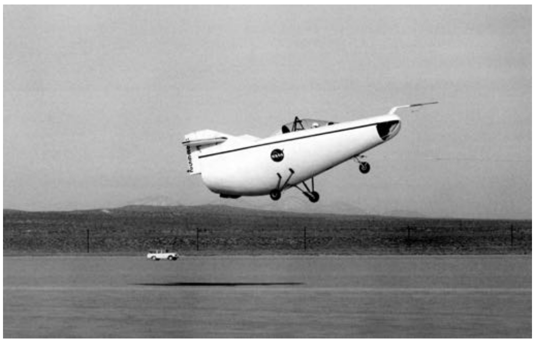

Figure 1.6: The “flying bathtube" M2-F1.

The **world’s first manned *M2-F1*** (Manned 2 - Flight 1) **lifting body** construction was completed in 1963: it featured a plywood shell placed over a tubular steel frame, looked like a bathtub sitting on a tricycle, and had no wings, just a pair of twin tail-fins (see Fig.s 1.5 and 1.6).

R. Dale Reed was a prime mover of the prototype lightweight M2-F1, since he actually was the enigineer who first presented the idea of flight-testing the concept to other at the NASA Dryden Flight Research Center. Thanks to him, 400 ground tows and 77 aircraft tow flights were successfully performed by M2-F1. Benefits from this effort immediately influenced the design and operational concepts of the winged NASA Shuttle Orbiter.
Its configuration and those of the later lifting bodies (see Fig. 1.7) allowed them to be maneuvered both in a lateral and a longitudinal direction, so they could be landed on a runway rather than simply parachuting into the ocean as did the contemporary ballistic capsules used in the Mercury, Gemini, and Apollo programs.

The X-20 Dyna-Soar

The U.S. Air Force transformed the 1930s spaceplane concepts of Eugen Sänger and others into an experimental vehicle: the *X-20 Dyna-Soar* (Dynamic Soaring). Had it flown, it might have been useful for reconnaissance and long-range bombing from the edge of space. Research on the piloted spaceplane lasted from 1957 to 1963, when the program was canceled before

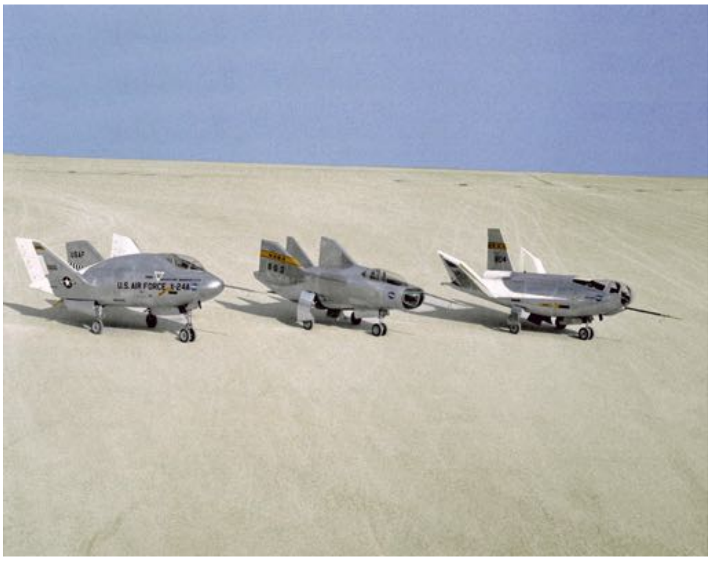
U.S. AIR FORCE X-24A

Figure 1.7: Three lifting body vehicles at NASA's Flight Research Center in California in 1969. Left to right: the X-24A, M2-F3, and HL-10. These aircraft helped pave the way for later spaceplane concepts.

the first vehicle ever flew.

Dyna-Soar was the first serious attempt to build a piloted, reusable, lifting reentry spacecraft, and it began before Project Mercury had taken flight. Most in the industry considered the capsule concept crude, while Dyna-Soar was perceived as elegant since it was maneuverable, reusable, and landed on a runway like an airplane. It was also vastly more complicated and required substantially more research, particularly in the area of thermal protection systems.

The wing on early Dyna-Soar configurations used a double-wedge upper surface with a flat bottom that provided good hypersonic stability and was easy to manufacture. Unfortunately, this design required the addition of retractable stabilizers for low-speed flight, so the upper wing surface was modified to improve low-speed handling without compromising hypersonic stability. This modification, however, resulted in some transonic instabilities that were eliminated by adding an aft fuselage ramp, giving the final Dyna-Soar its distinctive appearance (see Fig. 1.8).

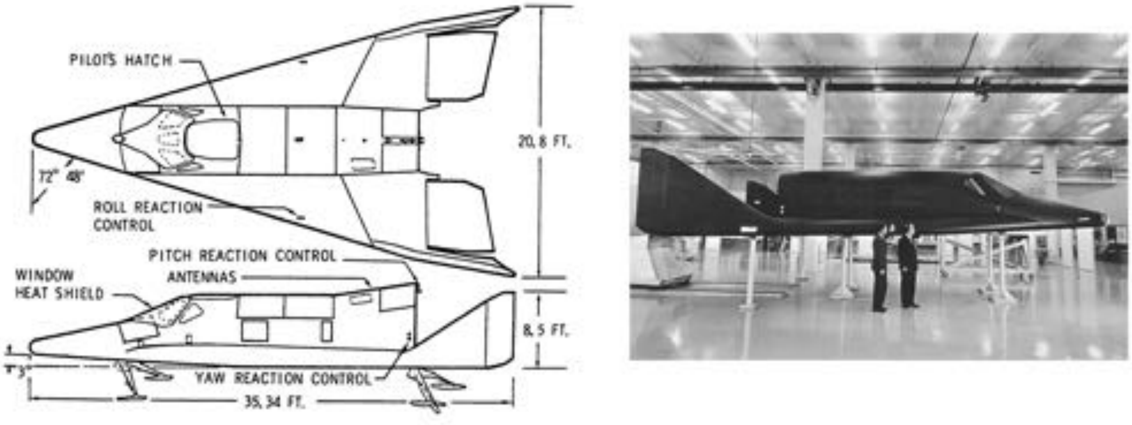
PILOT'S HATCH
72° 48'
ROLL REACTION CONTROL
20.8 FT.
PITCH REACTION CONTROL
ANTENNAS
WINDOW HEAT SHIELD
8.5 FT.
YAW REACTION CONTROL
35.34 FT.

Figure 1.8: X-20 Dyna-Soar specifications (left) and model (right).

The Russian front of lifting body research

At that time, the Soviets put as well lots of efforts in the study of lifting bodies spacecraft architecture. From 1965 to 1976, the Soviet Air Force launched the ambitious *SPIRAL OS 50/50* project as a direct response to the American X-20 Dyna Soar. However, the program, also known as EPOS (Russian acronym for Experimental Passenger Orbital Aircraft), was never properly funded by the government, and by the mid-1970's had only reached the stage of flight tests of subscale versions of Spiral.
The only Spiral full scale product was the *Mikoyan-Gurevich MiG-105-11* manned test vehicle, meant to explore low-speed handling and landing (see Fig. 1.10). Flight tests, totaling eight in all, continued sporadically until 1978. The actual spaceplane project was cancelled when the decision was made to instead proceed with the Buran project.

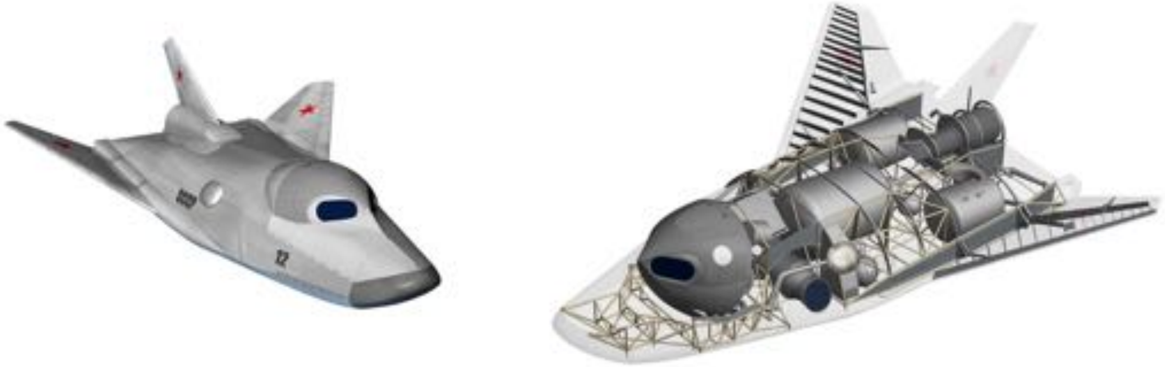

Figure 1.9: Spiral OS 50/50 design and internal structure.

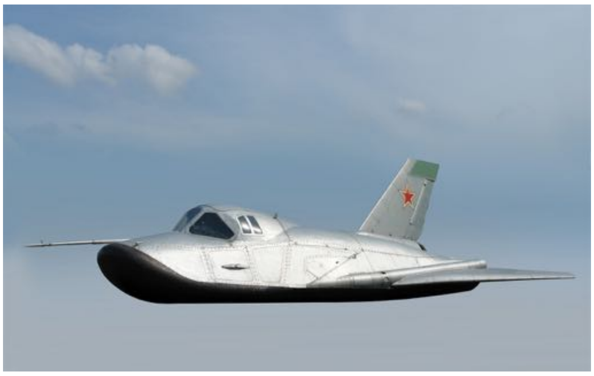

Figure 1.10: The MIG 105-11. It was nicknamed "Lapot", or bast shoe for the shape of its nose.

It is important to outline the fact, in opposition to Dyna-Soar, **Spiral was not a lifting body**: it was a conventional delta that featured an innovative variable-dihedral wing. During launch and reentry, these were folded upward at 60°. After dropping to subsonic speeds post-reentry, the pilot lowered the wings into the horizontal position, giving the spaceplane better re-entry and flight characteristics.
Another different trait concerned the launch configuration: while X-20 Dyna Soar was designed for launch atop a conventional expendable rocket such as the Titan III-C or Saturn I, Soviet engineers opted for a midair launch scheme for Spiral. The idea was that the spaceplane and a liquid fuel booster stage would be launched at high altitude from the back of a custom-built hypersonic jet. The mothership, however, was never built.

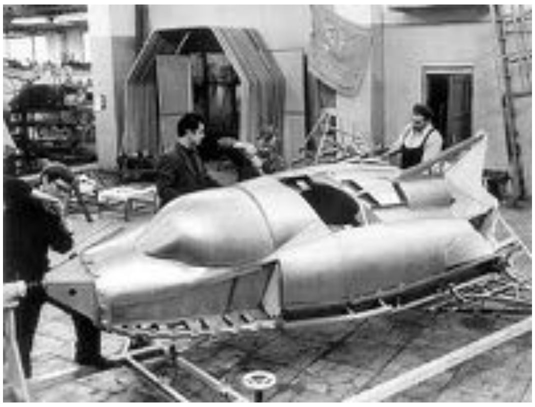

Figure 1.11: BOR-4 assembling in the factory.

During the first part of 80's the Lapot concretized into a real spacecraft with the advent of the *BOR-4* subscale unmanned program. This lifting body spaceplane was built to validate the heat shield design and materials of the ongoing Buran OS (first flight took place in December 5, 1980). The dimensions of the BOR-4 nose corresponded almost with those of Buran; moreover, it is being a counterpart of the Spiral lifting body at the 1:2 scale in regards of the fuselage. The wings of BOR-4, just as that the Spiral, ones could be turned along a radial axis; besides, the fold angle defined the angle of attack for which the lifting body is stable during the re-entry.
The fact of having directional wings was a real innovation for the 60's, because that made it possible to reduce the angle of attack and the heating on the nose and the leading edge of the wings (thus proving the lifting body concept).

The odd shape of Bor-4 attracted the NASA Langley designer and influenced them during the design development of a new transportation vehicle called *PLS* (Personnel Launch System) in mid 80's that later become *HL-20* (Horizontal Landing 20, no connection with the previous NASA program HL-10 of late 60's).

The born of Dream Chaser

Originally proposed as Shuttle replacement to serve the upcoming Freedom Space Station, the development of HL-20 lasted from 1989 to 1993 and ended without any real hardware but a full scale mock-up realized jointly by NASA, North Carolina State University and North Carolina A&T University during 1990.

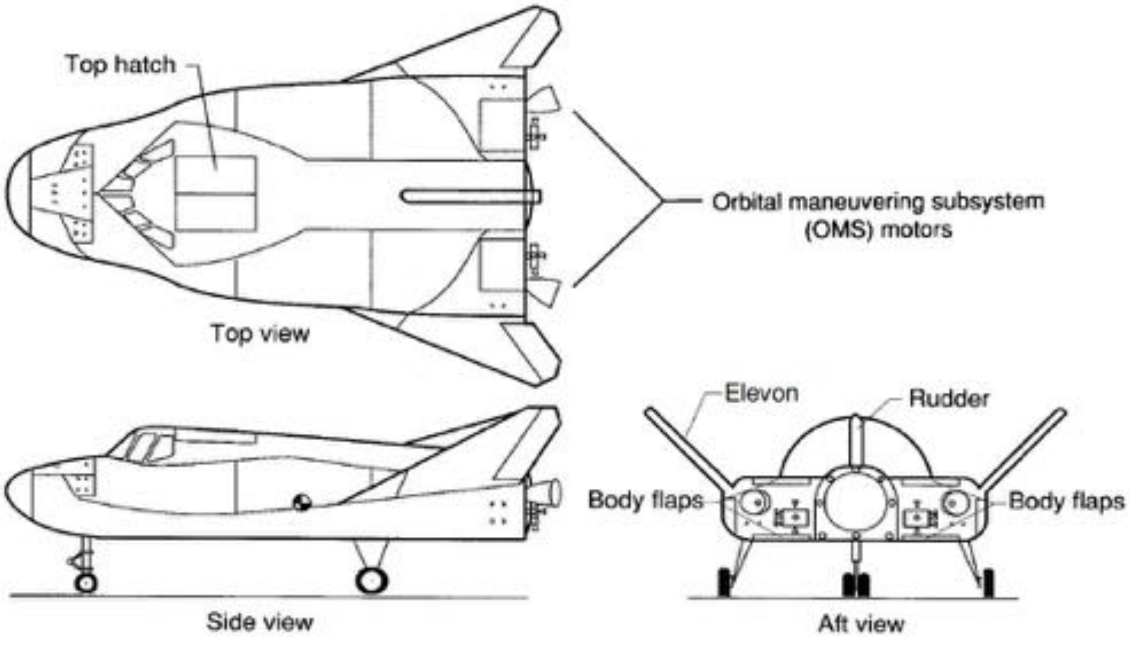

Figure 1.12: HL-20 design.

The HL-20 baseline design (see Fig. 1.12) was a 9000 kg lifting body with a maximum subsonic L/D of 4,3 that was capable of being launched vertically atop an expendable launch vehicle and could be landed horizontally following reentry. The vehicle was designed to carry a crew of two and up to eight passengers to and from LEO, with both manned and automatic landing capabilities implemented. During its development, aerodynamic refinements were made to increase subsonic L/D ratios [6] in order to improve on-pad abort capabilities, as acceleration levels on the order of 8g's were required to propel the vehicle a safe distance away from a malfunctioning booster. These and other interventions led to a final mockup total mass of about 11.000 kg (+22%), with enhanced pad abort-to-runway horizontal landing capability.

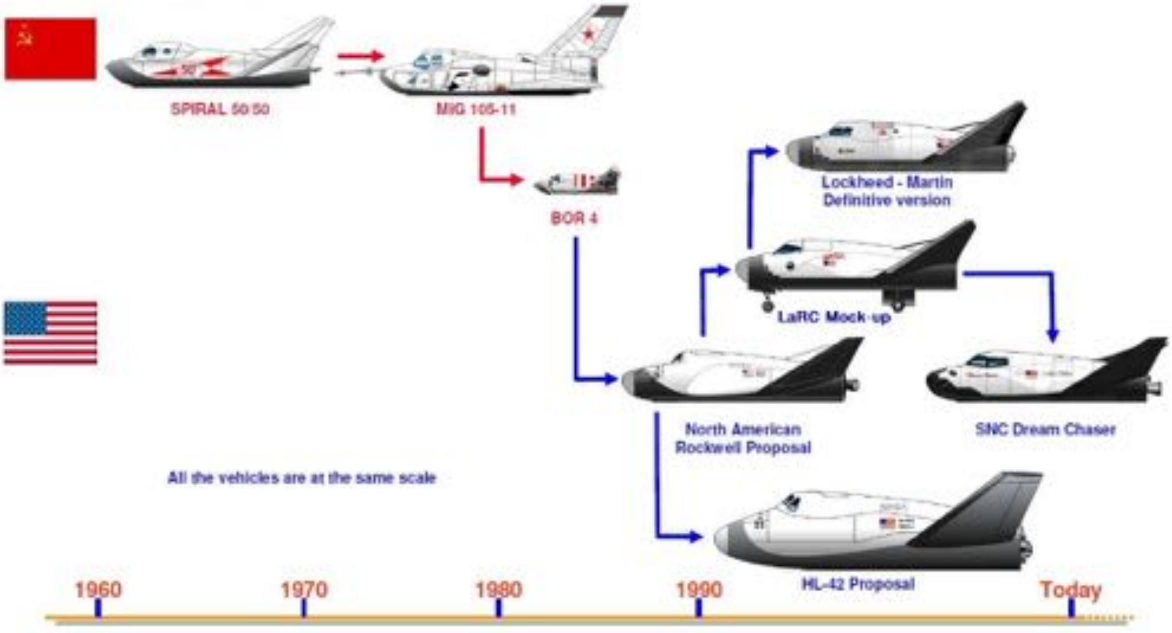

Figure 1.13: The evolution of the HL-20 series.

However, the HL-20 story was no to end, since on September 20, 2004, ***Jim Benson*** announced that the HL-20 development would be continued by his SpaceDev as *Dream Chaser* spacecraft. In 2006 SpaceDev signed a licensing agreement with NASA to reuse HL-20 for the Dream Chaser concept. Despite the agency heritage, SpaceDev failed to get funding under the initial NASA Commercial Orbital Transportation Systems (COTS) program to fund commercial spacecraft. SpaceDev, however, continued work with NASA under a non-reimbursable Space Act agreement in 2007. That same year, it signed a memorandum of understanding with United Launch Alliance (ULA) to put Dream Chaser on an Atlas V rocket. About two weeks after Benson's October 10, 2008 death, SpaceDev agreed to be acquired by Sierra Nevada Corporation, a privately owned company operated by Fatih Ozmen and Eren Ozmen, on October 21, 2008 for $38 million.

On February 1, 2010, SNC was awarded $20 million, the largest share of funds, under NASA's Commercial Crew Development (CCDev) phase 1 program for the development of the Dream Chaser. On April 18, 2011, NASA awarded nearly $270 million in funding for CCDev 2, including $80 million to Sierra Nevada Corporation for Dream Chaser. On August 3, 2012, NASA announced the award of $212.5 million to Sierra Nevada to continue work on the Dream Chaser under the Commercial Crew Integrated Capability (CCiCAP) Program. In April 2012 Sierra Nevada started the aerodynamical trials with a full scale prototype of the Dream Chaser, the ETA (Engineering Test Article) which its function is quite similar to the

Shuttle Enterprise back in mid 70's.

2014: the Dream Chaser deadlock and quick recovery

On September 16, 2014, NASA announced the next and final phase of the commercial spaceflight program would see SpaceX's Dragon and Boeing's CST-100 spacecraft funded for the Commercial Crew Transportation Capability (CCtCap). The Dream Chaser was not selected, due to lack of maturity. Sierra Nevada filed a protest (September 26, 2014) to the US Government Accountability Office (GAO), that temporarily halted work on commercial crew endeavors to wait for the protest resolution. However, on October 22, 2014, a Federal Judge ruled that NASA could proceed with contracts with Boeing and SpaceX to develop their "space taxis", while the GAO continued to consider Sierra Nevada's protest of NASA's original decision. Despite having lost the competition, SNC announced two weeks later the procecution of Dream Chaser development efforts by accomplishing next milestones under earlier phases of the Commercial Crew Program.

In December 2014, Sierra Nevada proposed Dream Chaser for Commercial Resupply Services 2 (CRS-2) consideration. It is in competition with the existing CRS-1 contract holders SpaceX Dragon capsule and Orbital Sciences Cygnus capsule, as well as fellow CCDev competitor Boeing CST-100. In January 2016, NASA announced that Dream Chaser had been awarded one of the contracts under CRS2. NASA committed to purchasing a minimum of six resupply missions to the ISS from Sierra Nevada. In July 2017, Sierra Nevada Corp. and United Launch Alliance signed an agreement to fly Dream Chaser to the ISS on Atlas V rockets. The first two flights (the ones covered under the agreement) are expected in 2020 and 2021. Finally, the United Nations Office for Outer Space Affairs (UNOOSA), which has never launched a space mission of its own, selected the cargo Dream Chaser for at least one mission for United Nations member states that have no space access or space programs of their own. The mission would last for at least two weeks in freeflight, to allow the payloads a microgravity environment, without docking with the International Space Station. The proposed mission would launch as soon as 2021.

It took a very long road to the realisation of such a small spaceplane, but thanks to it the spaceplane family has not gone with the Shuttle retirement in July 2011.

1.2 Dream Chaser state of the art

SNC's change of direction after 2014 deadlock have led to two main Dream Chaser concept variants:

- **Dream Chaser® Cargo System** (uncrewed)
- **Dream Chaser Space System** (crewed)

Although sharing the same structure and thermal protection system (TPS), there exist substantial differences between the two versions: the Dream Chaser Cargo System features an expendable cargo portion, containing solar panels, and it is designed to deliver up to 5500 kg of pressurized and unpressurized cargo to the ISS with the ability to conduct orbital disposal services and responsively return pressurized cargo (up to 1750 kg) at less than 1,5 g's to a gentle runway landing.

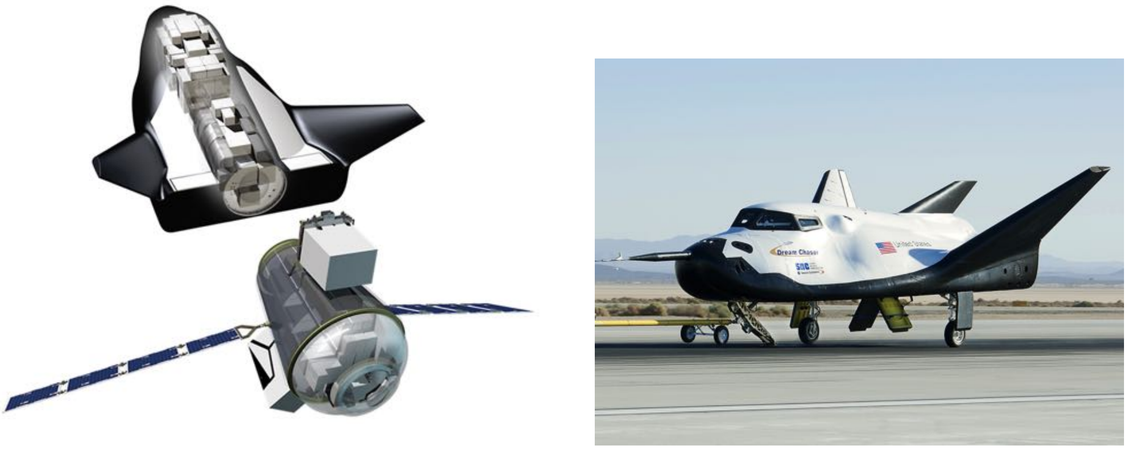

Figure 1.14: Dream Chaser Cargo (left) and Space (right) System variants.

Dream Chaser Cargo System specific features include:

- *Disposable cargo module* that attaches to the Dream Chaser vehicle, greatly increasing the amount of upmass pressurized and unpressurized cargo that can be carried
- *Innovative folding-wing design* allows the uncrewed Dream Chaser spacecraft to fit inside existing standard launch vehicle fairings, making it compatible with a suite of current and future launch vehicles
- *Solar arrays on the cargo module* increase flight time in space and support powered payloads

On the other hand, the Dream Chaser Space System is designed to be optionally piloted and transport up to seven crew members and cargo to LEO destinations with a gentle return to a runway landing. The spacecraft is roughly ¼ of the Space Shuttle orbiters total length, but can carry the same crew size and can remain docked to the ISS considerably longer.
Dream Chaser Space System specific features include:

- Environmental control, life support system and seating capable of transporting a crew of seven and critical cargo to LEO
- Windows for crew visibility
- Launches without a fairing on top of a human-rated United Launch Alliance Atlas V rocket with the ability to safely abort to a runway in the event of an emergency
- Integral main propulsion system for abort capability and major orbital maneuvers

Both vehicles are designed for high reusability (at least 15 times), reducing overall cost and providing rapid turnaround for re-flight opportunities. The ability to launch on top of multiple launch vehicles and land at a wide variety of runways makes Dream Chaser a flexible and viable option for reliable transportation.

Dream Chaser for European utilization

In December 2013, the German Aerospace Center (DLR) announced a funded study to investigate ways in which Europe might take advantage of the Dream Chaser crewed spaceplane technology. Named the DC4EU (Dream Chaser for European Utilization), the project will

study using it for sending crews and cargo to the ISS and on missions not involving the ISS, particularly in orbits of substantially greater altitude than the ISS can reach, such as microgravity science, satellite servicing and active debris removal (ADR).
This study was completed on February 3, 2015 and the cooperation between SNC and OHB SE was renewed in April 2015 for additional two years.

1.2.1 *Dream Chaser Space System* overview

The *Dream Chaser Space System* is the flexible and affordable spacecraft for human transport to LEO and has a significant heritage of completed development work. It is a **third-generation fully reusable, pressurized, suborbital and orbital vertical-takeoff, horizontal-landing** (VTHL) **lifting-body spaceplane**. Similarly to its father, the HL-20 PLS, Dream Chaser is planned to be launched atop of the Atlas V rocket, carry up to seven people to and from LEO, and finally land on conventional runways because of its all non-toxic consumables, including propellants. An overview of mission concept of operation is reported in Fig. 1.15, while in Fig. 1.16 the main mission phases are presented.

Trade studies drove SNC's decision to use a lifting body concept because of the significant advantages it offers over capsules for human transport, like:

- Increased cross-range
- Lower g forces during reentry ($\leq 1,5$g)

thus improving safety and landing opportunities while providing a more benign entry environment for sensitive payloads, crew and medical emergencies.

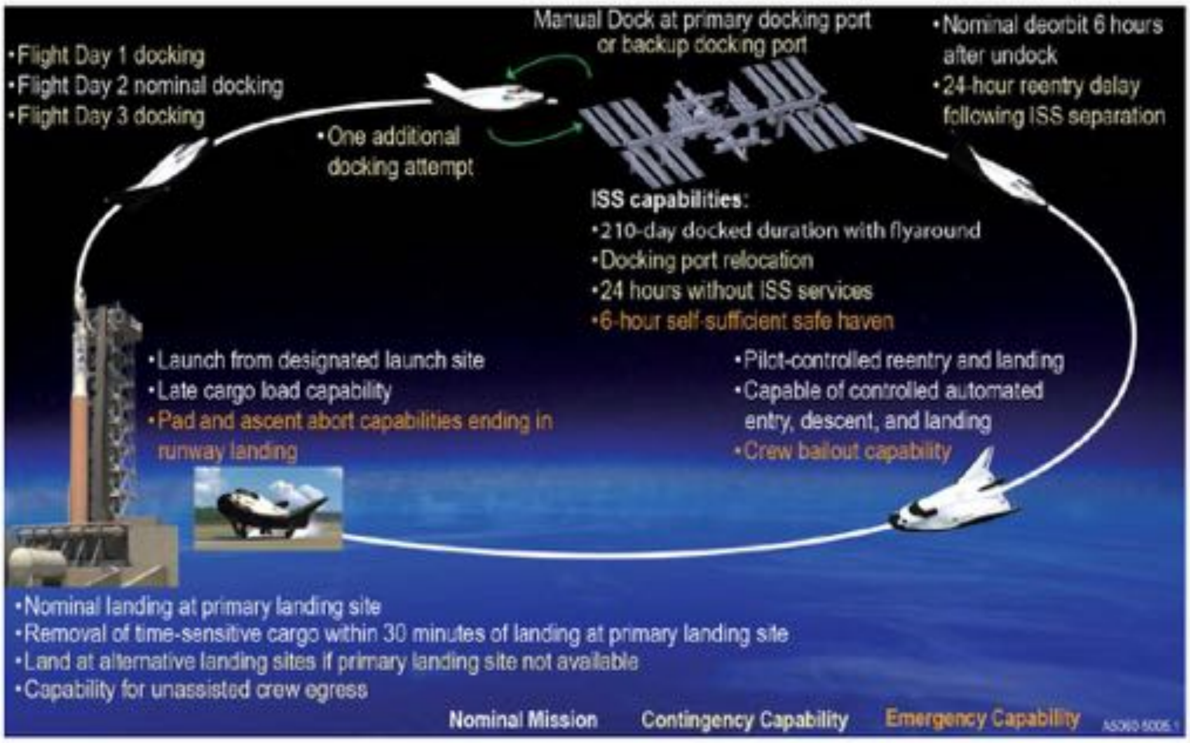
•Flight Day 1 docking
•Flight Day 2 nominal docking
•Flight Day 3 docking
•One additional docking attempt
Manual Dock at primary docking port or backup docking port
•Nominal deorbit 6 hours after undock
•24-hour reentry delay following ISS separation
ISS capabilities:
•210-day docked duration with flyaround
•Docking port relocation
•24 hours without ISS services
•6-hour self-sufficient safe haven
•Launch from designated launch site
•Late cargo load capability
•Pad and ascent abort capabilities ending in runway landing
•Pilot-controlled reentry and landing
•Capable of controlled automated entry, descent, and landing
•Crew bailout capability
•Nominal landing at primary landing site
•Removal of time-sensitive cargo within 30 minutes of landing at primary landing site
•Land at alternative landing sites if primary landing site not available
•Capability for unassisted crew egress
Nominal Mission
Contingency Capability
Emergency Capability
A5060-5005.1

Figure 1.15: ISS Mission Concept of Operations. The Dream Chaser will have frequent deorbit opportunities to landing sites in the United States and the ability to perform runway landings on every orbit during LEO missions. Thus, in case of a medical emergency, the Dream Chaser could land an injured crew member on a runway within a matter of hours.

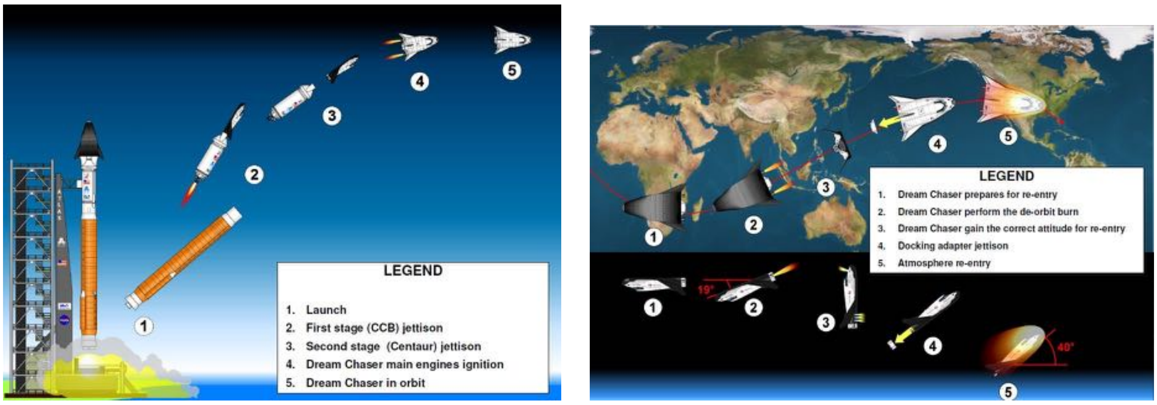
LEGEND
1. Launch
2. First stage (CCB) jettison
3. Second stage (Centaur) jettison
4. Dream Chaser main engines ignition
5. Dream Chaser in orbit
LEGEND
1. Dream Chaser prepares for re-entry
2. Dream Chaser perform the de-orbit burn
3. Dream Chaser gain the correct attitude for re-entry
4. Docking adapter jettison
5. Atmosphere re-entry
19°
40°

(a) *Launch Phase* **(b)** *Reentry Phase*

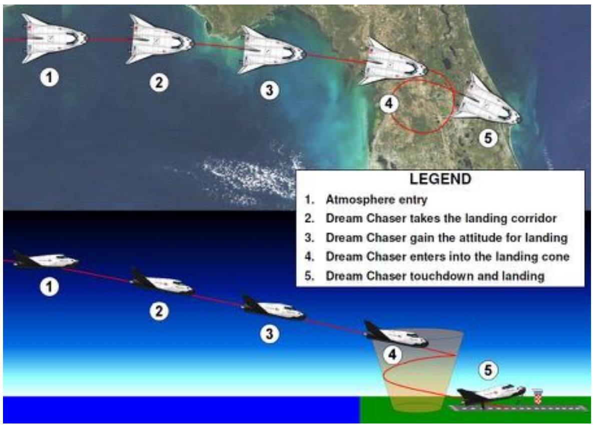
LEGEND
1. Atmosphere entry
2. Dream Chaser takes the landing corridor
3. Dream Chaser gain the attitude for landing
4. Dream Chaser enters into the landing cone
5. Dream Chaser touchdown and landing

(c) *Landing Phase*

Figure 1.16: Details of Dream Chser main mission phases.

Actual updated Dream Chaser configuration retains the outer mold line of the HL-20 design, whose aerodynamics have been refined through more than 1200 Langley Research Center (LaRC) wind tunnel tests, hundreds of hours of piloted flight simulation, and four successfull (two orbital) flights of the similar Russian BOR-4. Besides, Dream Chaser features a new composite structure using modern construction techniques and materials, and integrates a new SNC developed onboard liquid propulsion capability.

Every Dream Chaser mission will use humans-in-the-loop to enhance mission success, safety and reliability. A pilot reduces software requirements, enables timely and effective decision-making and provides greater likelihood of success of ISS docking operations. Eliminating automated rendezvous and docking by using a crewed spacecraft reduces development time and cost. To further reduce development time and risk for the Dream Chaser Space System, the ULA's Atlas V reliable expendable booster will be used.

Chapter 2

Vehicle Definition

As Sarafin suggests in his book [15], spacecraft structures can be categorized according to the different requirements which typically drive their designs: *"The **primary structure** is the backbone, or major load path, between the spacecraft components and the launch vehicle. **Secondary structures** include support beams, booms, trusses, and solar panels. We refer to the smallest structures, such as boxes that house electronics and brackets that support electric cables, as **tertiary**"*.
Tailoring this definition to our context, in this chapter we define the structural arrangement of the *Dream Chaser Space System* spacecraft, giving a comprehensive description of all its structural components and an overview of its key subsystems, as well as, the employed materials and joint technologies.

2.1 Concept development philosophy of the HL-20 PLS

Before starting straight away defining the Dream Chaser structural concept, we have to make a little digression regarding the HL-20 design rationale and approach.

While the Space Shuttle has proven itself to be a major technological advancement in the space transportation capabilities of the United States, one of its original goals, low-cost space transportation, has not been achieved. Since the late 1980s, NASA has been examining options for the next generation of US space transportation systems required to satisfy future mission needs in terms of personnel transport, payloads requiring manned presence, unmanned payloads, improved cost-effectiveness, increased vehicle reliability and safety, and large operational margins. One of these was the *Personnel Launch System* (PLS) program, whose primary mission would be to carry people to Space Station and back in a safe, cost-effective manner.
The HL-20 PLS concept is designed for **enhanced producibility and maintainability** [4]. This design approach provides features that facilitate manufacturing, maintenance, and inspection and overhaul of the flight articles. The key to the overall system design is the adoption of airline/aircraft approaches to initial certification and maintenance of flightworthiness. Ground rules for the HL-20 PLS study specify the vehicle be designed for **low operations and maintenance cost**. Aircraft-type operations and maintenance were adopted in order to achieve quickly turnaround times and efficient handling of the HL-20. Its structural design and subsystem packaging configuration were therefore impacted greatly by these ground rules.

HL-20 main design features

The baseline HL-20 design can accommodate up to ten people and has a overall length of 9 m and a span across the fins of 7,16 m. It weights approximately 12.700 kg on orbit or 16.78 kg when the launch vehicle adapter for National Launch System (NLS) and a launch escape system are included. Its landing weight is about 9980 kg.
As already stated, the Dream Chaser spacecraft retains the outer mould of the HL-20, but, because of its ongoing development, specific informations are not available about its inner structural layout. However, as reported in references [3], [4], [19] and [20], details are provided concerning the HL-20 subsystem design and internal structural arrangement (see Fig. 2.1).

To summarise, the HL-20 structure is composed of ***two primary components***:

- **Crew compartment**
- **Heatshield**

The crew compartment is a pressurised vessel that provides the necessary volume for crew habitability over the duration of the mission and serves as the primary structural element of the vehicle. The center section consists of a cylinder with a flat floor, a cockpit and close-out form the front, and a conical section form the aft end. Four frames extend from each side of the crew compartment to support the heatshield, subsystems, and the access panels. This crew compartment attaches to the booster at the aft end and supports all of the other components. Entry and exit hatches are necessary for ingress and egress from the HL-20 while on the launch pad, during docking to the ISS, on landing, and in the event of an emergency water-landing evacuation. The hatch located on the top of the vehicle can be used for prelaunch ingress and, in the case of a water landing, for egress. The aft hatch is for use in docking with the ISS and for normal egress on landing. The heatshield is suspended from the crew compartment by links to the extension frames and pressurised vessel. It provides thermal isolation from the crew module and, when removed, provides access to the pressure vessel during manufacturing and inspection.

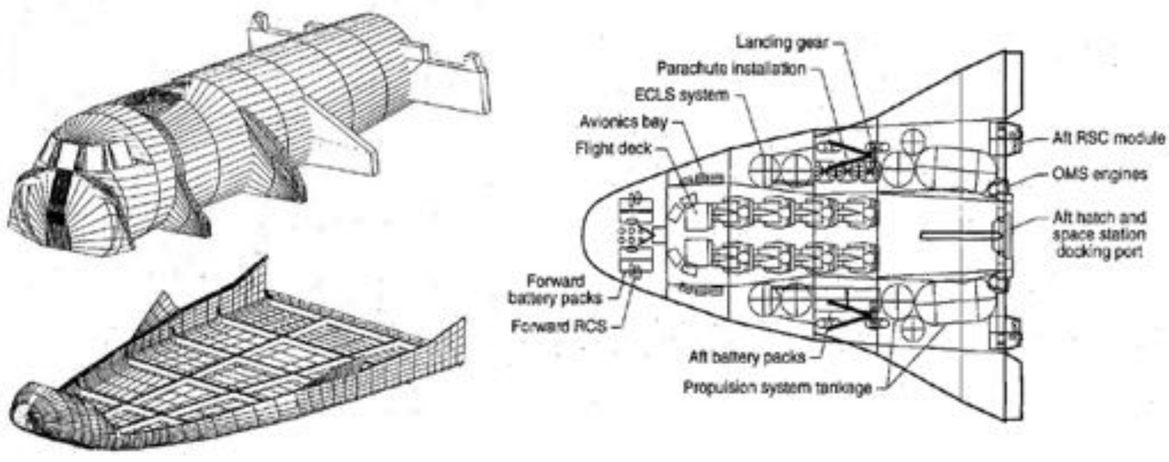

Figure 2.1: HL-20 primary structures (left, crew compartment on top of the heatshield) and subsystem layout (right).

The secondary structure consists of two canted fins or wings, eight large access panels and a center fin. Moreover, in an effort to reduce recertification, refurbishment and maintenance schedules, the HL-20 subsystems are positioned outside the crew compartment in a nonpressurised area. This area contains also the retractable landing gear, orbital maneuvering system

(OMS), reaction control system, prime power, environmental control and life support system, avionics systems, and personnel provisions.

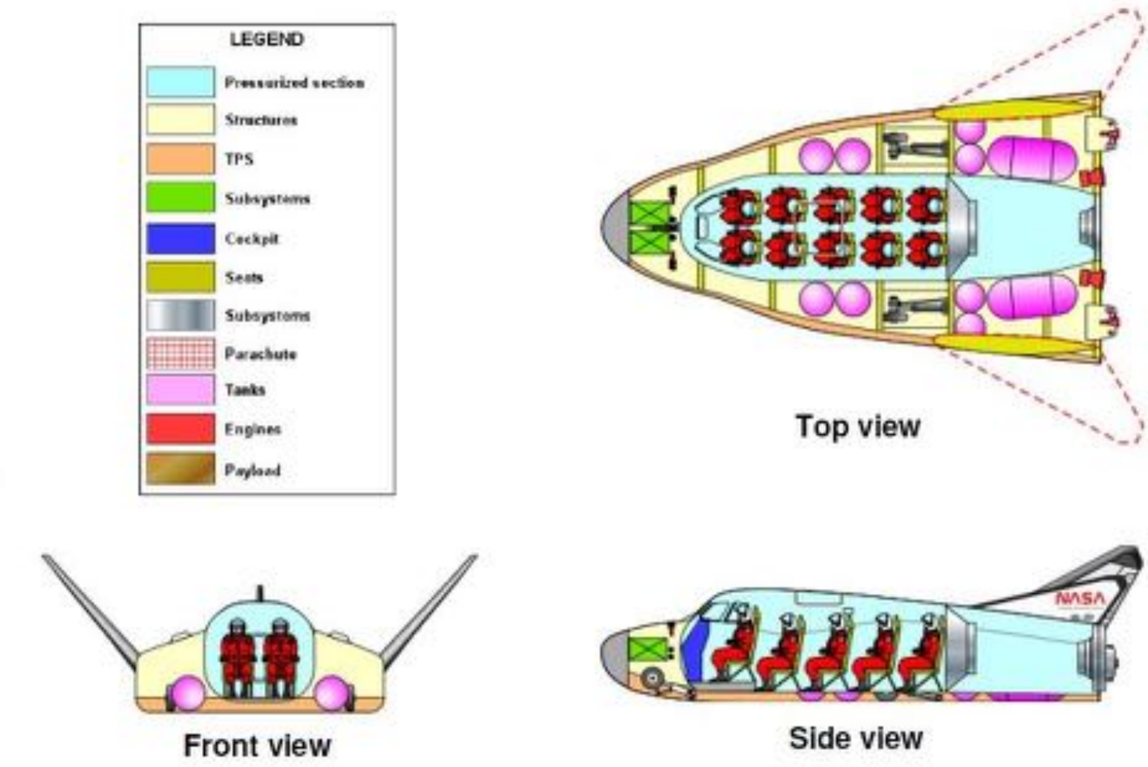

Figure 2.2: HL-20 cutaway. The crew compartment structural configuration is the result of a study [3] in which it was compared with a “conformal shell" configuration. The performed analyses of both concepts indicate no appreciable weight or load relief advantage of one over the other. Maintainability and operability became therefore the primary discriminator, leading to a choice of a crew compartment configuration.

2.2 Dream Chaser structural definition

2.2.1 Main features and key subsystems

Dream Chaser spacecraft can be easily visualised as the upgraded version of the HL-20 concept, in that it is built with modern materials and advanced manufacturing processes.
From an outer perspective, it presents the same shape in terms of aircraft type elements, as it shows the two canted fins, the center one, and the seven control surfaces. To be more precise, the **Dream Chaser spacecraft shape is an intermediate between a true lifting body and winged vehicle** since **its canted fins contribute about half of the net lift** [21].

The Dream Chaser vehicle baseline design has a total length of 9 m and a wing tip-to-tip width of 7 m. The weight stands approximately at 9000 kg, about 29% less than the HL-20. This gain in mass can be attributed to the lower number of passengers and, mostly, to the state-of-the-art composite materials Dream Chaser is made up of, which derive from a high technological readiness level (TRL) criterion selection.

The main features of the vehicle are summarised in the following table:

Reentry module	
Crew	up to 7
Length	9 m
Max wingspan	7 m
Height	2,8 m
Reference body length (no fins)	8,2 m
Reference body span (no fins)	4,51 m
Body planform area (no fins)	36,98 m^2
Habitable volume	16 m^3
Mass	9000 kg
Propellants	Liquid (C_3H_8/N_2O)
Electrical system	Batteries
Escape system	Liquid boosters
Hypersonic L/D ratio	1,8
Cross-range	2038,5 km
Landing speed	307 km/h
Glide time	$\sim$ 60 s

To perform all of its aerodynamic and orbital manoeuvres, Dream Chaser relies on the following subsystems:

PROPULSION SYSTEM. The Main Propulsion System (MPS), also used for aborts, is composed of two liquid engines that rely on a non-toxic combination of Nitrous Oxide (N_2O) and propane (C_3H_8). The Reaction Control System (RCS) shares oxidizer and fuel with the primary propulsion system. Since the Dream Chaser has significant delta-V margin on a nominal mission (greater than 50%) using a shared oxidizer and fuel for main propulsion and RCS saves hundreds of kilograms while increasing mission flexibility. Additionally, by using shared oxidizer and fuel the Dream Chaser can provide fault tolerance for minimal additional weight by designing the RCS engines to also perform the deorbit burn and nominal ascent burns to ISS.

AUTOLAND CAPABILITY. The Dream Chaser is optionally-piloted, which means that while the vehicle is equipped with autoland capability, the primary method of landing a crewed mission is through crew control. Autoland capability enables completion of a nominal mission with deconditioned crew, cargo-only flights, and crewed abort trajectories. As expected, there are some limited abort scenarios where the accelerations are relatively high ($\sim$ 6 g's), although within crew limits. With such a dynamic, challenging event, the Dream Chaser program desired additional landing options besides crew-controlled descent. The components enabling the Dream Chaser autoland capability are typical of conventional aircraft and do not require any additional navigational aid (Navaid) equipment at the landing site.

AERODYNAMICS. The Dream Chaser spacecraft shape is an intermediate between a true lifting body and winged vehicle in that its canted fins contribute about half of the net lift. There are seven control surfaces (CS) on the Dream Chaser. Four body flaps (upper and lower, left and right) provide roll control when used as ailerons, supplementary pitch control when used as elevators, and drag modulation when used in unison as a speed brake. A full-motion vertical fin provides yaw control and reduces adverse yaw events due to body flap deflections. Two elevons (left and right) are installed at the trailing edge of the canted fins, providing the primary pitch control and supplementary yaw control.

Thermal Control System. In conjunction with the primary propulsion system, the Thermal Control System (TCS) uses non-toxic fluids to enable quick access to the vehicle upon landing. The TCS system incorporates two N_2O boilers and a Phase Change Material (PCM) heat exchanger to control the temperature of the Dream Chaser vehicle while in the atmosphere. The PCM material is a wax-like material that can be reused by cooling the heat exchanger in space with the primary TCS system. The primary TCS fluid while in space is water (H_2O) through an evaporator. The combination of the N_2O and PCM enables the Dream Chaser vehicle to maintain temperature of all the systems, including the crew, during landing and after wheels-stop. This redundancy provides the option of removing the Dream Chaser off the runway before ground support equipment (GSE) is needed.

All of these key subsystems (propulsion, autoland, aerodynamic control, and TCS) enable post-landing procedures that are compatible with public-use airport operations and broader public and flight crew safety.

2.2.2 Structural arrangement

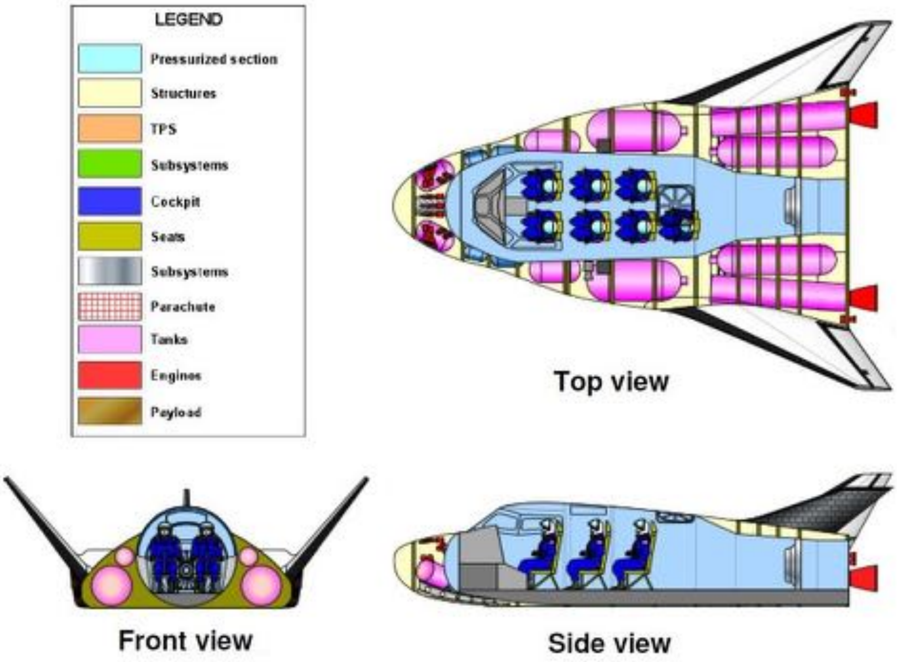

Figure 2.3: Dream Chaser cutaway.

Dream Chaser up-to-date configuration features the following structural components:

- *Exterior*: same as HL-20
- *Interior*:
  - Crew module: pressurised vessel, floor, 7 seats and cockpit

  - 13 fuselage frames or ribs
  - 10 fuel tanks for propane and nitrous oxide, 4 for normal nytrogen/oxigen balance (crew cabin pressurisation)
  - 2 main engines (exhaust nozzles are visible)
  - 2 access hatches (top and aft of the vehicle)
  - Orbital manoeuvring system/reaction control system (nose and rear of the vehicle)
  - Avionics, aerosurface actuators, landing gear, power supply and distribution, life support system (not shown)

2.3 Our proposal

To the extent of our project, and due to the obvious difficulty in designing something still classified, we kept the vehicle inner layout proposed in Fig.2.3 and derived our geometrical and structural assessments from then on. Further clarifications on how we proceeded are fully presented in the next chapter of this report.

Taking our cues from Sarafin, and pursuing our project goal, we focused on modeling those components defining the major load paths crossing the vehicle structure, that is those fundamental constituents necessary for defining the overall structure shape and functionality. This is because we left out tertiary structures as not of our relevant concern regarding a preliminary design study. In addition, we discarded also the central upper fin for yaw control, since it does not provide appreciable structural contributions.

Here we provide a comprehensive list of these elements:

- **Primary Structure**. We categorised as primary structure the assembly of:
  - Pressurized Module
  - 13 Fuselage Ribs (numbered 1-13 proceeding from nose to aft)
  - Fuselage Skin
  - 2 Axial "*keel beams*"

  The reason for this classification will become clear as we proceed in presenting and discussing the selected load conditions and CAD-modeled components (chapters 4 and 5, respectively), but we can anticipate that this choice lies in the ability of these elements to withstand, absorb and internally distribute the huge axial forces, namely compressive/tensile, deriving from an abort maneuver (where the high g's are felt particularly in the rear section of the vehicle, where the MPS is hosted) and the strong bending moments felt during the aerodynamic gliding maneuver. Moreover, the primary structure is usually designed for stiffness and to survive steady-state accelerations and transient loading during launch [15]. Besides, it sets out the natural frequencies of the overall structure.

- **Secondary Structure**. As secondary structure we defined the assembly of:
  - Canted fins
  - Pressurized Module floor, wing-to-fuselage attachments, thrusters mounts

Tanks have also been designed, mainly because they make an important contribution to the total inertia of the spacecraft. In this regard, we took care in including all the masses of the remaining excluded components, so as to provide the highest level of accuracy to our results during FEA simulations.

2.4 Materials

Frank Taylor, director of technology for Sierra Nevada's Space Exploration Systems, identifies Sierra Nevada's main engineering challenge as choosing the materials and process for a *human-rated space structure* that can withstand temperature variations ranging from −54 °C to 177 °C during the time period of each mission, and through repeated missions, without sacrificing the required strength and other performance properties.
Sierra Nevada Corp. elected to use **composite materials in both primary and secondary structures**, including the cabin, bulkhead, canted fins, aerosurfaces and aeroshells. It is primarily ***carbon fiber preimpregnated with bismaleimide (BMI) resin***, in both woven fabric and unidirectional tape, in a sandwich structure with an unidentified nonmetallic honeycomb core.

The materials selection was narrowed to products supplied by Cytec Engineered Materials (Tempe, Ariz.) and Hexcel Corp. (Stamford, Conn.). "Cytec's 5250-4 and Hexcel's M65 BMI prepregs are being used in discrete areas of the structure, based on the unique characteristics of each" Taylor reveals. "These materials retain good strength at high temperature." Further, he says, their low coefficients of thermal expansion (CTE) minimize the effect of thermal gradients within the structure. The high specific stiffness (modulus) of the composite minimizes strains on heat shield. Similar to the ceramic tiles and blanket materials used on the Space Shuttles, the heat shield minimizes the thermal strains imposed on the vehicle by extreme thermal gradients during reentry into Earth's atmosphere. Taylor says this results in a more efficient system and better protects the crew and cargo.

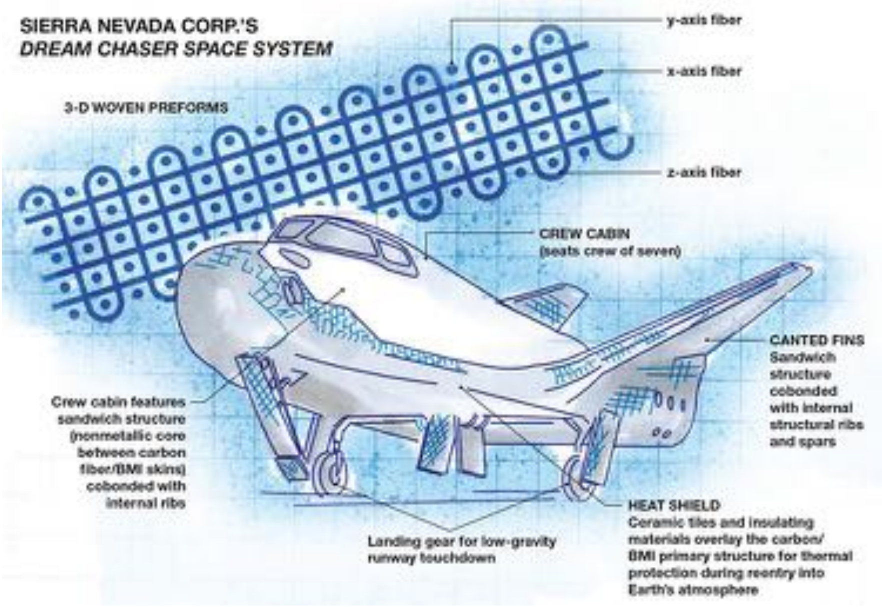
SIERRA NEVADA CORP.'S
DREAM CHASER SPACE SYSTEM
3-D WOVEN PREFORMS
y-axis fiber
x-axis fiber
z-axis fiber
CREW CABIN (seats crew of seven)
CANTED FINS Sandwich structure cobonded with internal structural ribs and spars
Crew cabin features sandwich structure (nonmetallic core between carbon fiber/BMI skins) cobonded with internal ribs
Landing gear for low-gravity runway touchdown
HEAT SHIELD Ceramic tiles and insulating materials overlay the carbon/BMI primary structure for thermal protection during reentry into Earth's atmosphere

Figure 2.4: Dream Chaser materials setup.

2.4.1 BMI resin

BMI resins, now a leading class of thermosetting polyimides, reportedly offer the highest service-temperatures of any thermoset (some can withstand up to 230 °C to 290 °C in extended service). Further, they offer familiar, epoxy-like autoclave processing.
In LEO, structural materials also must be shielded from atomic oxygen, single oxygen atoms (O) that, like peroxide, are extremely reactive oxidizers. Exposed epoxy-based composites are subject to substantial oxidation and erosion. BMIs also tend to oxidize in atomic oxygen, so the Dream Chaser will be shielded by an unidentified protective coating. Although details about the fiber architecture are proprietary, Taylor says Sierra Nevada fully exploited the ability to tailor fiber architecture and layup and, thus, the mechanical strength and stiffness properties, "to meet the challenging launch/abort, reentry and landing environments that the Dream Chaser vehicle is exposed to during its mission."

Stiffness is a vital factor because aerodynamic and launch forces subject all materials to significant vibration, acoustic and bending loads. Impact resistance is another requirement for protection against damage from the occasional micrometeoroid. Taylor also cites the time and cost savings that have accrued to the program through the use of composites, due to their flexibility in manufacturing. Tooling and manufacturing costs have been reduced through parts consolidation. For example, the crew cabin comprises only two shells, or skins, cobonded with multiple internal frames. The fins, too, are cobonded parts that combine upper and lower skins with three spars and multiple ribs. Further, as the vehicle's structural design matures, tooling changes for composites can be made more rapidly than is possible in metals fabrication. "The ability to produce additional vehicles more rapidly and to produce modified versions of the Dream Chaser to meet future client needs gave us greater confidence in our business plan," says Mark Sirangelo.
All composite parts will be autoclaved at the recommended time and temperature for the material ($\sim$ 177 °C to 204 °C). In structural assembly operations, Sierra Nevada will minimize the need for fasteners by employing a combination of cocuring and cobonding in an autoclave, incorporating the honeycomb core and advanced 3-D woven preforms. The 3-D preforms will be cobonded at most joints to further strengthen the structure.

2.4.2 Metallic Parts

Metals are used only for some structural parts for which their manufacturing and structural reliability with the use of composite materials are still under validation processes. Junction plates for fin root fittings and propellant and oxidizer tanks are made with metals. Bolted joints, as will be used for the first design of fin root fittings, are critical parts in terms of determining load paths from one part to another therefore having an isotropic material simplifies the structural analysis. Moreover, light alloys have been using in aeronautic and astronautic structures for decades and their reliability have been verified throughout that period. The material used for fin root fitting is the common 7075-T6 alloy extensively used in high stressed members of planes and spacecrafts. Tanks made with composites have the main drawback of the easy diffusion of molecules through the matrix fiber and this has prevented their use until now, especially for propellant that have a small atomic radius like LH2. Tanks are usually made with Titanium therefore Ti-6Al-4V, grade 5, STA alloy have been chosen both for propellant and oxidizer tanks.

2.5 Joints Technology

Due to the nature of chosen materials, bonding represents the primary fastening technology employed. As previously stated, almost every mechanical interface is cobonded in a single autoclave processing, in order to reinforce major component bond sites and increase the whole strength of the structure.

Nevertheless, we hypothesised the use of bolts to hold together the fins bulkhead to the fuselage ribs, where hinge fittings are necessary to correctly transfer the incoming fins loads, the material used for pins is a SAE class 8.8 Steel. Because of lack of specific informations about the real design, we chose this solution after some mechanical considerations on how loads have to be transferred, eventually finding out that this kind of connection is extensively used onboard of conventional aircrafts (which, in turns, gave us quite a relief).

Chapter 3

Preliminary Studies

In the early phases of the project, we thought that the reentry phase was the most critical condition in terms of mechanical and thermal loads, thus we spent many efforts in achieving the sufficient knowledge to deal with this subject. The kickoff was an extensive literature survey of ballistic capsules and aerodynamic reentry vehicles studied and designed so far found across the web. This research instructed us about the mechanical and thermal environments experimented by lifting bodies and reentry vehicles in general. An invaluable help has been provided by the extensive lab works carried out in the 90's on the HL-20, specifically from an aerodynamic standpoint, where the effects of several Mach ranges encountered by the vehicle were investigated.
With all these informations, we organized the framework of our analysis covering these areas:

- *Load definition during reentry*
- *Structural analysis*
- *Geometrical modeling*
- *Thermoelastic analysis*
- *Composite materials*

In the end of the reentry phase analysis, we recognized this flight condition hardly to be a design point for the structure, because of the low levels of loads experienced during hypersonic flight, and because of the unrealistic dimensions resulting from the preliminary sizing of structural members we performed.

It was clear that different flight conditions had to be identified for the design of the primary structure. Past studies on HL-20 helped us another time, as we found in literature [2] a complete preliminary analysis and design of HL-20 structure. This work identifies the most critical flight phases in terms of load factors for a typical round-trip to ISS, and uses them to design the primary structure. Important informations regarding the primary structure concept and how each part were modeled for FEM analysis are all clearly documented.

From now on, the work made by Bush [2] has been our main reference that steered our next steps. The framework remained almost the same, except for the thermoelastic analysis we were forced to discard essentially because we had not enough time. The updated design points taken from [2] and adapted for Dream Chaser will be explained extensively in Chapter 4, while Chapter 5 covers the preliminary sizing of the structure, the CAD modeling of the entire primary structure of the vehicle, and the FEM analysis using the same composite materials of Dream Chaser.

3.1 Reentry Phase Analysis

The analysis of atmospheric reentry maneuver was carried out to evaluate forces and moments acting on the spacecraft. A typical reentry trajectory passes through a wide range of Mach numbers, from 20÷25 at the atmosphere borders down to 0 once the spacecraft is landed. Over that range, forces, moments and thermal stresses vary in time and a complete analysis requires their evaluation over that interval in discrete and significant points of the trajectory. This requires a huge amount of work that is not possible to do in a restricted timeframe like that of a university project. Therefore, a decision had to be taken on what phase of the trajectory perform the analysis. The final decision was to focus on the intermediate phase of the trajectory where Mach number reaches a value of 10.
The primary reason that led us in choosing this trajectory point was the possibility to carry out an accurate analysis with all the available informations. First of all, we collected all the wind tunnel data [16] of the HL-20 regarding aerodynamic coefficients at $M = 10$. Lately, we estimated the altitude correspondent to that level of Mach from the performances curves of the Space Shuttle shown in figure 3.1, in order to obtain the local atmospheric data. The validity of this estimation is rather plausible because of the similar hypersonic lift-to-drag ratio values Space Shuttle and Dream Chaser display, a parameter that affects the shape of the reentry trajectory. Besides, this assumption is well-supported considering the values of ballistic coefficient possessed by the two spacecrafts, giving us an implicit proof of their similar behaviours in terms of inertia to atmospheric drag effects:

$$C_B = \frac{M_{S/C}}{A_{S/C} C_D} \Rightarrow \begin{cases} (C_B)_{SS} \approx 476,4 \text{kg}\,\text{m}^{-2} & \text{where } M = 10^5\text{kg},\ A = 249,9\text{m}^2,\ C_D = 0,84 \\ (C_B)_{DC} \approx 616,8 \text{kg}\,\text{m}^{-2} & \text{where } M = 9000\text{kg},\ A = 36,98\text{m}^2,\ C_D = 0,36 \end{cases}$$

For the sake of completeness, Dream Chaser reentry mass was estimated on the basis of the required mission $\Delta V = 270\,\text{m/s}$ through the use of Tsiolkowsky equation, given a specific impulse of 300 s from the propulsion system. Actually, these numbers are meant to give an idea of the order of magnitude we are talking about, so as to compare the two vehicles, rather then providing the exact values. Indeed, they are quite close to each other.

The typical performance parameters for reentry are shown in Fig.3.1. The angle of attach curve provides the informations needed to perform the flight equilibrium analysis: altitude was estimated to be 53 250 m, and atmospheric data based on ISA Standard Atmosphere model are reported in table 3.1. The angle of attach that corresponds to this flight condition is 30°.

Altitude (m)	**Density** (kg/m^3)	**Pressure** (Pa)	**Temperature** (K)	**Sound speed** (m/s^2)	**Viscosity** (Ns/m^2)
53250	6.62×10^{-4}	50.22	264.35	325.94	1.69×10^{-5}

Table 3.1: ISA atmospheric data at 53 250 m.

All these data were used to carry out the flight motion analysis and evaluate forces and moments acting on the vehicle. The equation of motion in this flight condition considers the rotational equilibrium around pitch axis provided by the action of control surfaces in order to stabilize the descend at 30°. Wind tunnel model used in reference [16] has been tested also in configuration with sideslip angle β different from zero. Given the possibility that during

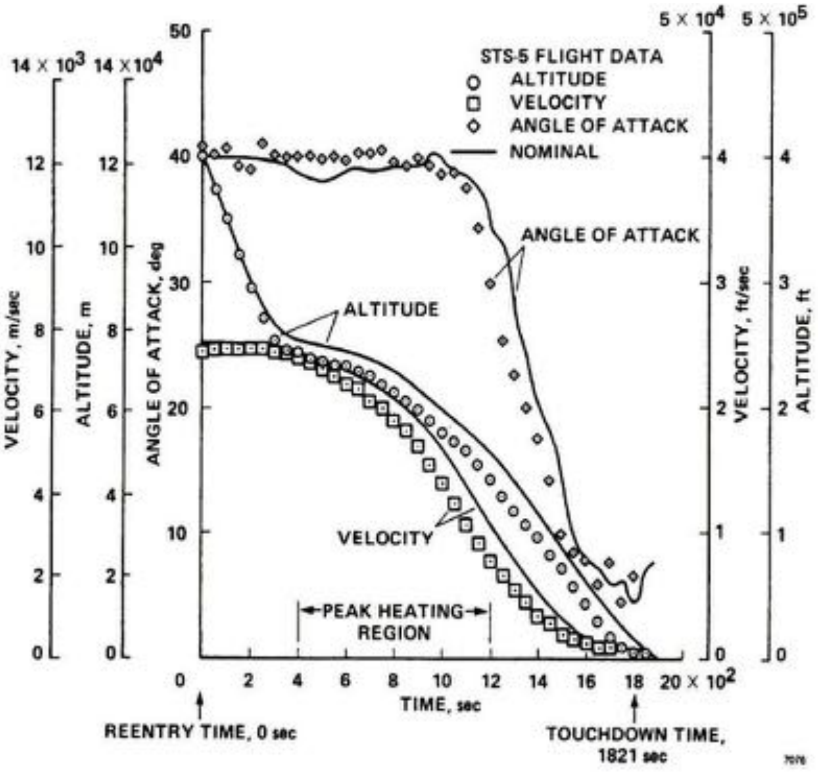

Figure 3.1: STS-5 reentry parameters as function of elapsed time from reentry.

this phase the spacecraft orients itself in order to catch the right reentry corridor, we decided to analyse this configuration, since it would generate a lateral force that would act on the structure.

Attitude control for HL-20 [16] was performed by means of control surfaces during atmospheric flight. Roll is controlled by lower body-mounted flaps, pitch is controlled by fin elevons and upper body-mounted flaps, and yaw is controlled by the top central fin, which acts as a rudder. We used the same scheme also for the Dream Chaser in absence of any information regarding its actuation scheme. Pitch control used a combined action because fin elevon are effective up to $\alpha = 23.5°$, the remaining control moment is provided by upper flaps. This was taken in consideration during the analysis of rotational equilibrium.

The equations of motion expressing the local translational and rotational static equilibrium of this flight configuration are:

$$\boldsymbol{F_A} + \boldsymbol{W} + \boldsymbol{F_I} + \boldsymbol{F_c} = \boldsymbol{0} \tag{3.1}$$

$$\boldsymbol{M_A} + \boldsymbol{M_c} = \boldsymbol{0} \tag{3.2}$$

where $\boldsymbol{F_A}$ is the aerodynamic force, $\boldsymbol{W}$ is the weight, $\boldsymbol{F_I}$ is the force of inertia, $\boldsymbol{F_c}$ is the force generated by control surfaces, $\boldsymbol{M_A}$ are moments of aerodynamic force and $\boldsymbol{M_c}$ are control moments. $\boldsymbol{F_A}$ and $\boldsymbol{M_A}$ are known from aerodynamic coefficients, the only unknowns are $\boldsymbol{F_I}$ and $\boldsymbol{F_c}$. Projecting equation 3.1 in the body axes reference frame as showed in figure 3.2:

$$\begin{cases} -D\cos\alpha + L\sin\alpha - Mg\sin\alpha = Ma_x \\ Y + D\sin\beta = Ma_y \\ -D\sin\alpha - L\cos\alpha + Mg\cos\alpha + L_b + L_f = Ma_z \end{cases} \tag{3.3}$$

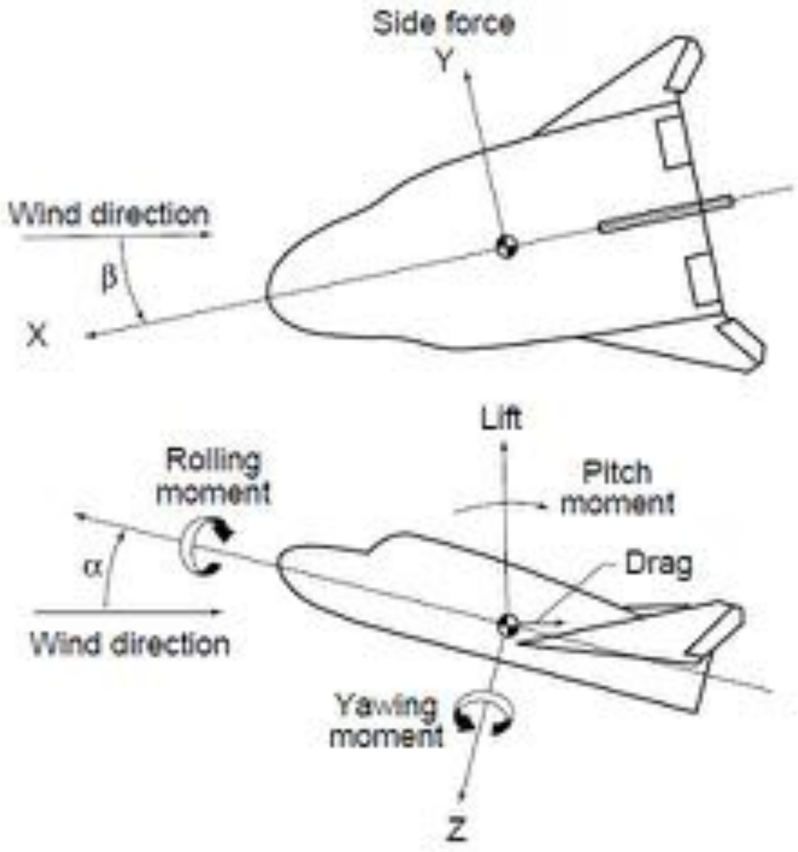

Figure 3.2: Body reference frame with positive signs convention at Mach 10 flight regime.

with M, mass of the spacecraft, L, D and Y the aerodynamic force components in the wind axis reference frame and L_b, L_f the body flap and elevon lift respectively. Dividing all terms by M, system 3.3 represents a set of linear equations in the unknowns (a_x, a_y, a_z).
Equation 3.2 written in body axes reference frame expresses the rotational equilibrium about the pitch axis. As already explained, pitch control is performed by the simultaneous action of fin elevons and lower flaps. This has been taken into account introducing in 3.1 and 3.2 the lift generated by the control surfaces. Pitch moment is evaluated from test data of pitch moment coefficient and evaluated at the gliding angle of attach, $C_{(m(30°))}$.
The control moment is distributed unevenly between elevons and flaps. It is assumed that elevons generate a moment that corresponds to a pitch moment coefficient at 23.5°, $C_{(m(23.5°))}$, taken from experimental data [16]. The remaining part of the pitch moment is generated by upper body-mounted flaps. Equation 3.2 along pitch axis is then:

$$\begin{cases} 2L_b l_T + 2L_f l_f = -M_{pitch(30°)} \\ 2L_f l_f = -M_{pitch(23.5°)} \end{cases} \tag{3.4}$$

where L_b, l_T, L_f, l_f represent respectively the flaps lift and their moment arm, with respect to the center of mass of the vehicle, and the elevons lift and moment arm. Moment arms are estimated from scale drawings [24] of the Dream Chaser: these are $l_T = 3.5\,\text{m}$ and $l_f = 4\,\text{m}$. The second equation of 3.4 system expresses the moment generated by elevons as if they were acting alone at the 23.5° flight condition. Equations 3.4 are solved simultaneously with equations 3.3 to get L_b, L_f and (a_x, a_y, a_z).

All of these calculations have been implemented in a MATLAB®code, and the results are listed in table 3.2.

L (N)	62380.72
D (N)	47994.94
L/D	1.3
Y (N)	1516.08
M_{roll} (Nm)	4153.79
M_{pitch} (Nm)	-16318.55
M_{yaw} (Nm)	3852.79
L_b	1968.15
L_f	317.69

(a) Aerodynamic loads

W (N)	86733.93
a_x (m/s^2)	-11.3
a_y (m/s^2)	0.48
a_z (m/s^2)	-0.07
$\|\boldsymbol{a}\|$ (m/s^2)	11.31
n_x (g)	1.15
n_y (g)	-0.05
n_z (g)	0.01

(b) Inertial loads

Table 3.2: Results of the reentry phase analysis

In order to prove the reliability of our analysis, we performed an error estimation in order to get confidence in the assumptions we made. Basically, we evaluated the error between evaluated Mach number correspondent to the flight altitude we found, and the nominal Mach number in this flight condition (namely, 10). The result is just an error of 1.33%. This confirms our initial assumptions, especially the attribution of the Space Shuttle reentry trajectory performance parameters characterising the Dream Chaser.

A first glance to the values of load factors, tells us the inertia loads to be very small along lateral and normal directions, and of moderate level longitudinally. This may suggest that reentry phase is not as critical as we thought in terms of structural loading.

3.2 Preliminary Structural Design

Previous analysis results were used as input for a preliminary design of the structure. At this stage of the project, Dream Chaser structure was not completely defined. Few informations were available regarding a possible arrangement of the structural members as it was shown in Fig.2.1, therefore we decided to rely on that configuration after having made several considerations regarding the structural role of each element, and how they should have been interfaced to one another.

However, useful suggestions regarding the central structure came out from a picture of the pressurized module at the end of a curing cycle. The main change was attributed to the presence of two axial beams, which we decided to call *keel beams*, that had never been considered in the previous concepts. Final version of the structural model consists of two keel beams with C-shaped cross-section, symmetrically mounted on the pressurized module bottom and meant to absorb the bending moments about the pitch axis and the compressive load mainly generated by the atmospheric drag.

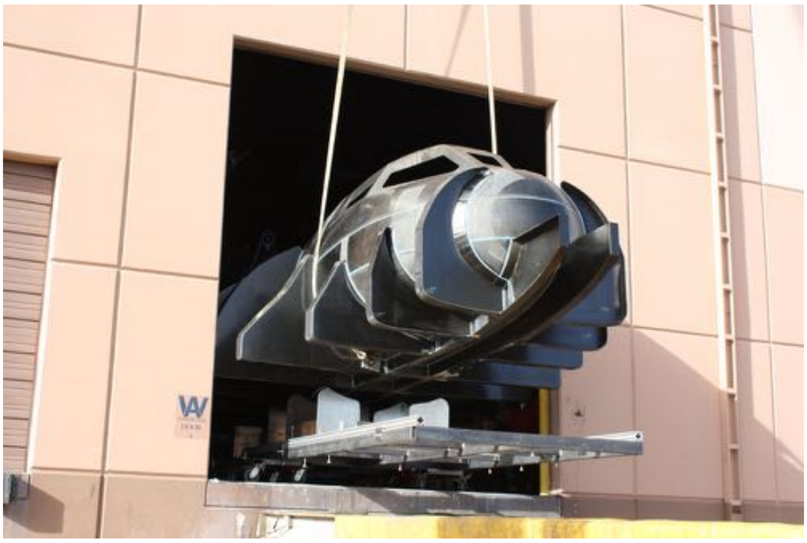

Figure 3.3: Dream Chaser central structure with pressurized module, body frame and two keel beams [1].

The "updated"model considered, therefore, a beam with a representative cross-section of the structural members explained so far. The evaluation of the loads and stresses was performed at a reference section placed at 6.95 m with respect to the Dream Chaser nose. The reference section scheme and its dimensions are reported in figure 3.4 and table 3.3 (further dimensions are listed in the relative MATLAB script in Appendix).

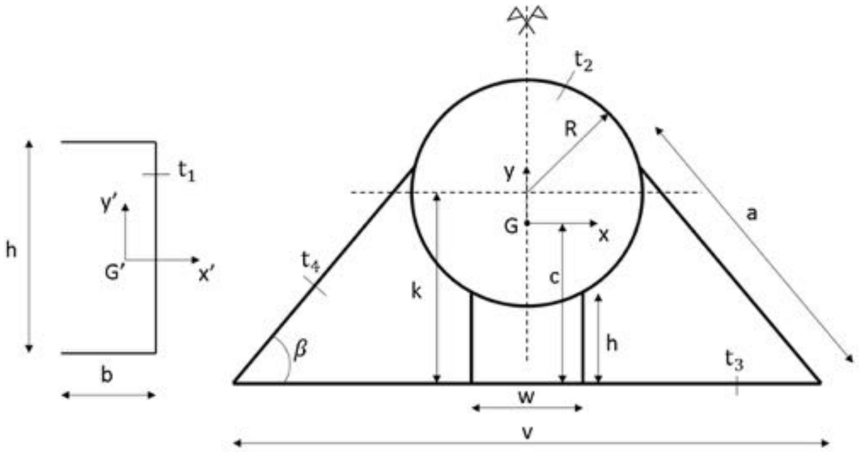

Figure 3.4: Model of the central body structure (beams mounted symmetrically with respect to the vertical axis.

Loads obtained in the reentry analysis were used to evaluate the wall thicknesses of the outer skin, t_3, pressurized module, t_2, and that of the keel beams. To simplify computations, flanges and web thicknesses of the keel beams were considered to be the same.

From a loading standpoint, we assumed a uniform load equally distributed between the two beams, which undergoes a direct stress because of the simultaneous action of bending moments and axial load. The maximum combined direct stress for a single beam is:

R (m)	0.86
v (m)	3.516
w (m)	0.37
h (m)	0.1
b (m)	0.15
k (m)	0.936
a (m)	1.417
c (m)	0.55
β (deg)	50

Table 3.3: Principal dimensions of central structure model.

$$\sigma_z = \frac{M_x}{J_{xx}}\frac{h}{2} + \frac{N}{A} \tag{3.5}$$

where $J_{xx} = 2bt_1h^2 + \frac{t_1h^3}{12}$ is the moment of inertia of the cross-section with respect to x and $A = 2t_1b + t_1h$ its area. The wall thickness of the keel beams, t_1, was then evaluated from equation 3.5.

The shear flow was instead evaluated from the theory of closed-section thin-walled beams subjected to shear loads. The section was divided into segments with an abscissa and on each segment is applied the following equation:

$$q = -\frac{S_y}{J_{xx}}\int_0^s ty\,ds + q_0 \tag{3.6}$$

where s is the local segment abscissa and q_0 is the basic shear flow, that is the open section shear flow evaluated once having cut the closed cell. When referring to the pressurized module wall, a slightly different expression of equation 3.6 has to be applied. Over these segments, the abscissa is not parallel to the coordinate system, in that it is expressed as a function of the angle α measured clockwise from the vertical axis, as indicated in figure 3.4 with $s = R\alpha$ and $0 \leq \alpha \leq 180$.

In equation 3.6, the corrective shear flow q_0 is null in closed cells like the pressurized module and keel beams since the section is symmetric along the y axis, while q_0 it is different from zero only in the lateral closed cells. Symmetry was wisely used to reduce the burden of calculations, considering just one half of the section. Consequently, corrective shear flow in the closed cell was evaluated by imposing equilibrium between the contribution of moment coming from shear flow in the walls and the moment of the external shear forces:

$$0 = \oint p(s)q\,ds = \oint pq_b\,ds + 2A_0q_0 \tag{3.7}$$

where $p(s)$ is the local moment arm, q_b is the basic flow and A_0 the cell area. Because of cross-section symmetry along y and moments values about its center of mass (our reference pole), contribution of external forces in equation 3.7 is zero. Equations 3.6, evaluated at each segment, and 3.7, form a non-linear system in the unknowns t_2, t_3 and q_0, that must be solved numerically. This was done with a MATLAB code (see appendix). Results of wall thicknesses at the end of this design process are reported in the following table:

As previously stated and guessed, the small output values of the wall thicknesses reflect the moderate load condition experienced by Dream Chaser during this flight regime.

t_1 (mm)	t_2 (mm)	t_3 (mm)
3.4	0.0768	0.00966

Table 3.4: Results of wall thicknesses of modeled cross-section members.

Thus, in conclusion of this very preliminary structural design, we found out this condition was hardly representative of a typical structural design condition, which is why further studies were undertaken in order to figure out what most demanding (or critical) structure load conditions was. These researches were fulfilled according to [16] and the subsequent outcomes and analyses are exhaustively reported in the next chapter.

Chapter 4

Vehicle Loading Conditions

Spaceplane and ballistic capsules have almost the same flight envelope. A subdivision into three main flight phases can be draw from a typical round-trip of both vehicles, these phases are atmospheric flight, space flight and hypersonic flight during re-entry. A vehicle is subjected to various kind of loads within each flight phases and its structure must withstand the entire load environment encounter during the mission. The spaceplane concept, and here specifically the lifting body configuration, expands the load environment, primarily during atmospheric flight and secondly in hypersonic flight. A lifting body generates more aerodynamic forces than an Apollo-like capsule, for instance, and performs aerodynamic maneuvers for a wider trajectory control capability during descent through atmosphere and orients itself for landing on a conventional runway. Clearly, these improved capabilities are at the expense of an increment of aerodynamic and inertial loads in the aforementioned flight phases.

The next section is a description of the prevalent load cases, these are obtained referring to a baseline mission that is supposed to represents a real mission scenario for which the Dream Chaser has been designed. The last two sections deal with load conditions analysed in this work; all the loads and other considerations will be used in following chapters during the preliminary design and FEM analysis of the structure and its relevant components.

4.1 Mission Baseline: ISS crew rotation

One of the main reasons for the design of Dream Chaser is the need for a spacecraft capable of transporting crew and payload to ISS and return them landing on a conventional runway. Therefore, a baseline mission that represents this operational environment needs to be identified in order to get precise estimation of loads acting on the spacecraft.

We based this study on previous works done for the HL-20 spaceplane [2], [3], deciding to adopt the same baseline mission, such as an ISS crew rotation mission scenario, in which the following sequences are included: launch, ascent, orbit, docking, berthing, deorbit, reentry, aerodynamic maneuvers and landing. As a result, five design cases were identified, which are given below.

During the launch phase, a spacecraft is subjected to a varying loading environment. Since here the launcher payload (i.e., Dream Chaser) is flying without the fairing, many problems arise concerning transonic, supersonic phases and aeroheating. Indeed, these aspects are strongly affected by the choice of the launcher, though a related study[8] reports that American DC/Atlas V configuration does not present any issue regarding aerodynamic loads and bending moments which fall within the load range already encountered by the launcher itself in different configurations. Future plans[5] indicate the Dream Chaser cargo version will be used by ESA and launched atop of an Ariane V, but no further informations regarding modified launch loads have been released yet.

An on-the-pad or altitude abort yields a critical loading condition. To escape an explosion and its resulting overpressure, an 8 g acceleration is provided by the abort motors mounted on the interface adaptor. This axial acceleration is the maximum value expected for the vehicle during a normal mission or abort. In fact, at launch, all of the fuel and cargo are onboard, and this condition yields the maximum inertial forces on the vehicle. In addition, the overpressure from a booster explosion reaches approximately 10 psi ($\cong 0.68$ atm) on the exterior surfaces, thus leading to additional structure loading.

The later phases of ascent present another design loading condition. The tiny pressure at high altitudes generates a pressure differential between the pressurized module and the exterior of 14.7 psi ($\cong 1$ atm), in combination with a 3 g axial acceleration imparted by the launcher.

While on-orbit, loads are mainly generated by thrusting maneuvers to rendezvous with ISS and attitude control by reaction jets. Significant vehicle loads are not expected to occur during either docking or berthing, given also the fact that no informations regarding these aspects were found. Some local loading will occur (for instance during docking sequence by the dedicated mechanisms), but this represents a premature assessment to be done at this stage, and it is beyond the scope of this analysis.

Upon re-entry, aerodynamic effects become significant on the vehicle. The maximum dynamic pressure during this phase of entry occurs around Mach 2.5 where the flight angle of attack is 6°. At this condition, pressures on the wing are in the neighbourhood of 3 psi ($\cong 0.2$ atm). The following maneuver is an aerodynamic maneuver, namely *pullup*, with a 2.5 g acceleration normal to the vehicle. This is reported to be the most critical condition, that is the design condition[2].

Lastly, landing occurs. A nominal touchdown deceleration at a sink rate of 3 ft/s ($\cong 0.91$ m/s) is assumed, thus entailing an acceleration normal to the vehicle of magnitude 0.35 g. A more conservative design condition of a 4 g touchdown was utilized in paper[2]. An overview of the critical load conditions and the relative schematic load diagram are reported in Fig.s 4.1a and 4.1b.

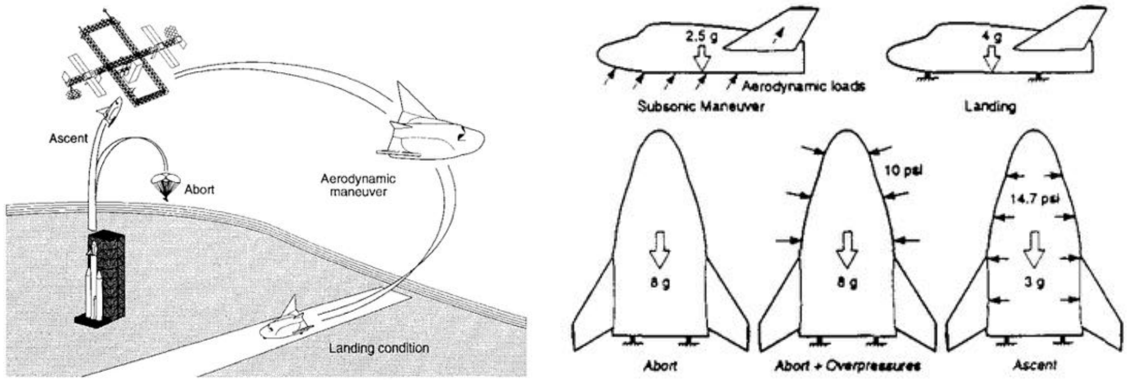

(a) Artistic drawing of critical load conditions[2] **(b)** Schematic load diagram for each load condition [3]

Figure 4.1: Load conditions of the ISS crew rotation baseline mission.

In a framework of a university project the available time was not enough to analyse all the aforementioned load conditions, so we had to make a choice. This fell back on those we believed were crucial for the design of the HL-20 structure as well as for the Dream Chaser, namely the 8 g abort and 2.5 g pullup maneuvers.

4.2 8-g Abort

If an 8 g abort maneuver is to be performed, then the vehicle will undergo its **maximum loading condition** with respect to the whole mission, particularly in terms of axial compressive/tensile loads. Related analyses [2] report levels of stresses as high as 2500 lb/in^2 ($\cong$ 17.24 MPa) and 2000 lb/in^2 ($\cong$ 13.79 MPa) for compressive/tensile loads, respectively, while hoop loads do not exceed 500 lb/in^2 ($\cong$ 0.35 MPa). Additionally, it is important to outline that such a scenario sizes about 36% of the total structure mass, which in turns represent almost 10% of the global mass of the vehicle.

In case of an on-the-pad abort or abort up to 64 s after liftoff, the vehicle has enough energy to return to the launch site. A window exists between 64 s and 403 s where it must be aborted to a water landing aided by parachutes. Water impact loads could reach level as high as 8 g due to the combined effects of vehicle impact and wave action. Thus, personnel safety is the primary concern in this case, while vehicle survivability is not a requirement.
So, when an emergency occurs, an escape maneuver is performed by the LES (Launch Escape System). During the space race era, and recently on Soyuz spacecrafts, the LES was mounted on top of a capsule in a tractor configuration, meaning the escape thrust was exerted by pulling away the spacecraft from the launcher interface. With the arrival of HL-20, and lately of Dream Chaser, the LES configuration changed. The system is implemented in a pushed configuration, in that the thrust vector now pushes away the spacecraft from the ground. Actually, HL-20 and Dream Chaser have different LES architecture: HL-20 mounts a block of rocket motors around the launcher adapter interface, while the DC uses its main propulsion system to provide the needed impulse. This translates into a different load path during engine firing. In HL-20, thrust is not applied directly on the structure but is transferred via adapter interface, while in DC it is applied directly to the primary structure by means of propulsion system attachments.

Based on HL-20 available data, we retained the 8 g acceleration value needed to escape an explosion and its resulting overpressure. As shown in Fig.4.1b, two loading subcases can be derived: an 8 g abort and an 8 g abort plus 10 psi overpressure. We decided to analyse only the former on-the-pad abort subcase, since we believed a less-than-1 atm pressure level would be an unnecessary measure to be addressed to a preliminary design study, since it would not appreciably alter the chosen loading configuration.
Dream Chaser main engines abort thrust value was estimated assuming the same 8 g acceleration as for HL-20 would impact on the whole mass of the spacecraft (i.e., launch mass), therefore coming to a $T_{abort} = 9,81 \times 8 \times 9000 = 706.320\,\mathrm{N} \approx 71$ tons of total thrust evenly imparted by the two engines. Section 6.1 provides further explanations regarding the applied boundary conditions.

4.3 2,5-g Subsonic Aerodynamic Pullup Maneuver

Once the spacecraft reaches the lower part of the atmosphere and is approaching the runway, a pullup maneuver is needed to recover from the steep descending path and level the spaceplane for the successive landing phase. During a nominal mission, this maneuver almost propellant-free; also, payload or crew mass may have changed. The worst case is when the pullup

maneuver is performed after an on-pad abort and the spacecraft is approaching the runway from the peak of the abort trajectory. In this case, all the fuel, cargo and crew are on board, yielding the maximum inertial forces on the vehicle. The pullup load condition is therefore analysed by considering the worst-case scenario of an on-pad abort with 2, 5 g acceleration acting normally to the vehicle.
The lift generated by the spaceplane is $L = 2,5 \times 9,81 \times 9000 = 220.725\,\mathrm{N} \approx 22\,\mathrm{tons}$. Drag generated during this phase was assumed to be 20% of the net lift, therefore $D = 0,2 \times 220.725 = 44.145\,\mathrm{N} \approx 4,4$ tons acting along the vehicle longitudinal axis. The loading scheme is shown in figure below.

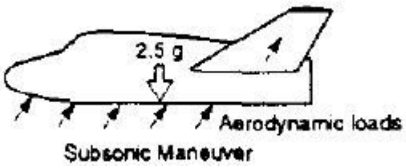

Figure 4.2: Loading condition during 2.5 g pullup maneuver (adapted from [3]).

The rational of pullup analysis is because this maneuver yields the **design condition for the fin inner structure and root section attachments**, since the aerodynamic loads, especially lift, are predominant. Design procedure is explained in subsection 5.2.4 and then verified through FEM analysis in section 6.1.

Chapter 5

Structural Analysis

The following three chapters represents the core of the overall project report. Here, the analytical, CAD and FEM techniques we utilized to determine the integrity of the proposed Dream Chaser structural arrangement are presented.
Our primary concern was the assessment of the structure ability to resist local mechanical failure modes and global buckling when subjected to aerodynamic and inertial loading found during the mission. Therefore, we attempted to identify the major load paths and critical areas of the vehicle that are stressed beyond the limits of construction materials. Chapter 5 shows the geometrical modelisation through the use of CATIA V5 R20 software, as well as some hand calculations. FEM and FEA discussions are addressed to Chapter 6, where ANSYS R18.1 MECHANICAL tool was used within Ansys R18.1 Workbench. Chapter 7 is, finally, devoted to the presentation of postprocessing results evaluation and model improvements.

5.1 Fundamental Premise to our Approach

Dream Chaser is synonym of versatility and safety. To fulfil these needs, it incorporates the most advanced manufacturing techniques for composite materials that led to the creation of a masterwork of space engineering. To do justice to its great complexity and coolness, we were compelled since the very beginning to do things right, without blindly rushing into the CAD representation (and subsequent FEA).

We must remark that our persistent approach has always been to derive, wherever possible, meaningful and useful informations on structural members behaviours from the available theoretical background of Structural Mechanics, apply verification criteria, **and only after** to question the software tools for verifying the accuracy of our predictions. In other words, we have never tried to shout out random numbers trying to guess things. Conversely, we paid much attention in making the right decisions and taking the right assumptions so as to match as close as possible the actual Dream Chaser design. Of course, many times we had to do it ourselves (for well-known reasons), but always trying to balance between the requested amount of details for a preliminary design evaluation and the struggle to accomplish the most realistic rendering possible. Indeed, it took months of efforts, but in the end the hard work paid off.

5.2 Geometrical Modeling

Since the beginning, we were aware that our model would have not been unique, in the sense that every little modification would have eventually affected the whole final results. Thus, we have always taken a critical look at our model, considering it more like a through-point driven by the many changes we had to produce accordingly to the actual needs, and not a final objective to be reached. Nevertheless, by virtue of our professional aptitude and personality, we sought out the most faithful representation possible, since at that moment we had acquired the necessary expertise and confidence in CAD design to deal with such a complex structure. Besides, we lacked of sufficient experience to assess *a priori* the impact of gross approximations on final stress results. So, it was our exercise purpose to learn how to understand where to stop or push forward.

Concerning geometrical modeling, we had no data nor detailed specifications, so we had to rely on available pictures and video clips found on the web. In principle, the fundamental theories learnt during the course were not applicable to our structure, since it is fully made up of composites, for which the idealisation of hyperelastic, linear, isotropic and homogeneous material would represent a too dramatic approximation. However, we had to exploit such properties of equivalent materials in order to perform our simulations during FEM and FEA, to be able to guess real trends of structural members behaviours (i.e., deformation modes, stress patterns, load paths, etc.) and, above all, the order of magnitudes of quantities we were dealing with.
Thus, after having collected many hours of observation, we performed a reverse engineering approach to bring out **our concept** of the Dream Chaser spacecraft. This was done by means of our intuitions and well-thought reasoning, basing our design approach on the structural functionality the various members have to fulfil in order to ensure structural stability, stiffness and strength.

Modeling was based on physical properties of plates and membranes for surfaces (e.g., skins, shells, ribs and spars webs), while beam properties were adopted for solid bodies (e.g., spars caps and keel beams). This distinction was done by bearing in mind how the FEM and FEA softwares would have later worked, since they treat objects as beam (1D), shell (2D), or brick (3D) elements. All physical properties were initially set at a minimum practical manufacturing standard (±10%)[15]. Where needed, some gauges were increased through sizing loops (see Chapter 6) to prevent failure, while the others remained unchanged where cases of low loading displayed.

5.2.1 Primary Structure Components

A top-down approach was performed to start modeling our vehicle. The geometrical methods being used came from our academic knowledge of technical drawing and aerospace structures design. As already mentioned, CATIA V5 R20 was used.
Dream Chaser cutaway showed in Fig.2.3 was our starting point. The three views were imported in Catia *Sketch Tracer* environment, correctly positioned with respect to each other at the right points. Dimensions of static envelope were then set as our modeling reference frame.

Pressurised Module

The pressurised crew cabin was the first element we began to deal with. It was realised in two halves to exploit axial symmetry in the first section, while an *ad hoc* design was performed for the module nose. The longitudinal profile was sketched, as well as, the most relevant geometrical discontinuities (e.g., cross-section variations), and spline curves to get the final 3D representation. Finally, on Catia *Generative Shape* environment, the module surface was carved out from the solid body.

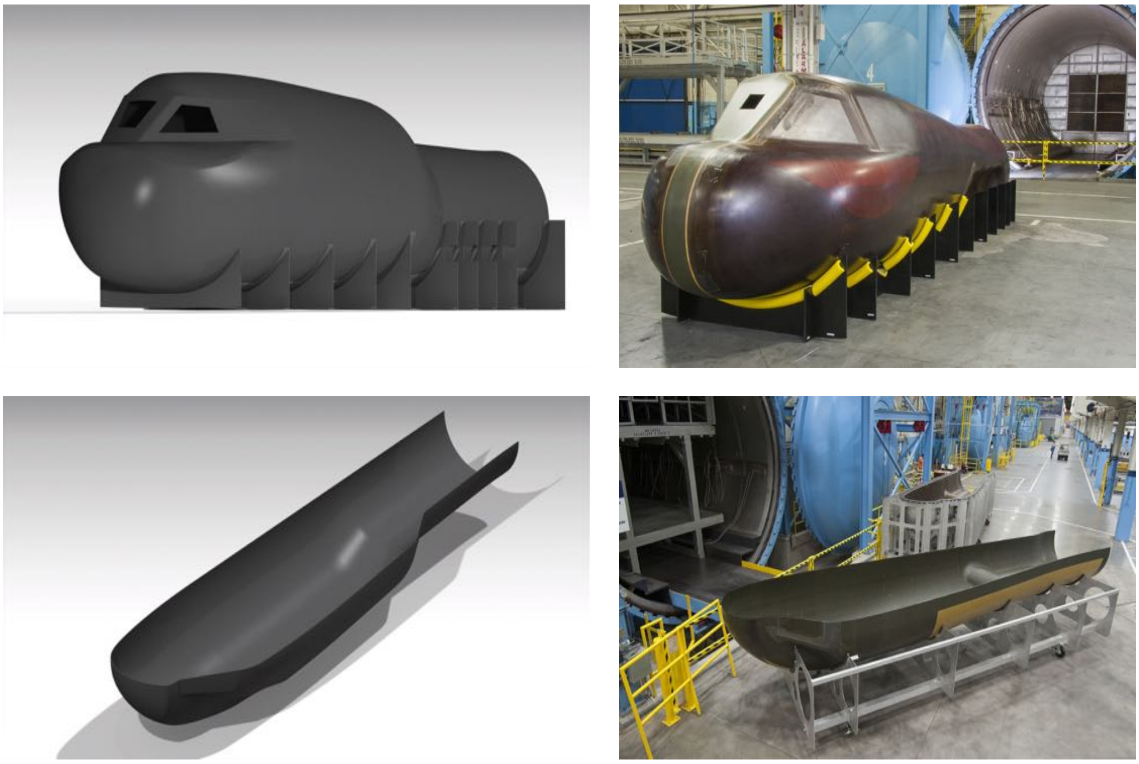

Figure 5.1: Pressurised Module rendering (left) vs. real manufactured piece after curing (right).

Fuselage Ribs

Dream Chaser features two kinds of fuselage ribs:

- *Front ribs*, from 1 to 8
- *Aft ribs*, from 9 to 13

The shapes of the former eight ribs retrace the unique vehicle outer shape line from its interior, thus primarily serving aerodynamic purposes. The latter five ribs are the most critical one, since they have to provide the necessary structural strength and stiffness to carry wings loads, redistribute them to the rest of the structure, and resist the huge launch and abort normal thrust. All of their cross-sections are of channel type (i.e., “C”-shaped). This fact should not amaze the reader because it is a typical configuration encountered on conventional aircrafts, in that it is particularly suitable for transferring wings moments via differential axial stress inside the ribs flanges and in-plane shear flows.
Within Catia, fuselage ribs were modeled like solid bodies in the *Part Design* environment.

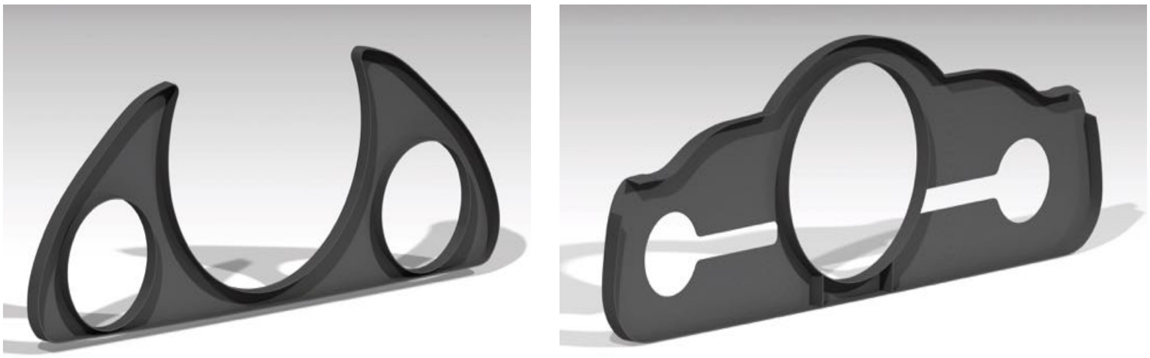

Figure 5.2: Fuselage rib n°6 (left) and 10 (right).

Fuselage Skin

Fuselage skin was probably the most difficult piece we had to model. We had to search a lot to find a way to sketch its complex shape, but in the end we managed to do that once having found a *step* file on the Internet meant for 3D-printing of a Dream Chaser mould.
We imported it in Catia, converted, scaled up to full-size, and then exploited the intricate lattice of shaping lines (step files are visualized like FEM models) to re-build spline by spline the most accurate shape possible. Indeed, this was a very draining procedure, but the final result worthy represents Dream Chaser look. The whole CAD design took place in the *Generative Shape* environment.

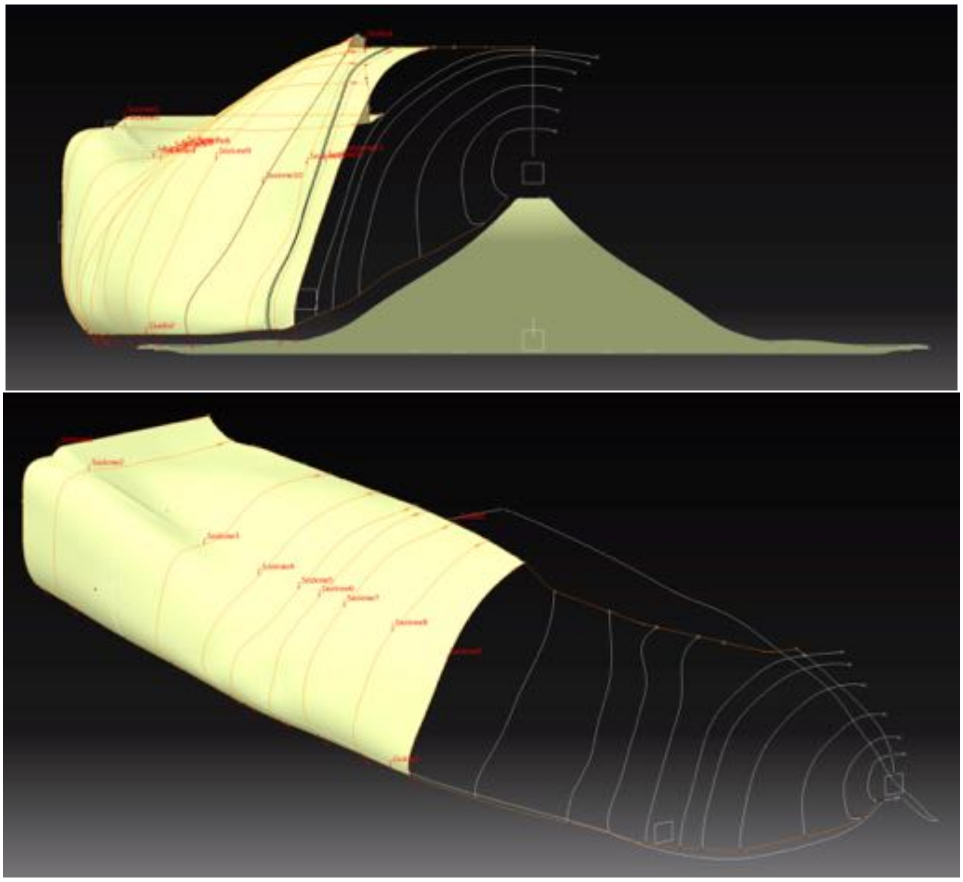

Figure 5.3: Representation of fuselage skin reference splines.

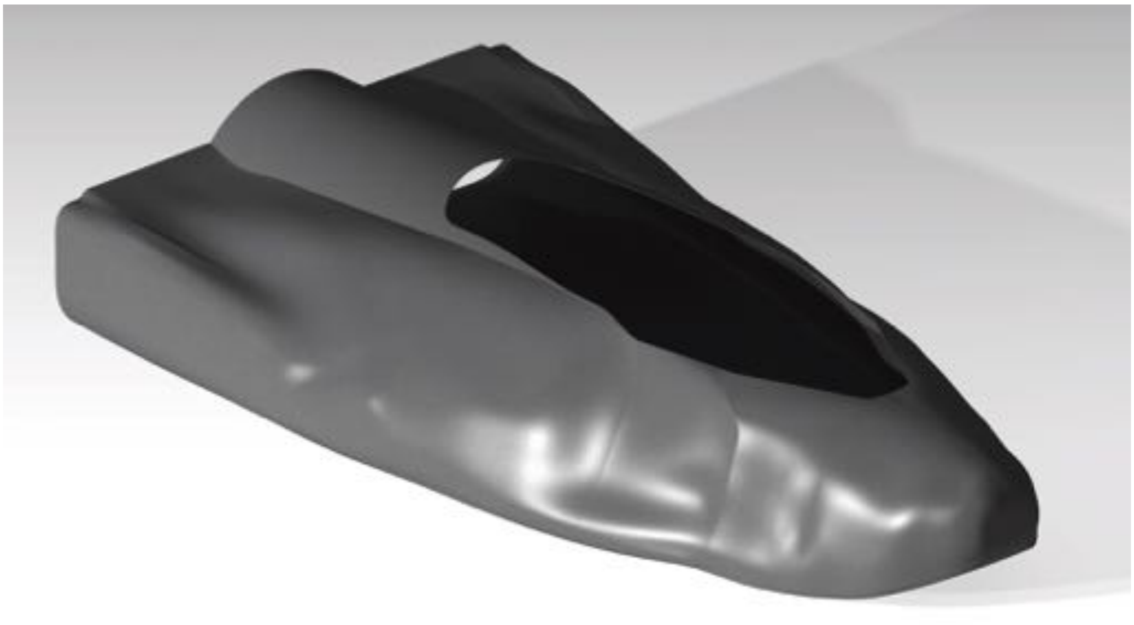

The assembly of primary structure frame is shown in the figure below:

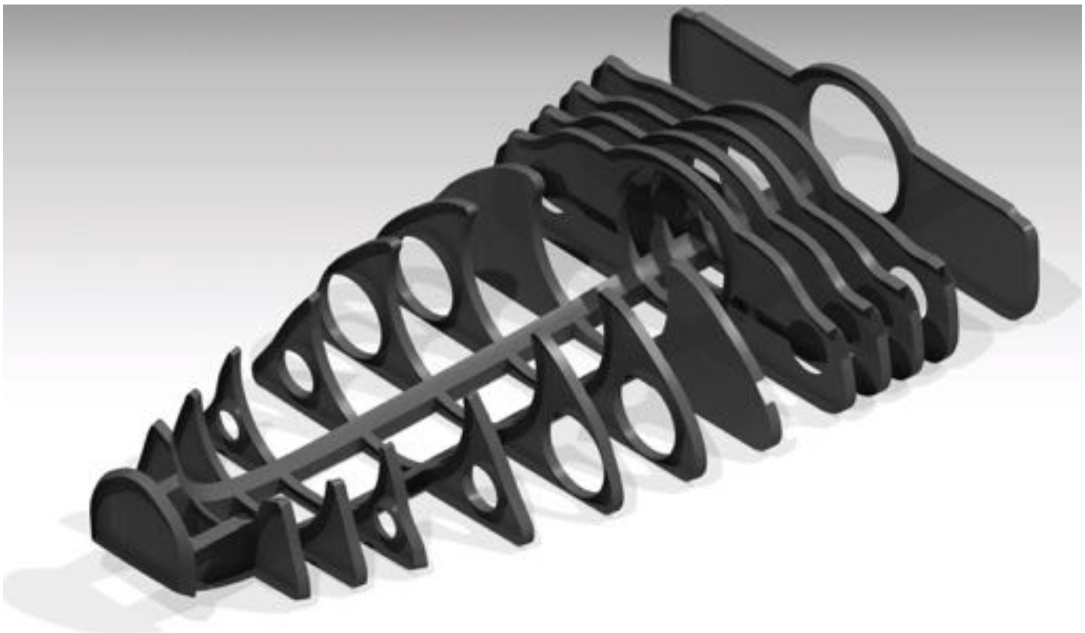

Figure 5.4: Primary structure frame assembly (ribs+keel beams).

5.2.2 Secondary Structure Components

Wings

The aerodynamic forces of a lifting body are generated mainly by the shape of the body itself and most of proposed concepts have no conventional wings to generate lift.

The so-called outboard fins mounted on the Dream Chaser changes the conventional configuration of a lifting body. they are used to generate half of the total lift needed to perform the atmospheric flight [21] and increase the longitudinal stability. Elevons are mounted on the trailing edge of the fins which are used , together with upper aft-body flaps, to produce the pitch control moment.

The geometry of the outboard fins were obtained from references [16], [22] and [23]. These data are for HL-20's fins but it was assumed that similar geometry would be the same for Dream Chaser. Fin planform geometry is a back swept-wing-like shape, They are mounted on the outboard aft-body part with a dihedral angle of 50°. They are tapered along the span with a swept symmetric airfoil, NACA 0008 at root section and NACA 0012 at tip. For the sake of geometrical modeling simplification, the incidence and toe-in angles of the fins are assumed to be zero. These values were not available in literature for the final configuration of the Dream Chaser, only those for HL-20 were present in references which are 6.6° and 1.25° respectively.

The inner structure of the fins were not known during the development of this work and we developed our structural concept based on a conventional tapered wing box with multiple spars and ribs and no stringers. From images of reference [24] and others found on web, we estimated a number of five wing spar. The placement of each spar within the wing is constrained by the frame pitch, frame number 8 to 12 have joining components to fasten wing spars on the lifting body main structure. This translates into a fixed distance of each spar from leading edge at wing root section. Each spar axis has been tilted in order to get at the tip the same distance ratio of spar built-in section. After geometry definition the fin has been modeled in CATIA and consequently, it was possible to obtain measures of the cell area and wall length for the root section. This data will be required for walls and skin sizing in the next part. Figure 5.5 shows a sketch of fin planform geometry with spar arrangement and table 5.1 lists the main fin's geometry specifications obtained during preliminary studies.

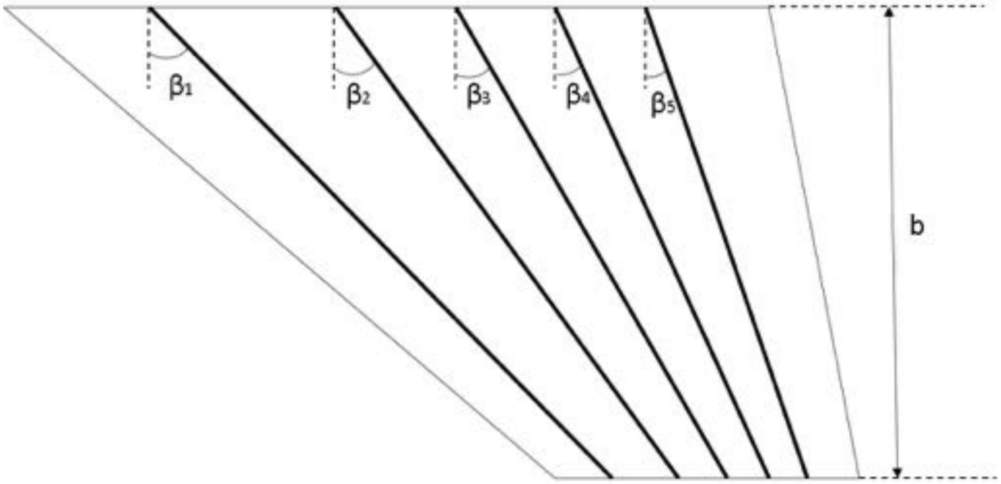

Figure 5.5: Scheme of fin's geometry and inner structure (without ribs).

Wingspan (mm)	**Root chord length** (mm)	**Tip chord length** (mm)	**Dihedral angle** (deg)	**Incidence angle** (deg)	**Toe-in angle** (deg)
2637	3000	712	50	6.6	1.25

Table 5.1: Fin main geometrical data.

Based on common wing box design, we decided to shape the front and rear spar with C cross section, while central spars with I section. The wing box sizing is done in section 5.2.4. Rib orientation is uniform and parallel to the spacecraft's longitudinal axis. Rib number and pitch have been derived in order to ensure structural stability of wing spars, the procedure is explained in section 5.2.4. Figure 5.6 shows the geometry of root section which will be used in the design process on section 5.2.4. Table 5.2 lists dimensions of spar pitch, closed cell area and wall length.

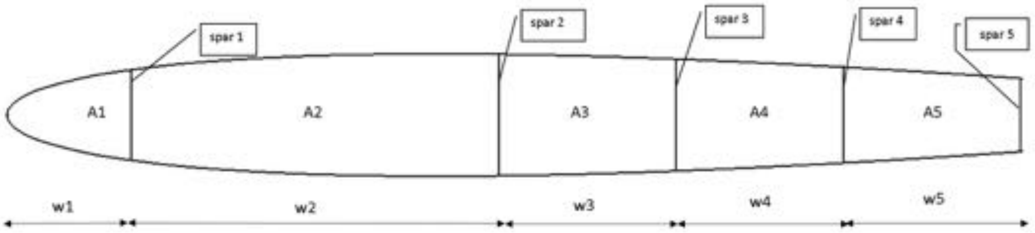

Figure 5.6: Fin root section geometry.

Spar (mm)	**Height** (mm)	**Pitch** (mm)	**Sweep angle** (deg)	**Cell area** (m^2)		**Wall length** (mm)	
1	177	260	52	A_I	0.032	l_{110}	569
2	239	770	46	A_{II}	0.173	l_{12}	771
3	220	370	44	A_{III}	0.085	l_{23}	370
4	188	350	41	A_{IV}	0.072	l_{34}	350
5	144	370	40	A_V	0.062	l_{45}	371

Table 5.2: Dimensions of fin root section (wall length are referred to the symmetric upper part of the airfoil).

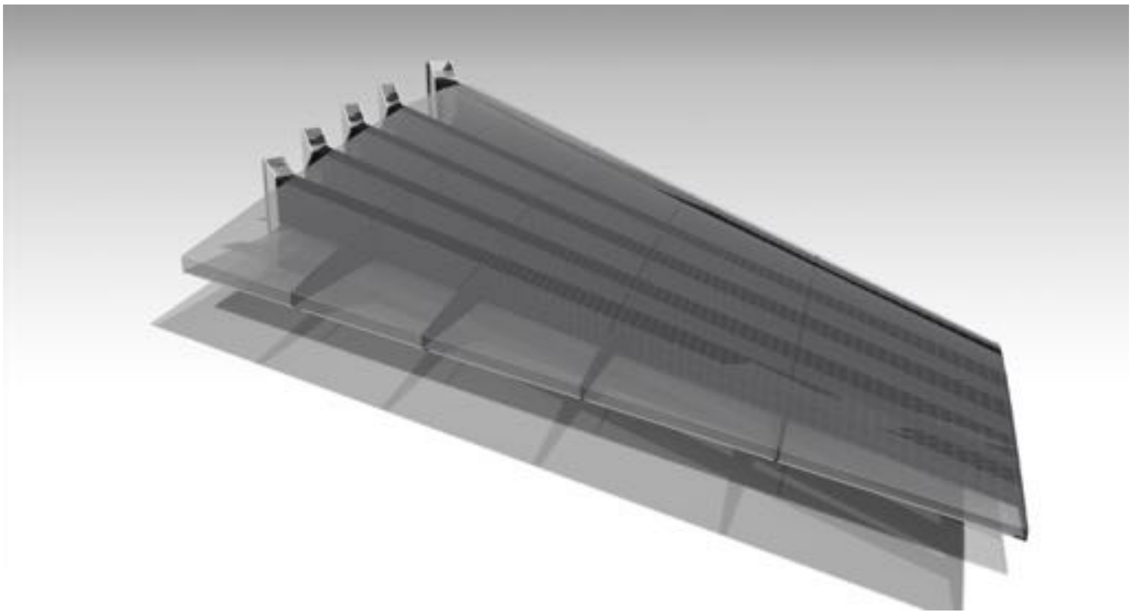

5.2.3 Other Components

Nonstructural elements are very important to model, because they introduce inertial forces into the structure when coupled with vehicle accelerations. Among the overall masses representing the various subsystems (positioned within the structure consistently with the subsystem packaging arrangement in Fig.2.3), we decided to account only for the most meaningful for a preliminary structural design, such as tanks and crew module floor.
A total of ten cylindrical tanks with hemispherical heads was modeled in Catia *Part Design* environment, so we could simulate their inertia later in the FEA. The pressurised module floor was modeled to account for the crew weight, and how this is transferred to the rest of the Dream Chaser.

5.2.4 Fin Structural Design

Critical loads acting on outboard fins are caused mainly by aerodynamic forces. Fuel is placed within the main body structure therefore no significant inertial load will act on the structure. The only contribution in terms of mass is from the actuation system of the elevons, in this preliminary analysis is assumed negligible.

As already explained in section 4.3, the pullup loads have been chosen as limit load for fin's structural sizing. Due to lack of information regarding the aerodynamic characteristics of fin solely, only the lift is considered in the analysis. The lift is modeled as a uniform distributed load per unit surface with a resultant of 55181 N applied at half wingspan. The line of action is assumed to be normal to fin's surface but in reality, lift will have a component normal to fin's surface and the other parallel due to dihedral angle. This modified load condition is heavier than real therefore getting a conservative sizing of wing spars.

The fin is modeled as box beam, tapered along z axis and clamped at root section. Clamped section has been chosen as design section for sizing the beam box since it is the most stressed. The cross-section is a NACA 0008 symmetric airfoil without the structural contribution of the trailing edge. Each spar is idealized as lumped parameter model with booms that absorbs direct stresses and walls effective only in shear. Also the skin is modeled as carrying only shear flow. Figures 5.7 and 5.8 highlight the structural model introduced above. Based on the simple clamped beam model for the fin we can evaluate the reaction force and bending moment at clamped section, $R_y = -L_{fin}$ and $M_{xroot} = 72757Nm$. Spar dimensions and skin thickness will be considered uniform spanwise after sizing process. A following analysis would optimize spar's geometry along their span, tapering the cross-section dimensions according to stresses found in this work. This optimization process is out of the scope of this project and will be left as detailed analysis phase.

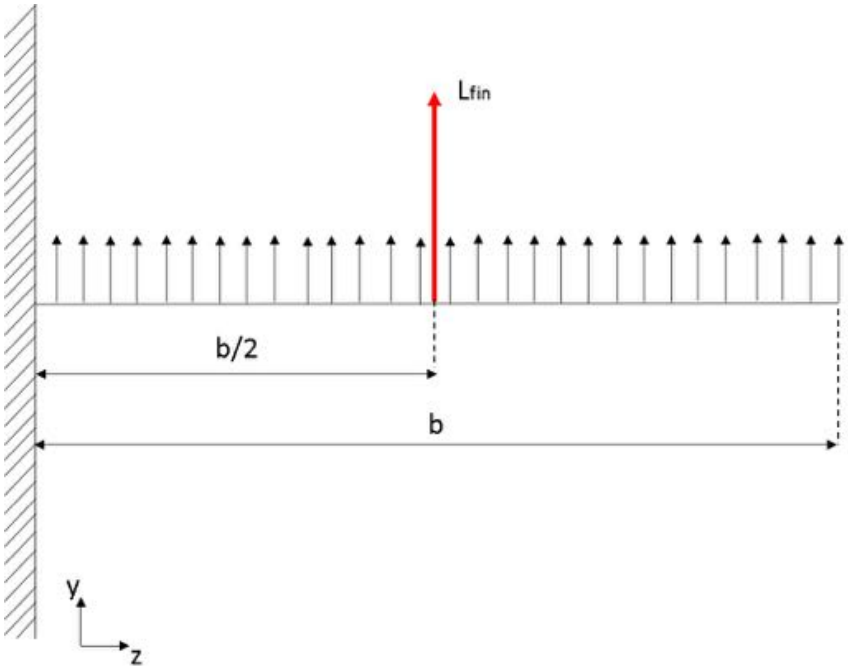

Figure 5.7: Beam model of the fin with total lift applied at half of wingspan.

This simple structural model doesn't allow to catch the real behavior of an orthotropic material like composites, therefore some simplification are needed. The material is modeled as isotropic with elastic properties equal to that along direction 0. Stresses on booms are expected to be symmetric, namely compressive stresses for upper booms and tensile stresses on lower one. Given the fact that compressive strength property of the material is lower than tensile strength, this one has been chosen to be the strength property of the equivalent isotropic material. This conservative assumption allows to obtain a design based on the critical component which are the compressed booms.

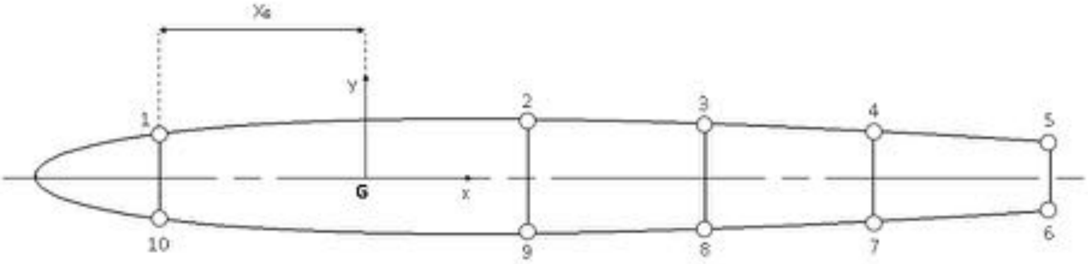

Figure 5.8: idealized root section of the fin symmetric along x

Dream Chaser vehicle falls within the category of man-rated commercial spacecraft. Flight authorities and space standardization organizations for both US [12] and Europe [17], don't supervise design & test processes nor flight operations of such space product category. The factor of safety used from here through this work is completely our judged assumption and this could be disapprove once the relevant organization will regulate the commercial use of space for man-rated spacecrafts. The factor of safety used in this project is 2.5 and is applied for all design processes hereafter.

Boom area has been the first design process for wing box sizing. Each boom area will be used to design spar caps dimensions that are assumed to carry all the direct stressed coming from bending. Due to swept geometry of the wing box, a boom will be loaded along z and x with opposite sign with respect to symmetry axis. From bending theory and considering the sweep angle of each spar, the forces acting on i-th boom are given by formula:

$$P_{zi} = \pm \frac{M_{xroot} h_i}{2J_{xx}} A_i \tag{5.1}$$

$$P_{xi} = P_{zi} \tan \beta_i \tag{5.2}$$

$$P_i = \frac{P_{zi}}{\cos \beta_i} \tag{5.3}$$

$$\tag{5.4}$$

where P_{zi}, P_{xi} and P_i are respectively load along z, x and along boom axis. h_i and A_i are

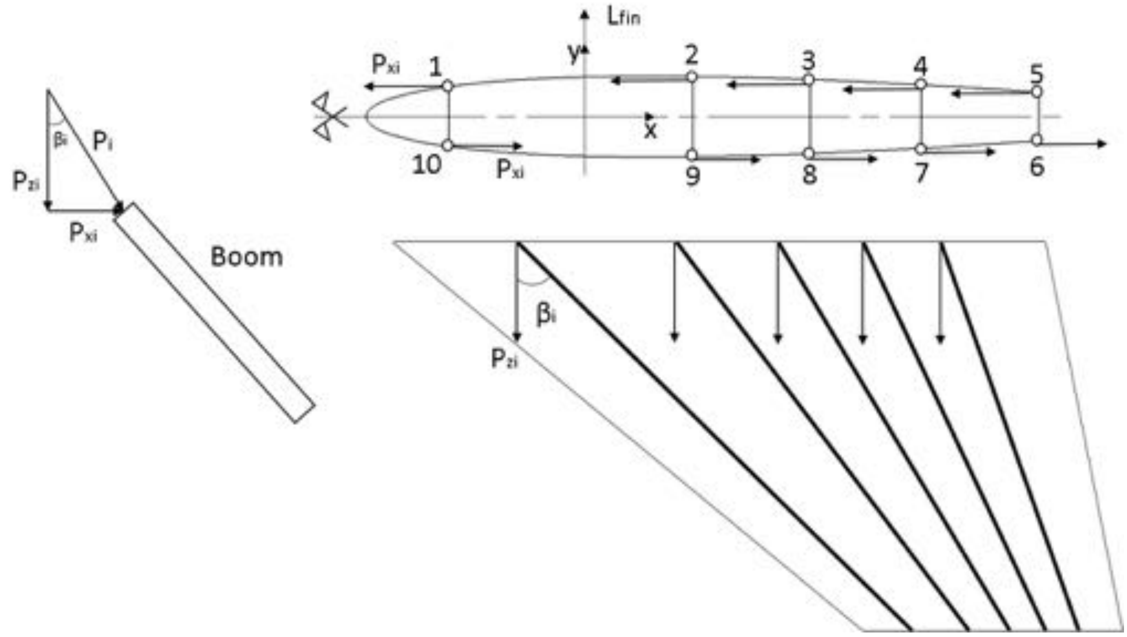

Figure 5.9: forces due to ending acting on each boom

boom height, that coincides with spar height, and boom area. Direct stress on a boom is simply yhe ratio of P_i and A_i. Booms idealize also the total inertia of the section and it is distributed on each center of mass. The moment of inertia and x coordinate of center of mass for root section, evaluated from wall 1_10, are given by formula:

$$x_G = \sum_{i=1}^{5} \frac{A_i x_i}{A_i} = \frac{1}{\sum_{i=1}^{5} A_i}[A_2 w_2 + A_3(w_2 + w_3) + A_4(w_2 + w_3 + w_4) + A_5(w_2 + w_3 + w_4 + w_5)] \tag{5.5}$$

$$J_{xx} = \sum_{i=1}^{10} A_i \frac{y_i}{2}^2 = \frac{1}{2}(A_1 h_1^2 + A_2 h_2^2 + A_3 h_3^2 + A_4 h_4^2 + A_5 h_5^2) \tag{5.6}$$

Boom area appear coupled and non-linearly in previous equations. To simplify the analysis, the sizing process has been divided into two step. First, moment reaction was distributed equally on each spar, thereby getting a single equation only in A_i. Second, once all boom area are known, stress evaluation on each element has been done to assure material strength. The evaluation of boom area in the first step has been done imposing that compressive stress must be less than the allowable strength of the carbon woven.

$$\begin{aligned} \sigma_i &= \frac{M_{xroot} h_i}{5 J_{xxi} 2 \cos\beta_i} \leq \frac{F_{cu}}{k} \Rightarrow \\ \Rightarrow A_i &= \frac{M_{xroot} k}{5 F_{cu} \cos\beta_i h_i} \end{aligned} \tag{5.7}$$

where $J_{xxi} = A_i \frac{h_i^2}{2}$ is the moment of inertia of a single spar, k is the safety factor and F_{cu} is the compressive ultimate strength of the material. After that stresses on booms for the overall root section has been verified. Table 5.3 summarize previous design process with chosen cross section dimensions for spar caps in terms of width and thickness.

Boom	**Boom area** (m^2)	P_{zi} (N)	P_{xi} (N)	P_i (N)	**Width** (mm)	**Thickness** (mm)
1	6.56×10^{-4}	-8.598×10^{4}	-1.101×10^{5}	-1.397×10^{5}	100	7
2	4.30×10^{-4}	-7.620×10^{4}	-7.891×10^{4}	-1.097×10^{5}	55	4
3	4.51×10^{-4}	-7.359×10^{4}	-7.106×10^{4}	-1.023×10^{5}	56	4
4	5.04×10^{-4}	-7.014×10^{4}	-6.097×10^{4}	-9.294×10^{4}	60	4
5	6.48×10^{-4}	-6.995×10^{4}	-5.798×10^{4}	-9.021×10^{4}	68	4

Table 5.3: results of boom area sizing with forces acting on them and cross section dimensions of each spar caps

Shear stresses generated by lift are carried by wall section, these are considered thin and theory of closed thin-walled section under shear load will be applied. In the lumped model for the root section, shear flow is constant along each wall and is the sum of base shear flow q_b and correction flow on each cell q_0. Base shear flow is the contribution of the total flow coming from the opened section. Taking advantage of the symmetry and cutting the upper skin panel, the base shear flow is different from zero only in vertical webs. Base flow is given by:

$$q_{bij} = -\frac{S_y}{J_{xx}} \sum_j A_i \frac{h_i}{2} \tag{5.8}$$

where $S_y = L_{fin}$ and the shear flow is evaluated along each web identified by two consecutive boom. q_{bij} is the shear flow taken as positive from boom i to boom j. Corrective flows are constant along cell webs and generate torsion due to the misalignment of shear line of action and shear center. From torsion theory the rate of twist of the section is related to shear flow by the formula:

$$\frac{d\theta}{dz} = \frac{1}{2A_kG}\oint_k \frac{q}{t}\,ds \tag{5.9}$$

where $q = q_b + q_0$, A_k is the area of k-th cell and G is the shear modulus of the material. In addition to corrective shear flow, also the x component of boom force generate torsion. The values of q_0 are given by equating external torque and torque generated by total shear flow evaluated with respect to middle point of web 1_10:

$$S_y(x_G - w_1) = \sum_{k=1}^{5}\oint_k q_b p\,ds + \sum_{k=1}^{5} 2A_k q_{0k} + \sum_{k=1}^{5} h_k P_{xk} \tag{5.10}$$

Combining previous relations we get a set of 5+1 equations in the unknown q_{0k}, $\frac{d\theta}{dz}$, skin and spar web thicknesses:

$$\begin{cases}
\frac{d\theta}{dz} = \frac{1}{2A_IG}[q_{0I}\frac{l_{le}}{t_{skin}} + (q_{0I} - q_{b1-10})\frac{l_{110}}{t_1}] \\
\frac{d\theta}{dz} = \frac{1}{2A_{II}G}[-q_{0I}\frac{l_{110}}{t_1} + q_{0II}(\frac{l_{12}}{t_{skin}} + \frac{l_{110}}{t_1} + \frac{l_{910}}{t_{skin}} + \frac{l_{29}}{t_2}) - q_{0III}\frac{l_{29}}{t_2} + q_{b110}\frac{l_{110}}{t_1} - q_{b29}\frac{l_{29}}{t_2}] \\
\frac{d\theta}{dz} = \frac{1}{2A_{III}G}[-q_{0II}\frac{l_{29}}{t_2} + q_{0III}(\frac{l_{29}}{t_2} + \frac{l_{23}+l_{98}}{t_{skin}} + \frac{l_{38}}{t_3} - q_{0IV}\frac{l_{38}}{t_3} + q_{b29}\frac{l_{29}}{t_2} - q_{b38}\frac{l_{38}}{t_3}] \\
\frac{d\theta}{dz} = \frac{1}{2A_{IV}G}[-q_{0III}\frac{l_{38}}{t_3} + q_{0IV}(\frac{l_{34}+l_{87}}{t_{skin}} + \frac{l_{38}}{t_3} + \frac{l_{47}}{t_4}) - q_{0V}\frac{l_{47}}{t_4} + q_{b38}\frac{l_{38}}{t_3} - q_{b47}\frac{l_{47}}{t_4}] \\
\frac{d\theta}{dz} = \frac{1}{2A_{IV}G}[-q_{0IV}\frac{l_{47}}{t_4} + q_{0V}(\frac{l_{45}+l_{76}}{t_{skin}} + \frac{l_{47}}{t_4} + \frac{l_{56}}{t_5} + q_{b47}\frac{l_{47}}{t_4} - q_{b56}\frac{l_{56}}{t_5}] \\
S_y(x_G - w_1) = (q_{b29}w_2 + q_{b38}w_3 + q_{b47}w_4 + q_{b56}w_5) + 2\sum_{k=1}^{5} A_k q_{0k} + \sum_{k=1}^{5} h_k P_{xk}
\end{cases} \tag{5.11}$$

The previous set of equations has been implemented in a routine on MATLAB to calculate web thicknesses iteratively, starting from a first guessed value. Convergence is reached when the difference of thicknesses of each web, for two consecutive iteration, is less than a tolerance. The script is reported in appendix. For the sake of manufacturing some thicknesses have been increased, the output of the routine and real dimensions are listed in tables 5.4a and 5.4b.

Web	**Thickness** (mm)
l_{le}	2.56
l_{110}	3.7
l_{12}	4.96
l_{29}	0.9
l_{23}	3
l_{38}	2.7
l_{47}	2
l_{45}	3.42
l_{56}	2.4

(a) Routine output.

Part	**Thickness** (mm)
skin	5
spar web 1	4
spar web 2	2
spar web 3	3
spar web 4	2
spar web 5	3

(b) Skin and spar web thicknesses.

Table 5.4: Output of the iterative procedure and actual thicknesses of spar webs and skin.

The last step for wing box sizing was the determination of rib number and their design. As already explained, one of the tasks of wing ribs is to ensure structural stability for wing spar and skin panel. For a preliminary approach the analysis has been focused on spar stability with the aim of finding the rib pitch that prevent column buckling of wing spar. Spar are modeled as Euler column, clamped at root section, and subjected to the same compressive load acting on compressed boom calculated in the previous analysis. The highest compressive load is on the first spar, satisfying the stability of this spar we are confident that also the others are stable. Compressive load acting on boom 1 is assumed to be constant spanwise and acting on tip section directed along boom axis. Lowest values have been chosen for moment of inertia and Young modulus, respectively $J_{min} = 1.26 \times 10^{-5}\,\mathrm{m}^4$ and $E_{min} = 7500MPa$. Moment of inertia of the cross section is evaluated on a direction perpendicular to spar web and Young modulus is equal to E_3 of the material. Equating the compressive load to the critical load and substituting the *effective length* for a clamped beam at one section and free on the other we get:

$$\begin{aligned} P_{cr} &= \frac{pi^2 E_{min} J_{min}}{l_0^2} = P_1 \Rightarrow \\ \Rightarrow l &\leq \sqrt[2]{\frac{pi^2 E_{min} J_{min}}{4P_1}} = 0.816 \end{aligned} \tag{5.12}$$

where l is the length that spar one must have to prevent buckling subjected to compressive load P_1. Rib number is evaluated by subdividing this length over the fin wingspan. Rounding to an integer, minimum rib number is 4. Two additional ribs have been inserted into the fin, one to get a closed section at tip and the other to obtain an equally spaced configuration of ribs along wingspan direction.

The connection of outboard fins with the spacecraft main body was the critical area of this work. Swept wing configuration is itself a complication for the design of wing fastening systems even for conventional aircraft. Additional complications arise in the presence of attachment angles along three different directions as in the case of Dream Chaser's fins. The attachment system must transfer the aerodynamic load from fin spars towards primary structure through body frames, each of which constrains a corresponding fin spar to body structure. The adopted configuration is composed of five fitting interface on each spar-frame patch. Each interface is formed by two half-parts, one fixed on fin spar root section and one on body frame plane. Body frame flange are cut off on that area in order to match the half-part on the frame face allowing fastening on it. The spar part has an encased housing that is the negative of spar root section so that a fitting area is created. Junction plates are present on both half-part, they are the matching parts that allow assembling of half-parts one to another. The tightening of half-parts assembly is fastened by a couple of screw bolts installed on opposite part of an assembled interface through holes made on junction plates. Junction plate on spar half-part forms a 90° angle between spar axis and plane of the plate. This arrangement transfer loads along spar axis without loading the latter in a direction normal to its axis, which would happen in a conventional lug configuration on a swept wing. Junction plate on body frame has the same form like the one on spar, receiving loads from it and directing towards primary structure by means of fastening on body frame. Main drawbacks of this configuration are the use of multiple components, with possible alignment problem during assembling phase, and load path concentrated on a restricted area. The latter disadvantage is reduced by using a large fitting area on body frame. Each half-part is fixed on respective structure by riveted joints. The attachment of half-parts are made by tension bolts that transfer shear and bending moment from spar to body frame.

Spar is fixed on the half-part using riveted joints. Fitting is made between spar caps and built-in of the half-part that encloses spar cap geometry using a simple lap joint configuration. The joint must transfer bending load coming from spar caps in an alternate way to the rest of the structure, this load is assumed equally distributed on each rivet. Shear load on each spar web is transferred by the body of the half-part towards screw bolts. Joining is done by using 3/16"

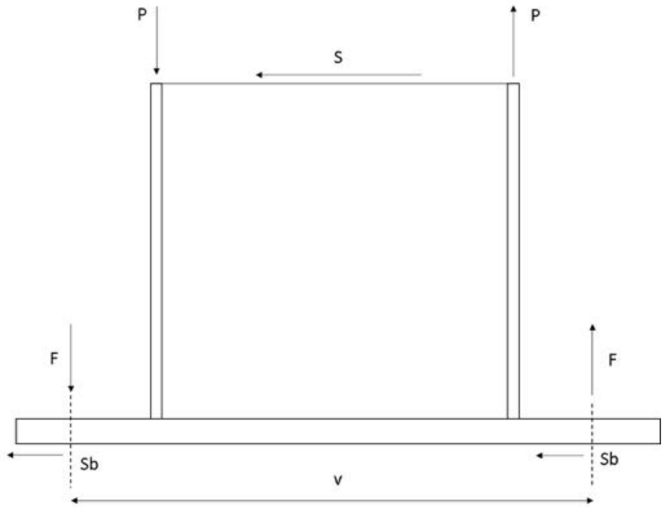

Figure 5.10: schematic draw of attachment system on fin spar with load path from spar to bolts

HI-LOK arranged in two row per each spar cap, this configuration applies both for C and I cross-section. HI-LOK datasheet gives the maximum shear load that a rivet can withstand, imposing also that P_i is distributed equally on each rivet row we get the number of rivet per each row by:

$$n_{bi} = \frac{P_i}{2F_{bmax}} \tag{5.13}$$

where F_{bmax} is the maximum shear force on rivet and n_{bi} is the number of rivet per row on $i-th$ spar. The thickness of lap joint plate is evaluated imposing that the drilled cross section must resist to direct stress.

$$\sigma = \sigma_y = \frac{P_i}{t_s(f_i - 2d)} \Rightarrow t_s = \frac{P_i}{\sigma_y(f_i - 2d)} \tag{5.14}$$

where σ_y is the yielding stress of 7075-T6, f_i is the plate width in the $i-th$ half-part and d is rivet diameter. Shear of the plate near free edge has been verified in order to get the distance between rivet hole and free edge. Force on the rivet near free edge is $\frac{P_i}{2n_{bi}}$ and is subdivided on the two section tangent to hole perimeter, the free-edge distance is:

$$e_{si} = \frac{P_i}{4n_{bi}\tau_y t_s} \tag{5.15}$$

Figure 5.10 shows loads acting on the two bolts. Bending moment given by the couple P_ih_i, is transferred by alternate tension and compression of opposite bolts. Force on a single bolt is calculated by the equivalence of moment couple $F_i = \frac{P_ih_i}{v_i}$, where v_i is bolt distance. This value is chosen according to different geometric requirements such as airfoil thickness and bolt assembling. After few attempts, the value $v_i = 1.3h_i$ has been selected. Shear on each spar is assumed to be equally subdivided on two bolts. Bolts are subjected to combined stress of shear and tension. The diameter can be evaluated from Von mises failure criteria, imposing that the equivalent stress is less than the ultimate stress of bolt material. The minimum cross section area of the bolt is:

$$A_{bi} = \frac{\sqrt{F_i^2 + 3S_b}}{\sigma_u} \tag{5.16}$$

From that, the evaluation of bolt diameter can be obtained.

The assembled junction plate will be subjected to the same alternate load action on bolts. As a consequence, each end of the plate is loaded with a force normal to its plane and in an anti-symmetric way depending on whether the bolt is on the suction side or on the pressure side of the fin airfoil. Plate ends are restrained on their other side to the half-part main body, they can be thought of as clamped plates on one side and free on the other three subjected to a concentrated force acting perpendicular to the main plane. For a preliminary design of the plate thickness, the Grashov's method has been used and applied on a single end of an half-part. Loads and boundary conditions for the method are; a normal uniform pressure on the schematized plate equal to the concentrated force transmitted by the bolt distributed over the contact area on the junction plate, three edge clamped and one free. Reference frame for the analysis is oriented with x axis along short edge and y axis parallel to the long one. Dimensions for the bolt housing are obtained from geometric requirements explained before in combination with results from bolt design, these are reported in table 5.5c. Distributed loads acting along x and y are obtained as follows

$$\begin{cases} p_x = p\frac{a^4}{kb^4+a^4} \\ p_y = p - p_x \end{cases} \tag{5.17}$$

where $k = 17$ is the constant representing the chosen boundary condition, a plate length along y and b length along x. From Grashov's method, the plate problem has been reduced to a two beam problem. Beam along x is a canted beam under load p_y, the other along y is clamped on each end subjected to load p_x. Maximum bending loads are $\frac{p_y b^2}{2}$ for the former and $\frac{p_y a^2}{8}$ for the latter, both happening on clamped section. Grashov's method assumes that the cross-section of the approximating beams have unitary width, therefore the moment of inertia of the cross section can be expressed as

$$J_{xx} = J_{yy} = J = \frac{M_{x;y}}{\frac{1\times t_a^3}{12}}\frac{t_a}{2} = \frac{6M_{x;y}}{t_a^2} \tag{5.18}$$

where the axis for the calculation of the moment of inertia changes depending on which beam is considered. In the actual geometry the cross sectional moment of inertia would be calculated with respect to plate main plane. Plate thickness is evaluated combining the maximum of bending moments between the two cases and the previous expression for moment of inertia, equal for the two beams. This procedure has been repeated for all the five fitting interfaces, results of the design process are summarized in table 5.5a, 5.5b and 5.5c

The dimensions of structural components obtained in this subsection have been used during CAD modeling of the Dream Chaser. Validation of the structural design explained above will be performed using Ansys FEM software; the analysis and results obtained will be covered in the next sections.

Interface	**Diameter** (mm)
1	24
2	22
3	22
4	20
5	20

(a) Bolt diameter (one pair per each fitting interface).

HI-LOK number	**Lap-joint width** (mm)	**Lap-joint depth** (mm)	**Lap-joint thickness** (mm)
24	100	90	8
20	55	77	12
16	56	62	11
16	60	62	9
16	68	62	7

(b) Spar to half-part fastening.

Plate	**Length** b (mm)	**Width** a (mm)	**Thickness** t_a (mm)
1	63	100	16
2	68	55	12
3	64	56	12
4	58	60	16
5	51	68	16

(c) Plate dimensions used for Grashov's method and evaluated thickness of the junction plate.

Table 5.5: Results of fitting interfaces design.

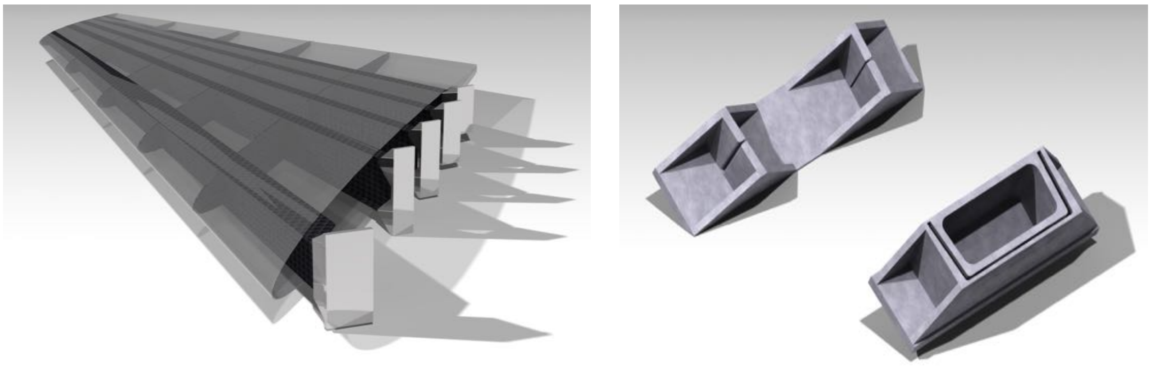

Figure 5.11: Renderings of entire wing and spar root fittings.

Chapter 6

Finite Element Analysis

6.1 Finite Element Modeling

Our FEM/FEA project-management tool was ANSYS WORKBENCH 18.1: it allowed us to handle the passing of data between ANSYS Geometry/Mesh/Solver/Postprocessing tools once imported the Catia-modeled geometry. Linear static structural analyses were performed by means of ANSYS MECHANICAL interface. The purpose was to evaluate the amount of load our structural elements could withstand without failing when the load is applied once (*strength analysis*). In our case, failure is rupture/collapse (ultimate failure) for composites parts, while permanent deformation (yield and joints shift) is referred to metallic bodies failure. Nonlinear static (large deflections theories) and dynamic simulations (harmonic, random vibration responses) are beyond the scope of this project, although necessary for predicting eventual fatigue or buckling failure modes. Fatigue investigations would be particularly suited for Dream Chaser, because of its high level of reusability.

Like geometrical modeling, and as already stated in Sec. 5.1, we looked at simulations results carefully and critically, by knowing the level of accuracy we were using to represent the level of structural complexity requested for a preliminary design evaluation. Moreover, at that time we were not as well educated as in the CAD area, therefore we had to learn day by day the background software theory and how to better exploit simulation tools Ansys made us available (references [10] and [13]). Indeed, this was kind of a learning process which eventually provided us strong confidence and high-level knowledge in the mastering of Ansys simulation methods.
For these reasons, our approach developed from top to down, that is incrementally raising the accuracy of our simulation predictions starting from very simple models, namely from the inner components of our proposed structure, finally getting to the global one. This procedure was carried out concurrently with CAD design, which means we had to refresh our geometry every time we wanted to perform a simulation. Anyway, our dedicated study prevented us from generating a cumbersome amount of them.

Mechanical Considerations on Materials

The starting-point of any kind of Ansys simulation consists in setting the material properties. This was accomplished by generating a standalone *Engineering Data* cell on the Workbench interface, so that every later simulations would have shared the same data source from our customised material library.

On this regard, we have to re-mark the important concept expressed in Sec. 5.2: apart from metallic components, **composites had to be treated as hyperelastic, linear, homogeneous materials**, for which equivalent mechanical properties in terms of Young modulus and Poisson ratio had to be assigned. This, of course, may represents a heavily-idealised situation in the aim of simulating the real behaviour of composites components, and we realised that straight away. Nevertheless, we could mitigate the impact of these strong assumptions by reasoning on how real structural members tend to deflect on applied loads.
As a matter of fact, the effect of aerodynamic loads during pullup maneuver is well-known, in that they tend to deflect the two canted fins upward, thus placing their lower skin in tension and the upper ones in compression. Besides, these loads tend to cluster at the leading edge because of the shorter load paths into the body structure. In addition, the unusual intersection angle of the wings and fuselage body introduces a canted load path in the body itself. These paths can be critical because of the abrupt change of curvatures found on the body surface.
A suitable carbon fiber orientation should be then readily planned during manufacturing of these components to assure the necessary material strength. Datasheets provide an IM7 carbon fiber yielding stress of $S_y = 2618$ MPa at 24°C and $S_y = 2550$ MPa at 177°C, which is Dream Chaser maximum operative temperature. This latter should have been our design failure stress, but we chose to use its 60% as design value. This decision came from the observation that maximum load distribution may occur when two fibers are placed 90° to one another, giving load components projected at 45° along each fiber. This entails a tensile loading of $\approx 70\%$ the total applied one. So, to be more conservative and given our lack of experience in composite materials, we took $S_y = 1530$ MPa as material input strength.

The following table summarises the complete list of materials we used for our spacecraft, where we decided to ascribe unidirectional and 3D woven properties to specific constituents, such as fin structural assembly (spars, ribs, skin) and fuselage assembly, respectively:

Material	**Density** (kg/m^3)	**Young modulus** (GPa)	**Poisson ratio**	S_y (MPa)	S_u (MPa)
7075-T6	2810	71,7	0,33	503	572
Ti-6Al-4V	4430	114	0,33	1100	1170
IM7 UD (CYCOM®5250-4)	1250	95	0,27	1530	1535
3D Woven (CYCOM®5250-4)	1250	70	0.27	848	850

Table 6.1: List of material used in structural analyses

This targeted and judicious way to assess things allowed us, in the end, to get useful insights on structural deformations and failure modes.

Masses Distribution

Upon materials assignment, we found out our vehicle structure to weight approximately 1984 kg, about 22% of the entire spacecraft. This result was actually in line with our expectation, as concurrently displayed by the HL-20 preliminary design analysis carried out in reference [2]. Thus, 7016 kg had to be properly distributed all around the Dream Chaser structural arrangement. We made that by assuming a crew mass of 560 kg (80 kg for each passenger), while the remaining mass was spread on fuselage ribs, tanks, keel beams and module floor. In this way, we eventually reached the final 9000 kg in order to accurately represent the vehicle inertia.

Contacts

Once having prepared the entire geometry, we passed to Ansys *Mechanical* environment to set up preprocessing steps. Firstly, we **manually** assigned contacts between each members common interface. This “by hand” procedure was unfortunately unavoidable, since Ansys could not manage to automatically detect and define the right contact regions due to our structure complexity.
Every contact was bonded-type, that is surfaces are fixed to one another so no gaps can open and no sliding takes place. In this way, we could properly simulate bonding behaviour and load transfers across the whole structure.

Mesh

Meshing our structure was a crucial step, so we had to pay particular attention on creating the right solution domains as far as our computing power would have let us. This was our inherent limitation during the execution of the various simulations we are going to present shortly.
Ansys provides both global and local meshing controls to allow the users sizing and refining the mesh to the desired quality prior an analysis run. First of all, we used the *Contact Sizing* tool to generate similar-sized elements on contact faces for face/face or face/edge contact regions. This actually was the most important device we exploited to correctly simulate load paths inside the structure. Next, since every structural member exhibited a curved shape, we used a *Curvature* size function with *Medium* Relevant Center, *Fast* Transition and *Fine* Span Angle to effectively approximate curves with small curvature radii (e.g., fins skin leading edge). For the latter, a 15° Curvature Normal Angle was used. Moreover, Max Face Size and Max Tet Size were set to 100mm with a default Growth Rate of mesh elements. This was done in order not to run already out of RAM memory, having a wide enough mesh grid to be resized on purpose wherever needed, as for few elements. In fact, we locally refined mesh elements size imposing 80 mm for tanks, 35 mm for all contact sizings, and 50 mm for wings frame. Such control parameters provided us a good global mesh quality for the overall structure (see Fig. 6.1), but we forcasted several changes were to be made depending on the type of specific simulation we wanted to carry out. Particularly, simulations of few components allowed us to thicken the mesh locally, so as to predict more accurate analyses results (see Fig.s 6.2, 6.3, 6.4, 6.5, and 6.6).

Adopted meshing functions exploited a Patch Conforming method for 3D bodies, because a Patch Independent algorithm would be preferable where many small surfaces (with respect to the model dimensions) are present. Inflation and Pinch controls along boundaries and edges were in turns automatically executed to provide local topology continuity of mesh elements. Multizone Quadrilateral/Triangles method was used for 2D surfaces.

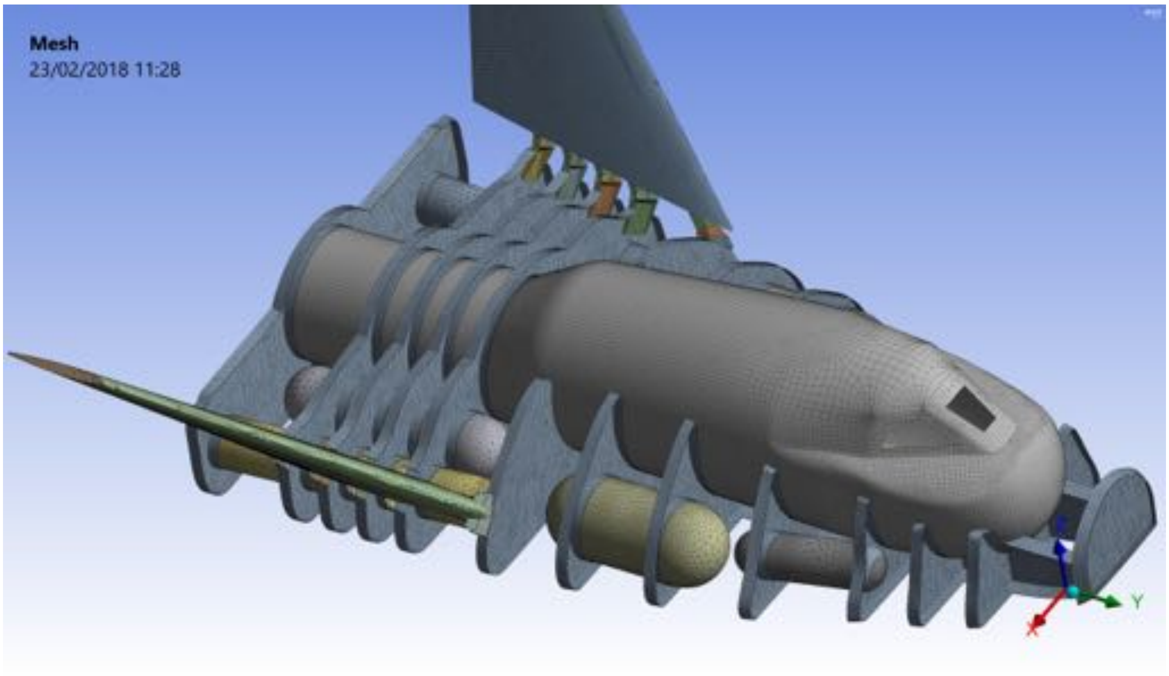
Mesh
23/02/2018 11:28
Z
Y
X

Figure 6.1: Final mesh for our Dream Chaser concept (fuselage skin is not showed).

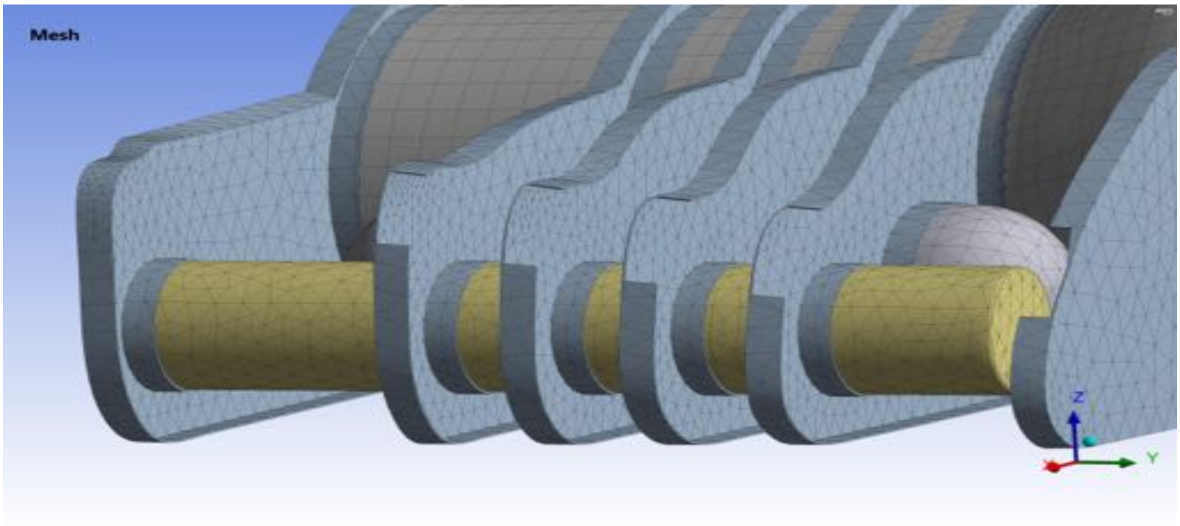

Figure 6.2: *Abort 8g - global.*

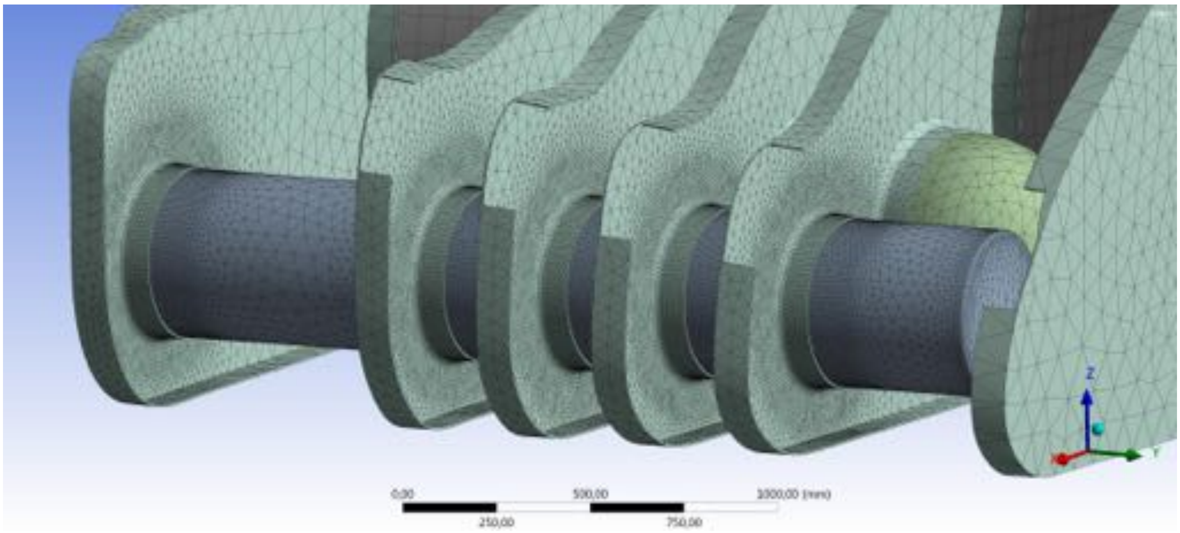
Z
0,00
500,00
1000,00 (mm)
250,00
750,00

Figure 6.3: *Abort 8g - local.*

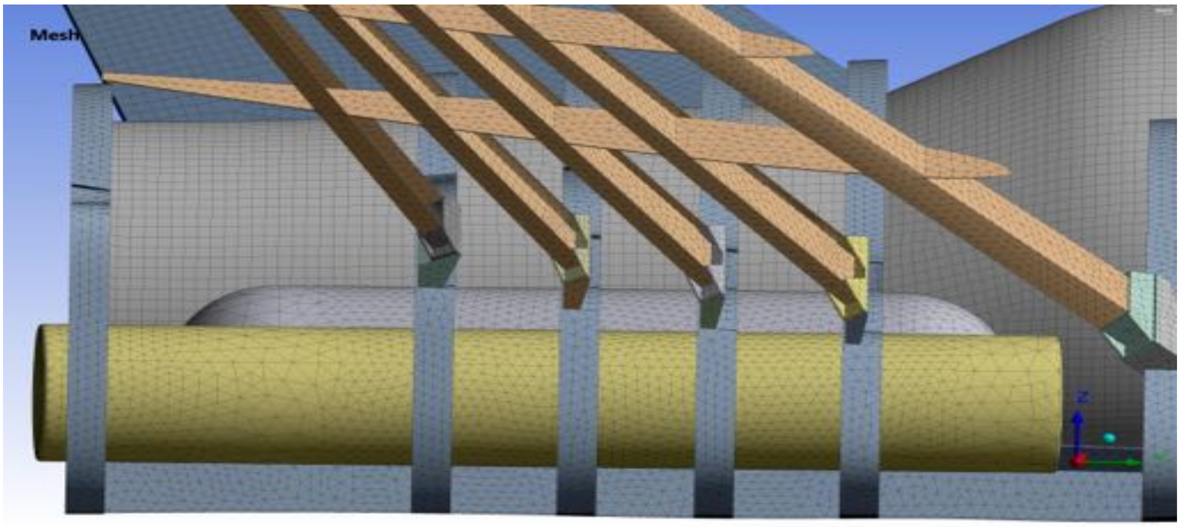

Figure 6.4: *Pullup 2,5g - global.*

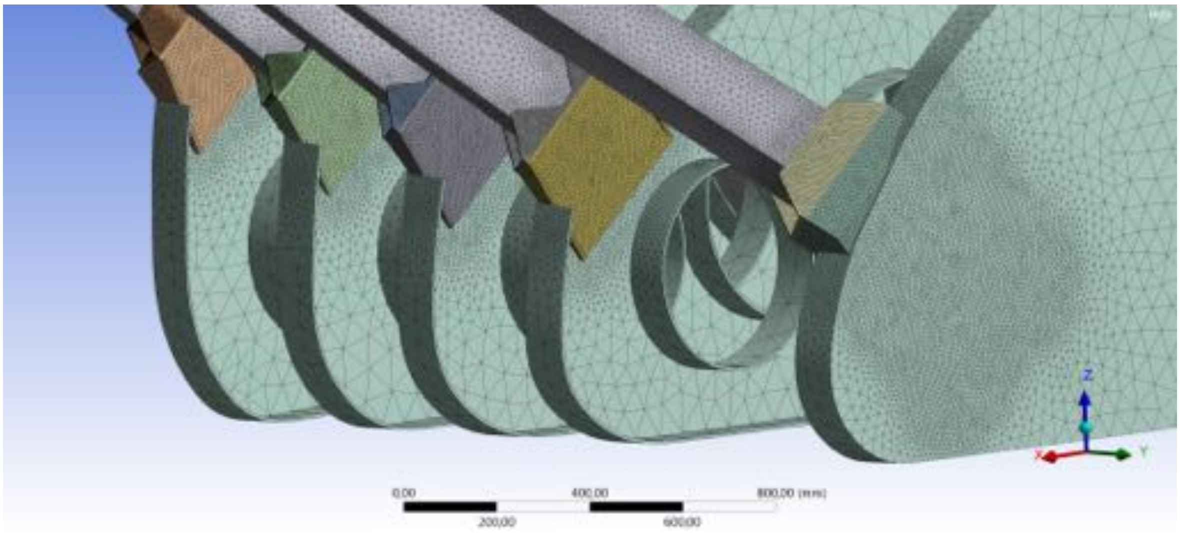

Figure 6.5: *Pullup 2,5g - local.*

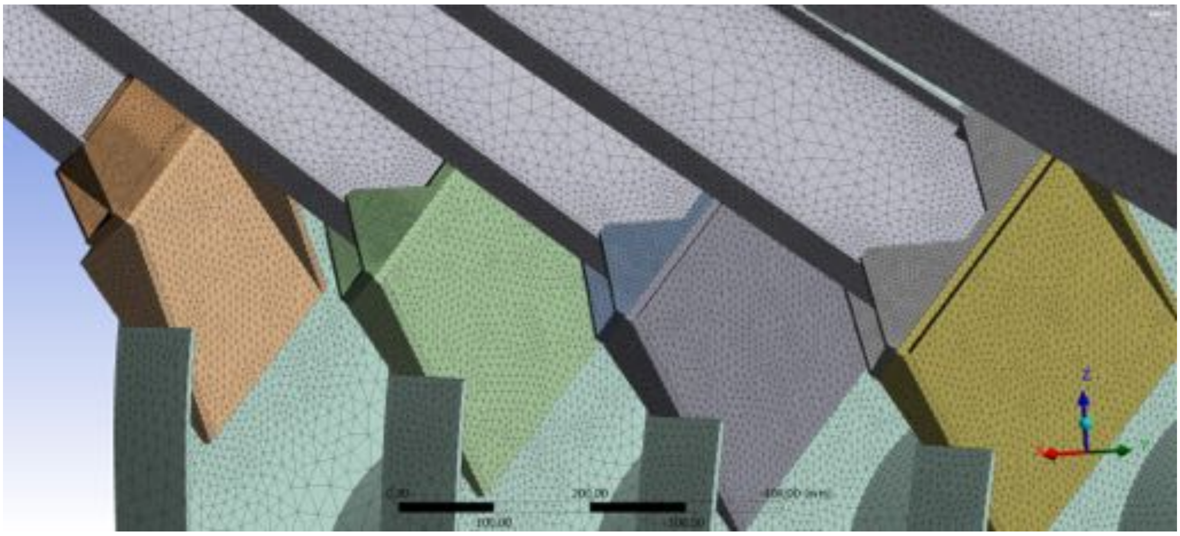

Figure 6.6: *Pullup 2,5g - local (fin root fittings detail).*

6.2 Abort 8g

Global Model

Meshing techniques and general preparation steps used during FEM were given as inputs to set both Abort 8g and Pullup $2,5$g maneuver global analyses, namely our design loading conditions. Initial simulations were performed all with 7 mm surfaces thickness.

Concerning global abort analysis settings, the vehicle was clamped at the rear edges of the pressurised module and aft rib (n°13) to simulate initial instant ($t=0^+$) in which the propulsion system generates a huge thrust of 706.320 N to propel the spacecraft far away from the launcher, placing it in an escape/emergency maneuver. Such level of force was assumed to evenly act on the outer boundaries of main tanks, simulating the force imparted to the spacecraft. Essentially, this physical condition represents a case in which all the nominal thrust is

applied impulsively at once (which of course does not happen in reality), but it is a conservative way to assess structural response upon loading application.
Inertial effects were assessed by setting standard earth gravity acceleration value, acting longitudinally against the thrust direction. Stresses and deformations are shown in Fig.6.8 and 6.9:

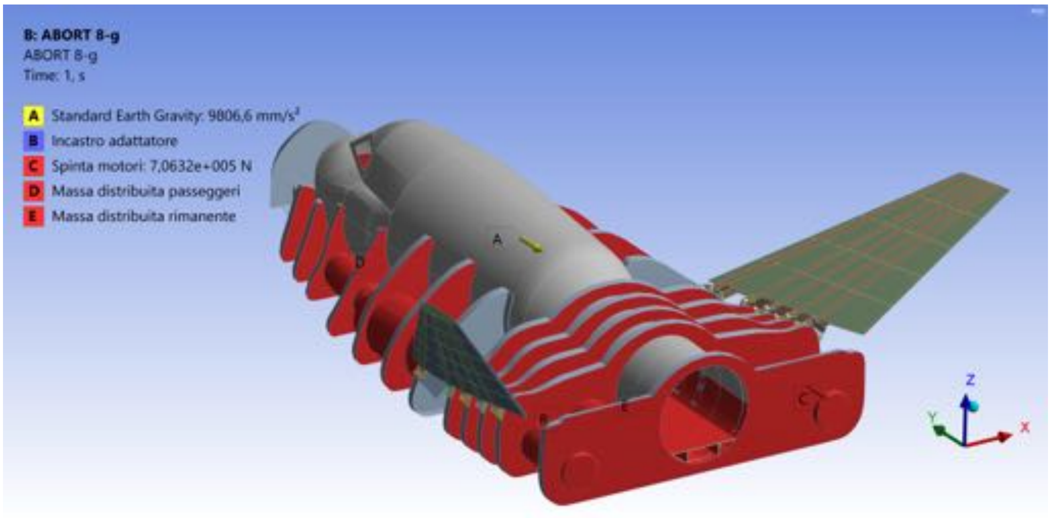
B: ABORT 8-g
ABORT 8-g
Time: 1, s
A Standard Earth Gravity: 9806,6 mm/s²
B Incastro adattatore
C Spinta motori: 7,0632e+005 N
D Massa distribuita passeggeri
E Massa distribuita rimanente
A
Z
Y
X

Figure 6.7: Abort 8g global model - analysis setup (constraints + loads).

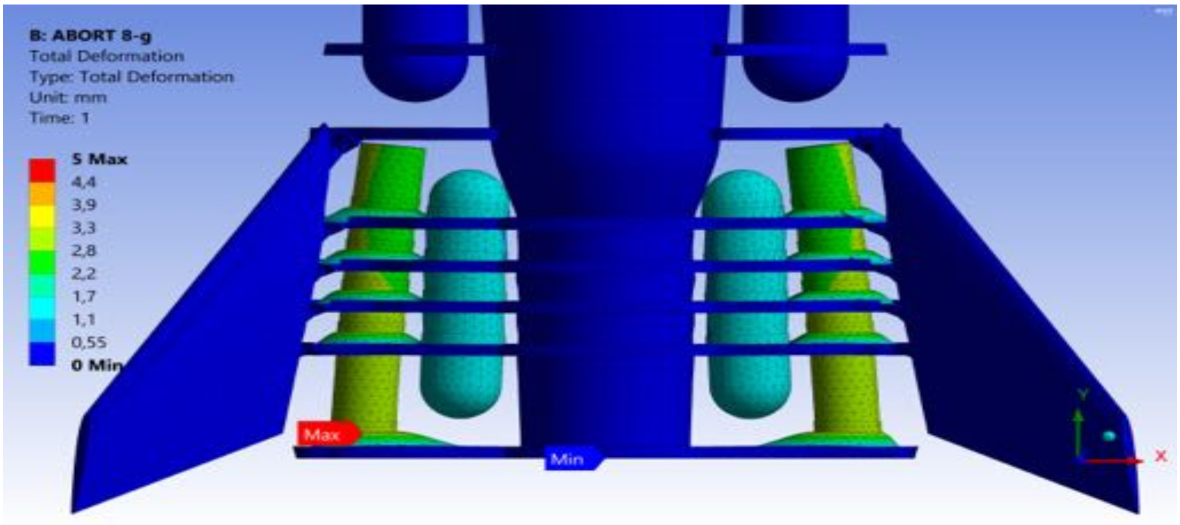
B: ABORT 8-g
Total Deformation
Type: Total Deformation
Unit: mm
Time: 1
5 Max
4,4
3,9
3,3
2,8
2,2
1,7
1,1
0,55
0 Min
Max
Min
Y
X

Figure 6.8: Abort 8g global model - deformation patterns. Maximum deflection corresponds to a 5 mm fuselage skin deformation near the thrust point of application. This is due to load transfer from tanks to skin through rib deformation.

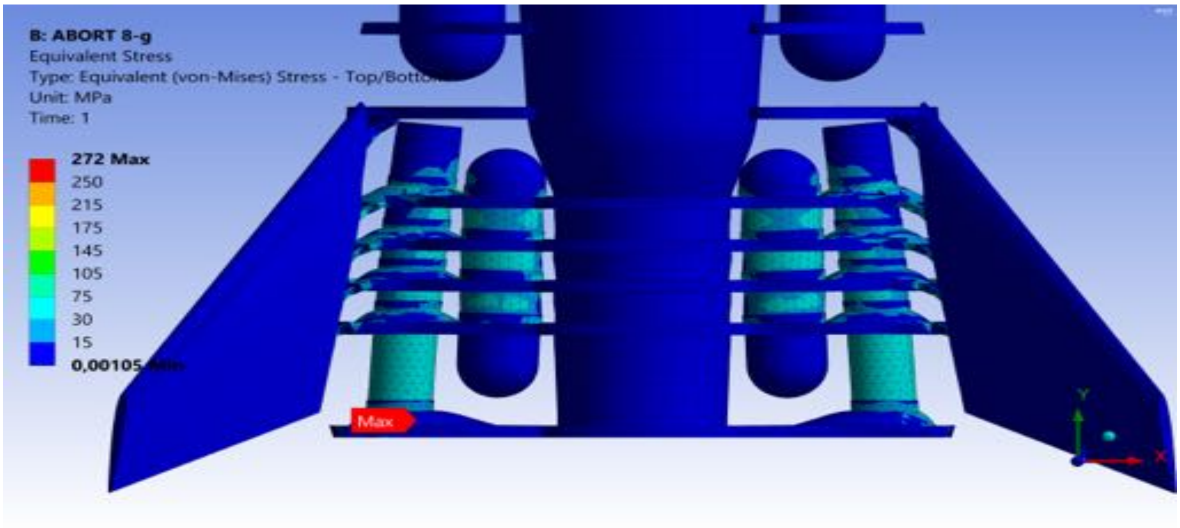

Figure 6.9: Abort 8g global model - equivalent stress patterns. Maximum stress is 272 MPa inside the tanks.

Local Model

The detailed analysis of the abort scenario confirms the large deformation of fuselage ribs found in the global simulation. In the previous simulation, values for the displacements of fuselage ribs are of the same value of rib thickness. This implies that besides the assumed plate behaviour for each rib, membrane effects start to play a role.

The first analysis, the one with 7 mm, shows a peak deformation of 7, 5 mm on each rib around the hole area where the tank is attached. The latter deflects in a rigid way, with a displacement equal to the peak one as can be viewed from the following figures. Displacements distribution is sorted in concentric band around the hole and decreases by moving away from it. Main stressed regions are those around holes and along rib edges as can be viewed from Fig.6.11 , with a value of about 290 MPa, but the rest of the element is subjected to lower values of approximately 50 MPa. Maximum stress occurs on the rib n°9, in the region between the two holes, due to stress concentration effects, which result in mutual influence between the two stress fields.

This solution is just as starting point for an iterative improvement process that guided us towards a better comprehension of internal structure, that is the topic of next chapter.

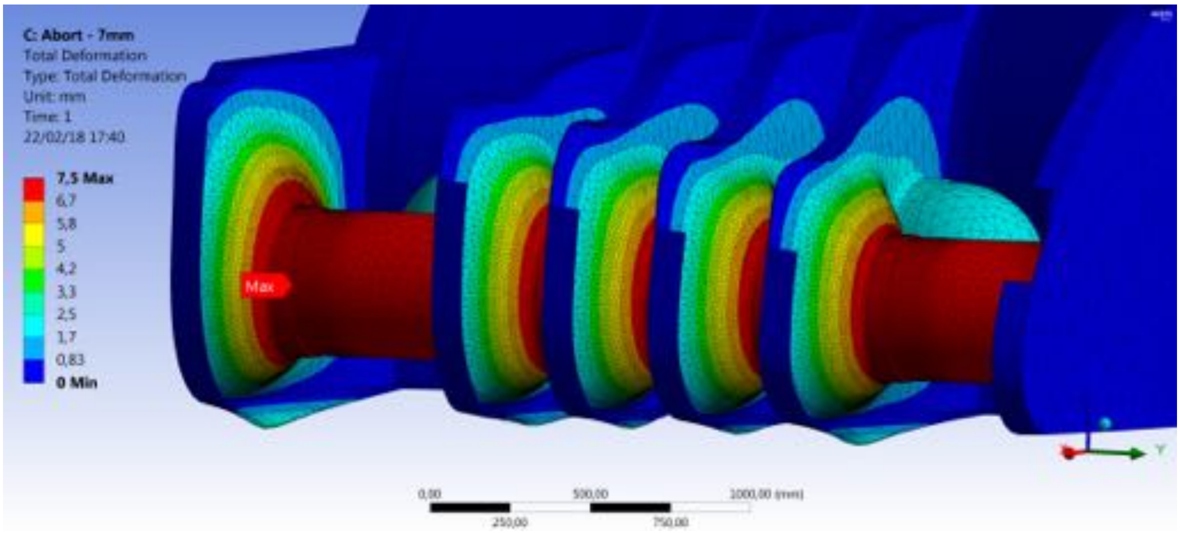
C: Abort - 7mm
Total Deformation
Type: Total Deformation
Unit: mm
Time: 1
22/02/18 17:40
7,5 Max
6,7
5,8
5
4,2
3,3
2,5
1,7
0,83
0 Min
Max
Y
0,00
500,00
1000,00 (mm)
250,00
750,00

Figure 6.10: Abort 8g local model - deformation patterns.

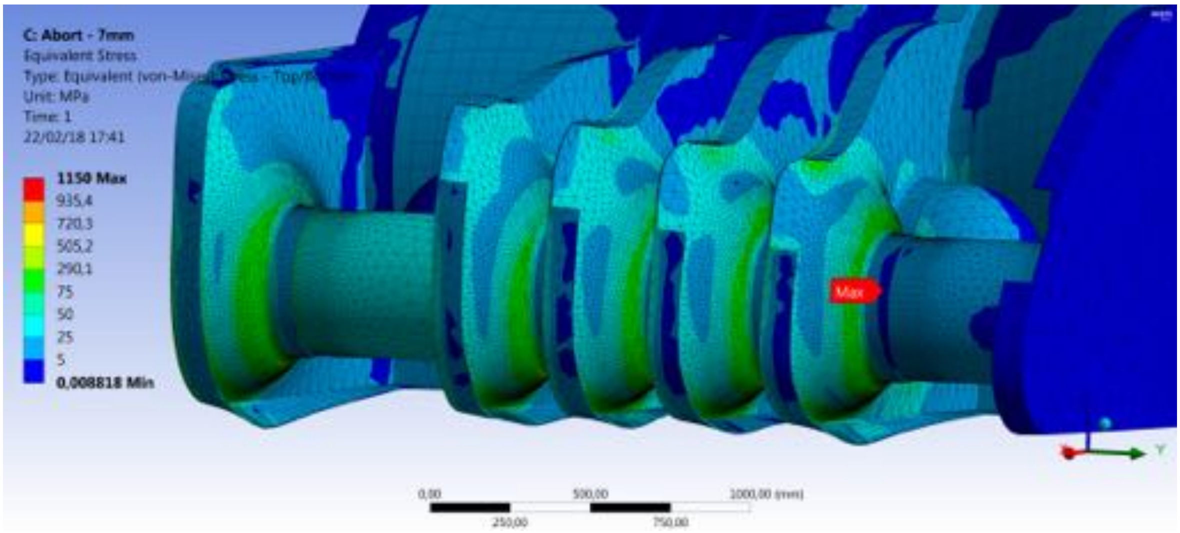
C: Abort - 7mm
Equivalent Stress
Type: Equivalent (von-Mises) Stress - Top/Bottom
Unit: MPa
Time: 1
22/02/18 17:41
1150 Max
935,4
720,3
505,2
290,1
75
50
25
5
0,008818 Min
Max
Y
0,00
500,00
1000,00 (mm)
250,00
750,00

Figure 6.11: Abort 8g local model - equivalent stress patterns.

6.3 Pullup 2,5g

Global Model

The aerodynamic pullup maneuver performed by Dream Chaser during subsonic reentry phase was analysed with the aid of Ansys *Inertia Relief* solver control. In this way, we let it solve the equations of statics 3.1 and 3.2 to compute the free-body equilibrium under inertial and external applied loads. The reference point was assigned close to the spacecraft centre of gravity (CG) through the command of *Remote Displacement*, once being connected to a couple of symmetrical points of the surrounding structure (the CG coordinates were known thanks to Ansys solution information sheet).
For what concerns aerodynamic loads, as already stated in Sec.2.2, 50% of total lift (which is of 220.725 N) was applied to the canted fins skin in yaw direction, while the other 50% acting on the fuselage skin. On this regard, we have to remark that we tried to recreate a fictitious load pattern in order to simulate the real distribution, which has to provide a pitching moment of the vehicle about its aerodynamic centre. For this reason, we subdivided this 50% in three regions: 20% on the skin bottom, and the other 80% on the top part (40% around the nose and 60% on all the skin left area, respectively). Consequently, we also assessed the downforce exerted by control surfaces (which we did not model) to supply equilibrium by perfectly balancing the rate of rotation around the pitch axis. In the end, drag effects were also simulated by setting an estimated value of 20% the total lift ($D = 44.145$ N), as already mentioned in Sec.4.3.

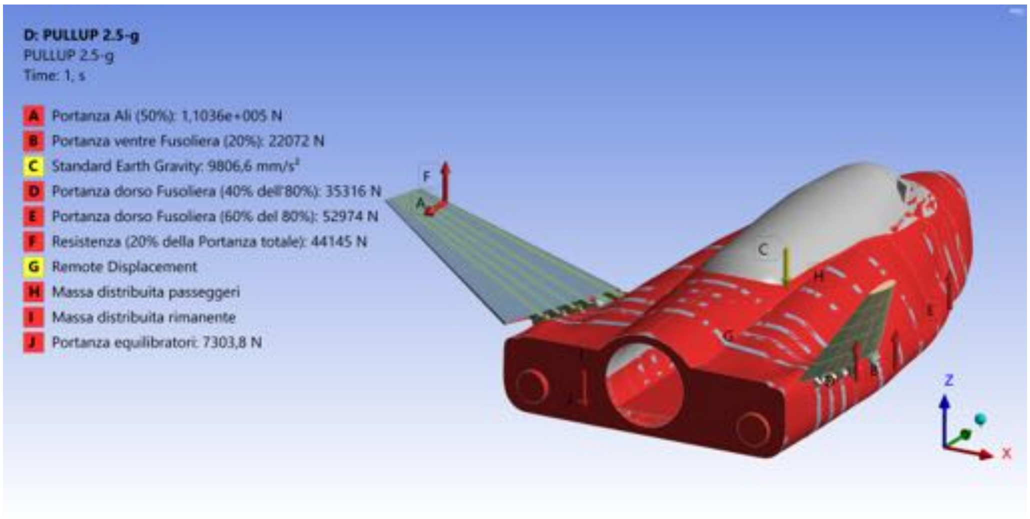
D: PULLUP 2.5-g
PULLUP 2.5-g
Time: 1, s

- A Portanza Ali (50%): 1,1036e+005 N
- B Portanza ventre Fusoliera (20%): 22072 N
- C Standard Earth Gravity: 9806,6 mm/s²
- D Portanza dorso Fusoliera (40% dell'80%): 35316 N
- E Portanza dorso Fusoliera (60% del 80%): 52974 N
- F Resistenza (20% della Portanza totale): 44145 N
- G Remote Displacement
- H Massa distribuita passeggeri
- I Massa distribuita rimanente
- J Portanza equilibratori: 7303,8 N

Figure 6.12: Pullup 2,5g global model - analysis setup (constraints + loads).

The following pictures present the stress and deformation fields for this loading condition.

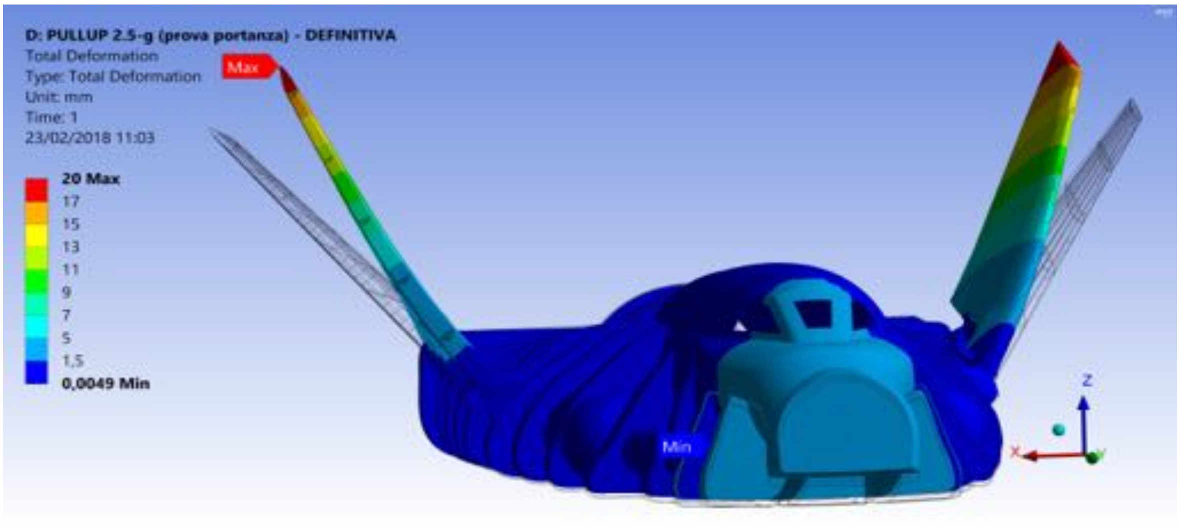
D: PULLUP 2.5-g (prova portanza) - DEFINITIVA
Total Deformation
Type: Total Deformation
Unit: mm
Time: 1
23/02/2018 11:03
20 Max
17
15
13
11
9
7
5
1,5
0,0049 Min
Max
Min
Z
X
Y

Figure 6.13: Pullup 2,5g global model - deformation patterns. Max displacement occurs at fins tip, as expected. The figure shows both deformed and undeformed structure shapes to better understand the overall deflections.

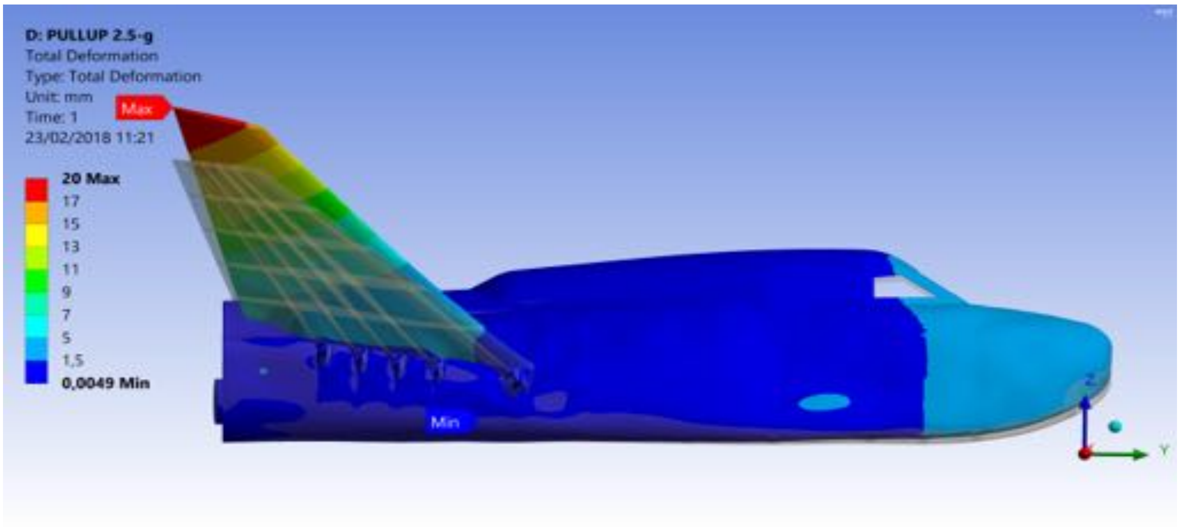
D: PULLUP 2.5-g
Total Deformation
Type: Total Deformation
Unit: mm
Time: 1
23/02/2018 11:21
20 Max
17
15
13
11
9
7
5
1,5
0,0049 Min
Max
Min
Z
Y

Figure 6.14: Pullup 2,5g global model - deformation patterns (lateral view).

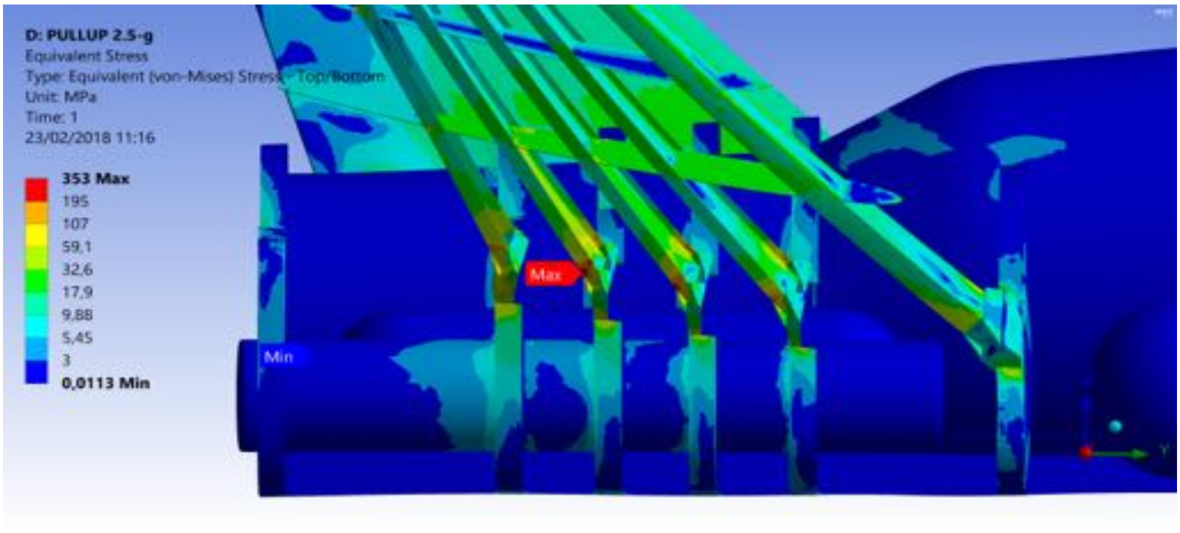

Figure 6.15: Pullup 2,5g global model - equivalent stress patterns. As expected, again, both fins and fuselage try to strain similarly to a cantilever beam, meaning that bending is the primary cause of deformation critically affecting the structure strength, particularly at the root fittings, where maximum stress of 353 MPa occurs.

Local Model: Fin Joints Analysis

After the simulation of the pullup scenario for the entire spacecraft, a local analysis around fin root fittings was performed, in order to compare the results with design procedure explained in Sec.5.2.4. This analysis comprises a symmetric portion of the vehicle around the rear side where the fin is linked to the aft ribs. Part of the main body frame is included in the analysis to take into account the load transfer from the fin structure to the ribs and keel beams. Loading condition is slightly different from the global simulation: lift and drag are the same as before, but there is no aerodynamic load applied on the considered part of the fuselage skin. The boundary conditions are applied on the plane of symmetry and must satisfy the compatibility of displacements at this location. Simple supports are applied on rib sections lying on that plane, and a fixed support is applied on the lower section of rib n°9 to provide the same constraint, recalling the concepts of classic theory treated during the previous course of Aerospace Structures. The results of deformation are shown in Fig.6.16. As expected, the maximum deformation occurs at fin tip section, proving the idealised structural beam analytical model. The value is a bit higher than in the global analysis due to a much thicker and accurate mesh. The rest of the structure remains undeformed confirming that it could be impose a rigid constraint on fin root fittings.

From a first look on the solution of stress distribution, the model clearly shows that stresses are transferred on fuselage ribs, but the fuselage skin is loaded too, even if with lower intensity. In particular, the skin area around the cutouts and along the joints of fuselage skin and ribs are stressed. Stresses on fin spars near the root section and induced stress on the corresponding root fitting are more intense around each spar cap. This condition represents the symmetric stresses encountered on booms in the analytical model. However, the main difference between the two predicted stress distributions is that the analytical model considers the stress caused by bending acting along each boom, thus modeling the spar caps, while the stress resulting from the simulation represents the Von-Mises equivalent stress, therefore the comparison is not straightforward. Nevertheless, the analytical model catches some of the stress value, in particular for spar 3 and 4 on the lower caps, where values are around 220-250 MPa as predicted by the model.

Loads are then transferred to fuselage ribs, which are most stressed near junction plates, holes and around the upper corner linked to the other symmetric part of each rib. Stresses on root fittings are below the allowable limit for Al 7075 but there are some spots where stress concentration occurs: these are around 400 MPa with the maximum at 750 MPa as seen in Fig.s 6.18, 6.19 and 6.21. This outcome is one of the main issue that led us to reconsider the geometry of fin root fitting, as explained in details in Sec.7.3.2.

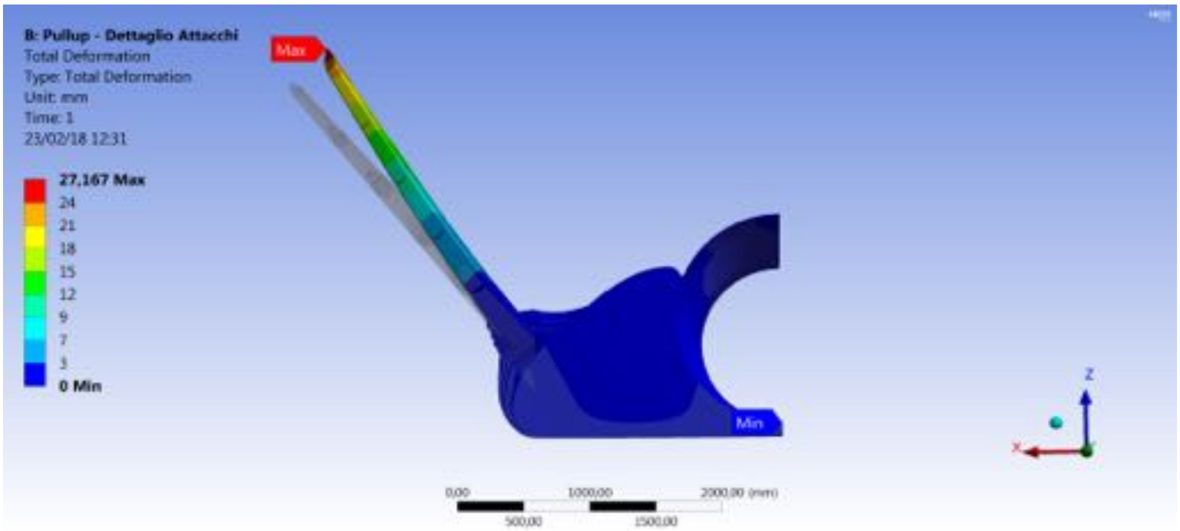
B: Pullup - Dettaglio Attacchi
Total Deformation
Type: Total Deformation
Unit: mm
Time: 1
23/02/18 12:31
27,167 Max
24
21
18
15
12
9
7
3
0 Min
Max
Min
Z
X
0,00
1000,00
2000,00 (mm)
500,00
1500,00

Figure 6.16: Pullup 2,5g local model - deformation patterns.

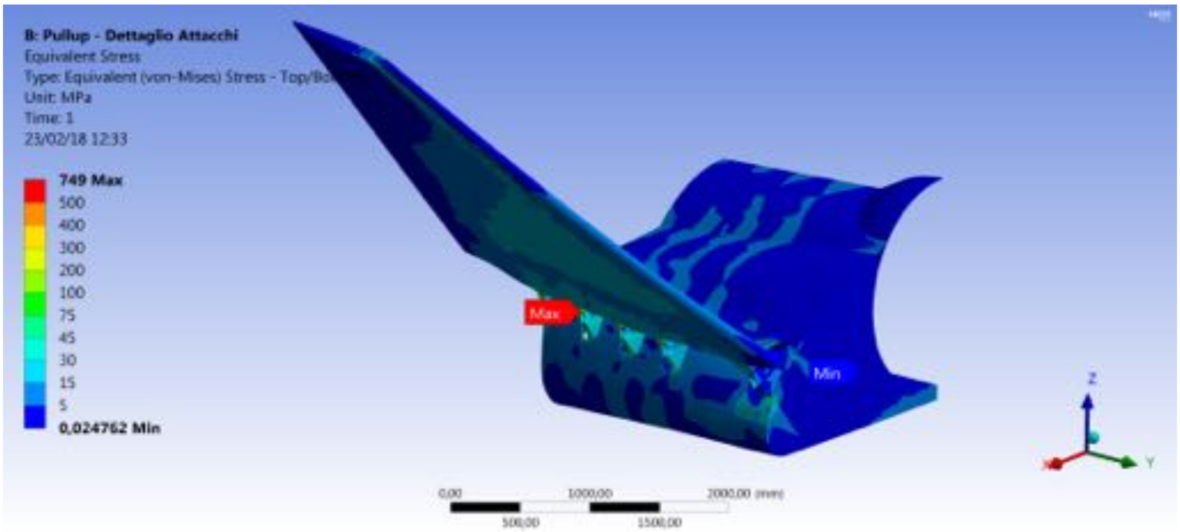
B: Pullup - Dettaglio Attacchi
Equivalent Stress
Type: Equivalent (von-Mises) Stress - Top/Bo
Unit: MPa
Time: 1
23/02/18 12:33
749 Max
500
400
300
200
100
75
45
30
15
5
0,024762 Min
Max
Min
Z
Y
0,00
1000,00
2000,00 (mm)
500,00
1500,00

Figure 6.17: Pullup 2,5g local model - equivalent stress patterns.

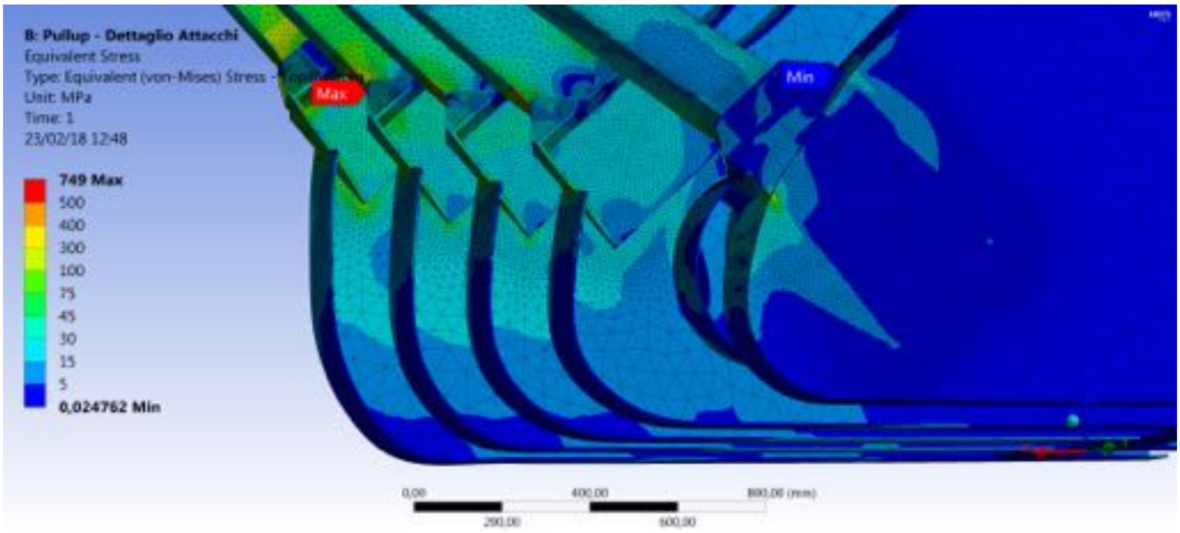
B: Pullup - Dettaglio Attacchi
Equivalent Stress
Type: Equivalent (von-Mises) Stress - Top/Bottom
Unit: MPa
Time: 1
23/02/18 12:48
749 Max
500
400
300
100
75
45
30
15
5
0,024762 Min
Max
Min
0,00
400,00
800,00 (mm)
200,00
600,00

Figure 6.18: Pullup 2,5g local model - equivalent stress patterns (fittings detail).

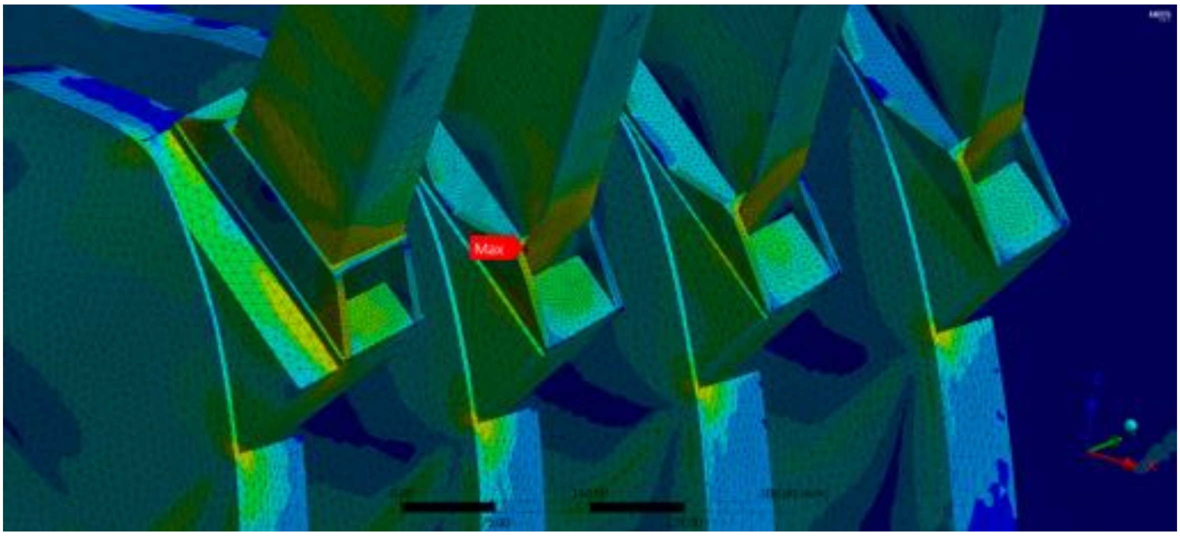

Figure 6.19: Pullup 2,5g local model - equivalent stress patterns (spars caps detail).

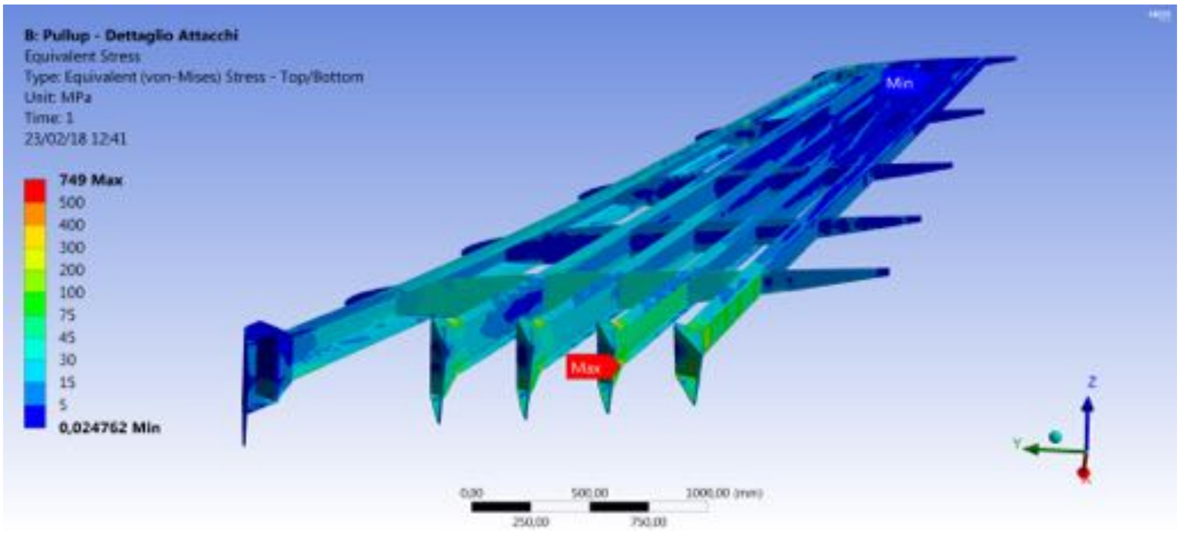
B: Pullup - Dettaglio Attacchi
Equivalent Stress
Type: Equivalent (von-Mises) Stress - Top/Bottom
Unit: MPa
Time: 1
23/02/18 12:41
749 Max
500
400
300
200
100
75
45
30
15
5
0,024762 Min
Min
Max
0,00
500,00
1000,00 (mm)
250,00
750,00
Z
Y

Figure 6.20: Pullup 2,5g local model - fin equivalent stress field.

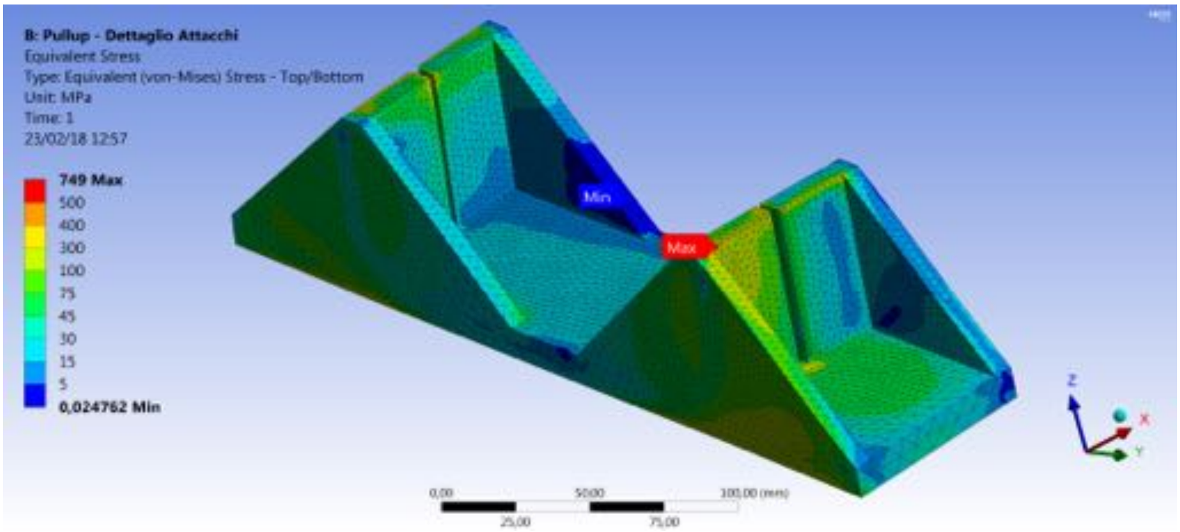
B: Pullup - Dettaglio Attacchi
Equivalent Stress
Type: Equivalent (von-Mises) Stress - Top/Bottom
Unit: MPa
Time: 1
23/02/18 12:57
749 Max
500
400
300
100
75
45
30
15
5
0,024762 Min
Min
Max
0,00
50,00
100,00 (mm)
25,00
75,00
Z
X
Y

Figure 6.21: Pullup 2,5g local model - fin root fitting equivalent stress distribution.

6.4 Modal Analysis

Even if this project has regarded the static analysis of the Dream Chaser primary structure, we decided to carry out a modal analysis. This has been performed on the two main parts of the Dream Chaser studied in this project, the main body structure and the outward fins. Fin is analysed as a canted beam without the wing root fittings while the main body is analysed without fins and relative root fittings and without internal components like tanks and engine structure and in a condition that represents the launch phase. The modal analysis was carried out in Ansys within the *Modal Analysis* environment. The pre-processing of the software consists in the definition of:

- Mass and materials of each member in order for the software to evaluate mass and stiffness matrices
- Boundary conditions

- Number of modes to evaluate

Mass and materials have been already defined during static analyses and are transferred into *Modal Analysis* environment through the data transfer interface in Workbench™. The boundary condition for the analysis of the fin is a fixed support on each spar root section. Based on reference [2], Dream Chaser is mounted on top of a rocket through the aft rib fixed onto a customized adapter. The chosen boundary condition is a fixed support on the aft rib outer edge. The number of modes was set to six both for fin and main body analyses. Table 6.2 and 6.3 list the output of each analysis in terms of natural frequencies and mode shapes.

Natural frequency (Hz)	**Mode Shape**
30.54	beam-type bending, all body
52.79	beam-type lateral bending, all body
71.6	plate mode, lower aft skin
72.23	plate mode, antisymmetric, lower skin, aft part
86.79	plate mode
97.2	plate mode, antisymmetric, lower skin, central part

Table 6.2: Modal analysis results for main body

Natural frequency (Hz)	**Mode Shape**
38.9	beam-type bending
120.32	plate mode
139	combined bending-torsional mode
142.69	plate mode
170.31	beam-type lateral bending
178.21	combined bending-torsional mode

Table 6.3: Modal analysis results for fin.

Mode 2 of the fin is not reported because corresponds to a penetration of the two side of skin around trailing edge due to a lack of the root rib, this can be appreciated also from 6.23.

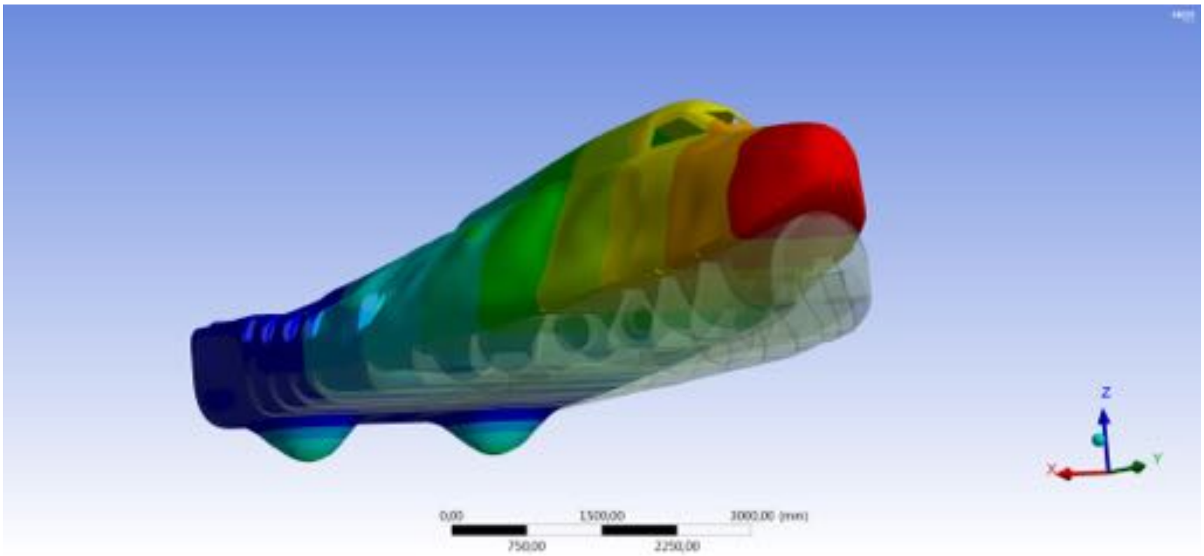
0,00
1500,00
3000,00 (mm)
750,00
2250,00
Z
Y
X

(a) Main body mode 1: bending.

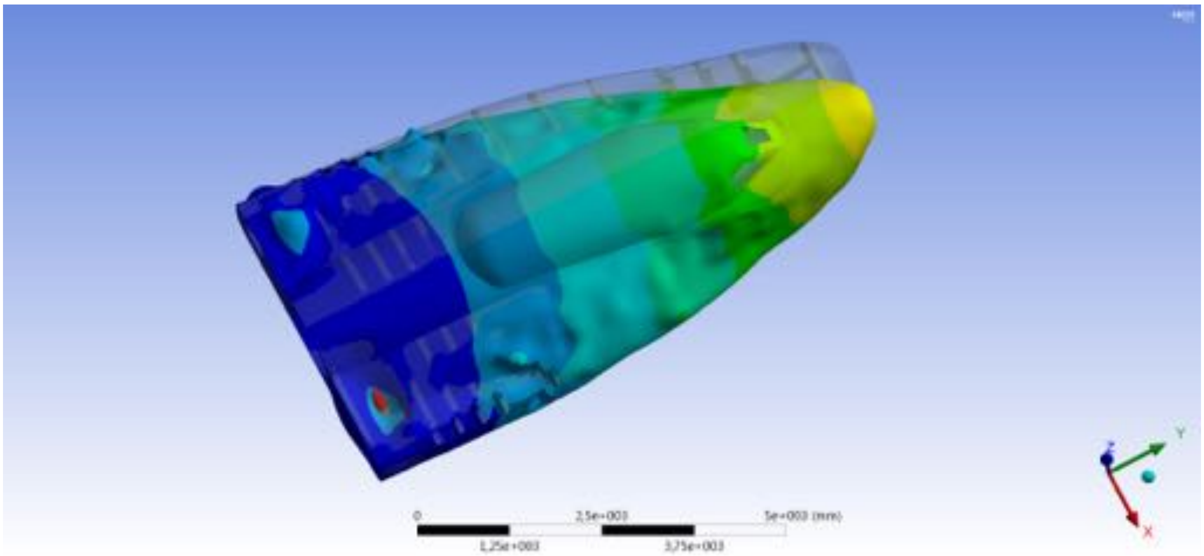
0
2,5e+003
5e+003 (mm)
1,25e+003
3,75e+003
Z
Y
X

(b) Main body mode 2: lateral bending.

Figure 6.22: Main mode shapes of main body.

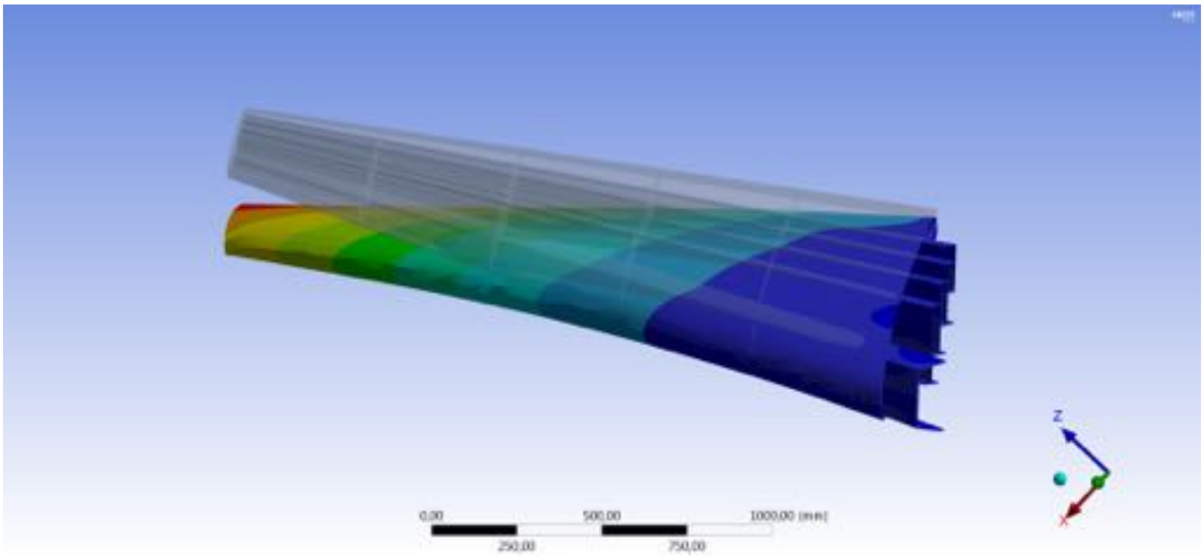
0,00
500,00
1000,00 (mm)
250,00
750,00
Z
X

(a) Fin mode 1: bending.

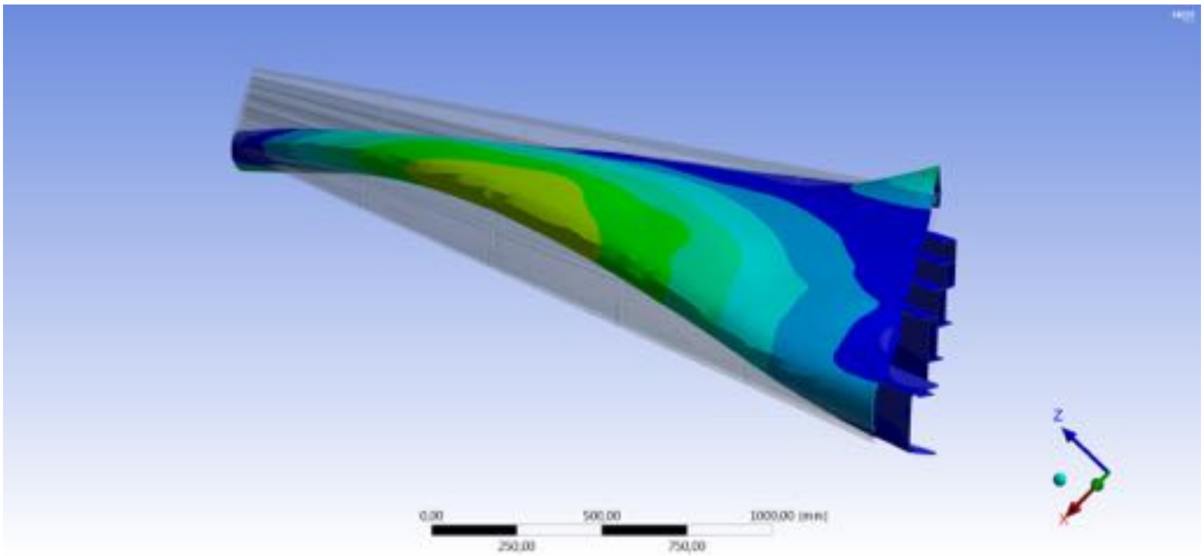
0,00
500,00
1000,00 (mm)
250,00
750,00
Z
X

(b) Fin mode 3: flexural-torsional.

Figure 6.23: Main mode shapes of fin.

Chapter 7

Finite Element Analysis: Optimisation Process

7.1 Pressurised Module

Pressurised Module was our first CAD modeled structural member, so our first element to be simulated accordingly to our project approach. Geometry was imported and opened within Ansys *DesignModeler* environment. There, materials were assigned, as well as, surface thicknesses, which is an input Ansys cannot supply on its own. To do this, we had to firstly set a value and then assess through simulation the allowable material strength, so as to have an idea at least of the order of magnitude we were dealing with.

From pictures and videos, we observed Dream Chaser fuselage ribs flanges were ∼ 10 cm wide, so we decided to start modeling ribs with 7 mm in thickness. Consequently, we assigned this value also to our 3D woven composite crew compartment, in order to uniform surfaces thicknesses. Then it was symmetrically constrained (Ansys provides the relative command) with an internal evenly distributed pressure of 1 atm. Later, further sizing loops followed up in order to get an acceptable material stress level. The results are shown in the following table and figures:

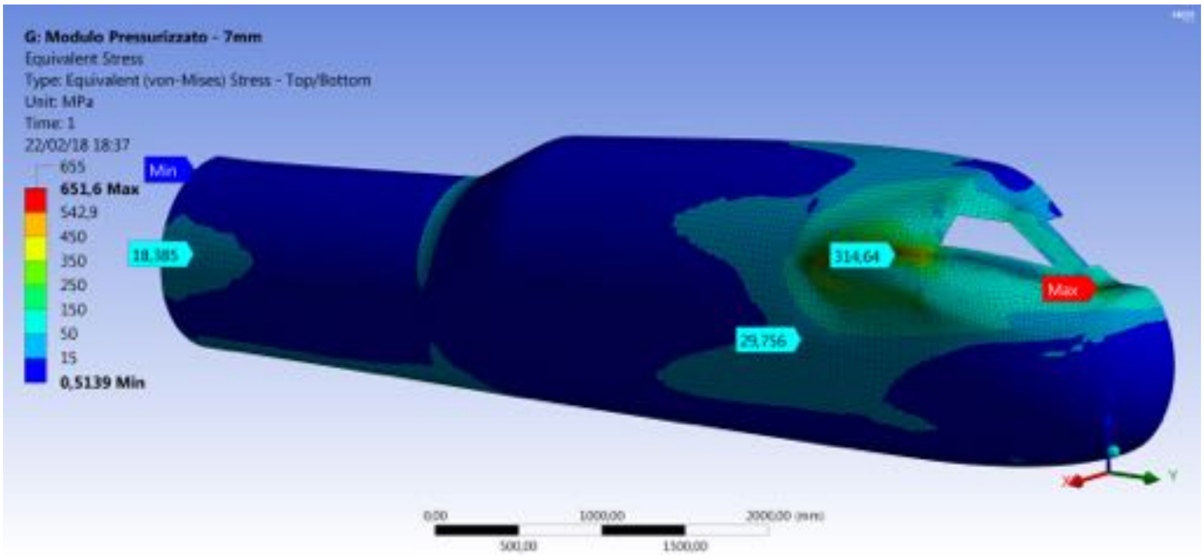

G: Modulo Pressurizzato - 7mm
Equivalent Stress
Type: Equivalent (von-Mises) Stress - Top/Bottom
Unit: MPa
Time: 1
22/02/18 18:37

Figure 7.1: Step 1, 7 mm.

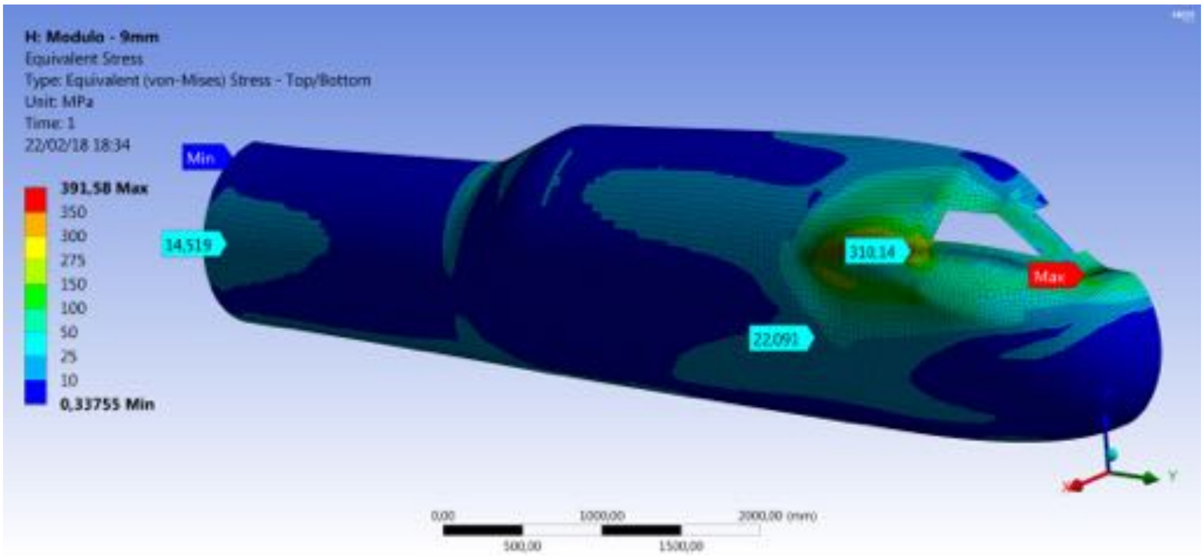
H: Modulo - 9mm
Equivalent Stress
Type: Equivalent (von-Mises) Stress - Top/Bottom
Unit: MPa
Time: 1
22/02/18 18:34
391,58 Max
350
300
275
150
100
50
25
10
0,33755 Min
Min
14,519
310,14
Max
22,091
Y
0,00
1000,00
2000,00 (mm)
500,00
1500,00

Figure 7.2: Step 2, 9 mm.

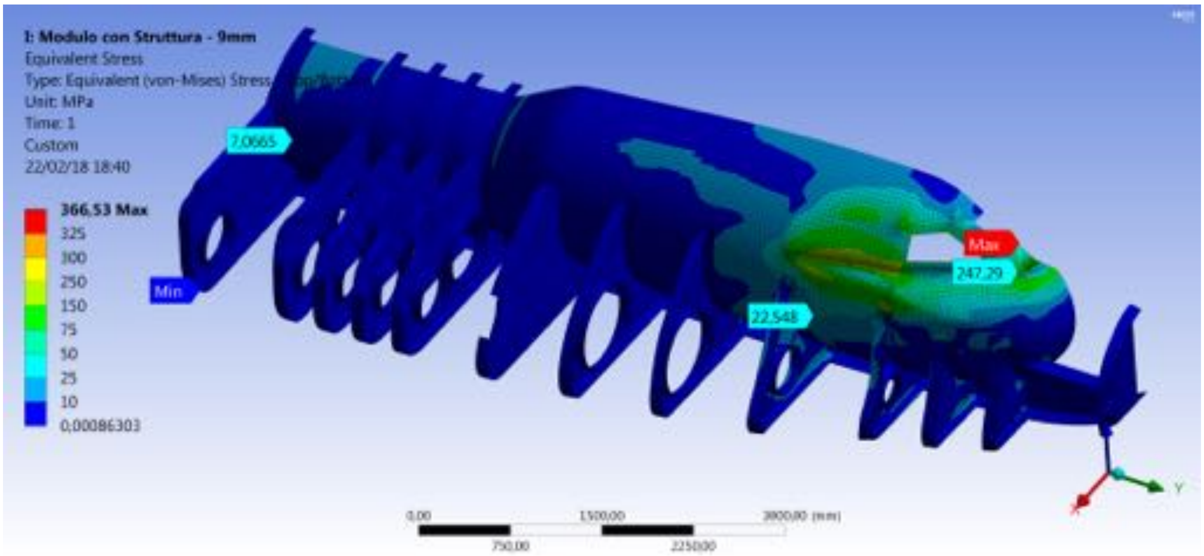
I: Modulo con Struttura - 9mm
Equivalent Stress
Type: Equivalent (von-Mises) Stress
Unit: MPa
Time: 1
Custom
22/02/18 18:40
366,53 Max
325
300
250
150
75
50
25
10
0,00086303
7,0665
Min
22,548
Max
247,29
Y
0,00
1500,00
3000,00 (mm)
750,00
2250,00

Figure 7.3: Step 3, 9 mm plus ribs and keel beam.

In general, stresses well distribute themselves around the pressurised vessel, but they tend to concentrate at the front portion underneath the cabin windows. This derives from merely geometrical modeling features we could not succeed in refining any better, but we found out a 9 mm thickness could lessen the stress concentration region to a −40% with respect to the initial configuration. Surrounding ribs help in lowering maximum equivalent stress value down to 366 MPa, well below the material ultimate strength. This stress relief was accompanied by an increase in module mass of barely +43 kg (+28% added composite mass), and a reduction of maximum displacement from 34 mm ($\sim$ 5 times the thickness) to 19 mm (−44%), which is about twice the vessel thickness. Of course, this latter value could appear still quite high, but we were aware of the presence of unmodeled internal ring frames that would further stiff the entire module and diminish even more the predicted maximum deflection.

Blue flags at few module locations inside the figures show points where we computed stresses by means of results from theory of thin-walled cylindrical pressure vessels (see section 6.8 of Sarafin's book [15]) to assess the validity of symmetrical constraints applied to our component and the accuracy of our results. Essentially, these turned out to match quite perfectly. At the

	Thickness (mm)	**Mass** (kg)	**Max deflection** (mm)	**Max stress** (MPa)
Step 1	7	152	34	651
Step 2	9	196	19	391
Step 3*	9	196	18	366

Table 7.1: Pressurised Module sizing loops for thickness and allowable strength evaluation. *Step 3 includes the assembly of fuselage ribs and keel beams.

aft end region, for instance, we have:

$$\textit{Hoop stresses,} \qquad \sigma_\theta = \frac{pr}{t} \tag{7.1}$$

$$\textit{Longitudinal stresses,} \qquad \sigma_L = \frac{pr}{2t} \tag{7.2}$$

$$\textit{Total Stresses,} \qquad \sigma_{tot} = \sqrt{\sigma_\theta^2 + \sigma_L^2} = \frac{\sqrt{5}}{2}\frac{pr}{t} \approx 14\text{MPa} \tag{7.3}$$

where $t = 9\text{mm}$, $r = 1,016\text{m}$, and $p = 101.325\text{Pa}$. The above formulations are usually accurate enough if r/t is greater than about 10 (which is the case).

7.2 Abort 8g

Once results were obtained from the simulation at 7mm thickness, the following step was to parametrize the analyses respect to rib thickness, to better understand its influence in the deformation and stress, and to assess the validity of this solution. Discrete values were selected respectively with 7, 9 and 11 mm.

The second local analysis with 9 mm shows a similar pattern as in the previous simulation but with a reduced value of displacements and stresses. Deformation distribution recalls almost the same results, but with a lower peak value around 6 mm where the thrust force is applied.

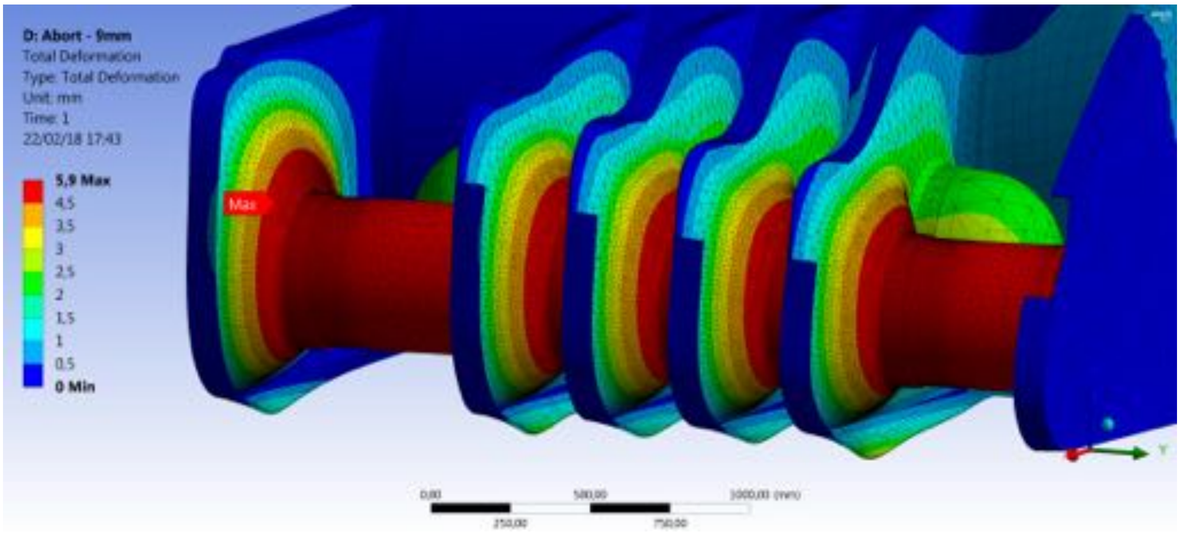

Figure 7.4: Abort 8g local model - deformation patterns for 9 mm thickness.

As before, the results in the figure show uniform displacements for both tanks along the longitudinal direction. This could be explained considering the combined effect of materials

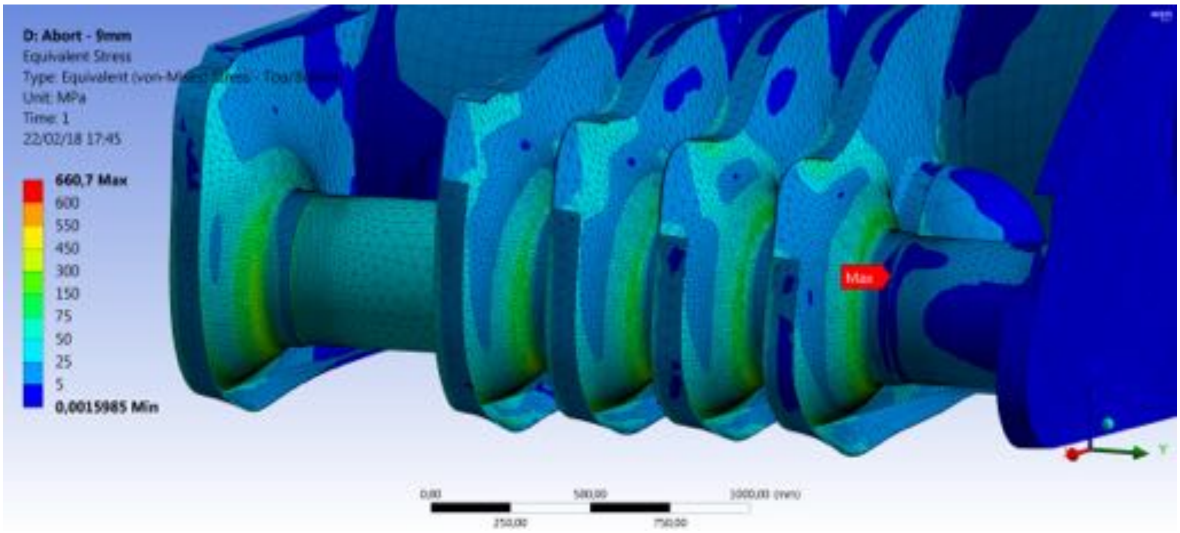
D: Abort - 9mm
Equivalent Stress
Type: Equivalent (von-Mises) Stress - Top/Bottom
Unit: MPa
Time: 1
22/02/18 17:45
660,7 Max
600
550
450
300
150
75
50
25
5
0,0015985 Min
Max
0,00
250,00
500,00
750,00
1000,00 (mm)
Y

Figure 7.5: Abort 8g local model - stress patterns for 9 mm thickness

rigidity and how components are loaded, although for tanks is an acting direct stress, for the rib is a plate loaded out of plane, resulting in this way strains negligible for tanks respect to the ribs. Also the stress field keeps the same distribution but with a smoother gradient. Now in the regions around holes and bordering sides, stresses are in the order of 150 MPa, and all around within a range of 25-50 MPa. Peak stress goes down to 660 MPa (-43%) in the same position as before.

No relevant differences appear with 11 mm simulation. Regarding deformation, the pattern is almost the same, with the maximum displacement about 4 mm ($\approx 0,36$ the thickness). The stress distribution gets more uniform for points with values around 10-30 MPa. Maximum stress arises again, in the same position of previous analyses, but now with a value of 478 MPa, resulting in a reduction of -60% from the first simulation.

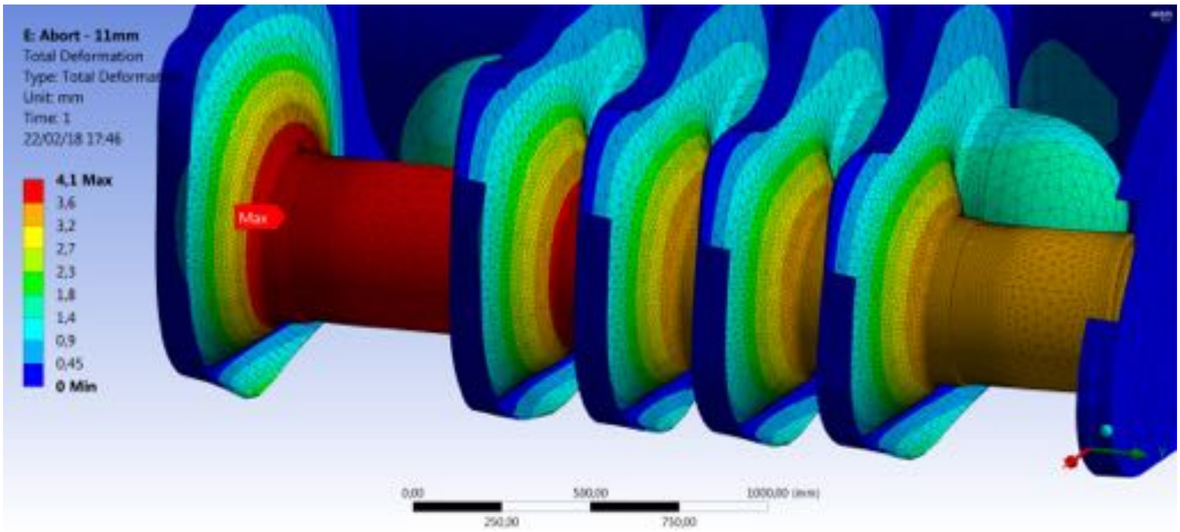
E: Abort - 11mm
Total Deformation
Type: Total Deformation
Unit: mm
Time: 1
22/02/18 17:46
4,1 Max
3,6
3,2
2,7
2,3
1,8
1,4
0,9
0,45
0 Min
Max
0,00
250,00
500,00
750,00
1000,00 (mm)
Y

Figure 7.6: Abort 8g local model - deformation patterns for 11 mm thickness.

At this point of our process, we realized that ribs, still loaded as plate out of plane, were not sufficiently enough to carry all the loads, so we applied rough improvements on the engine support that restrains itself to the vehicle structure. Four diagonal rods are introduced to

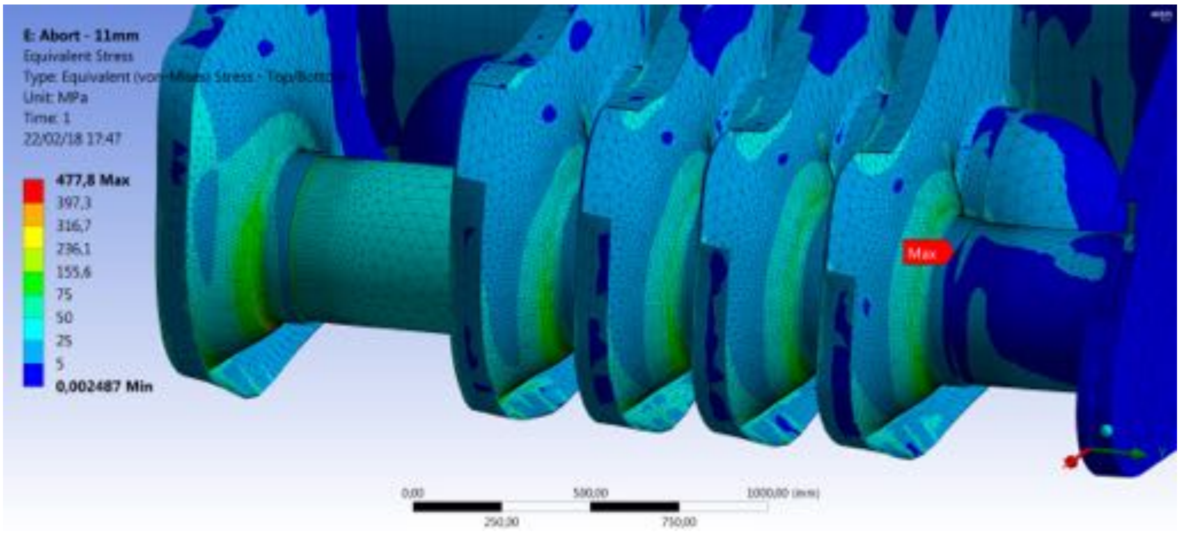

Figure 7.7: Abort 8g local model - stress patterns for 11 mm thickness

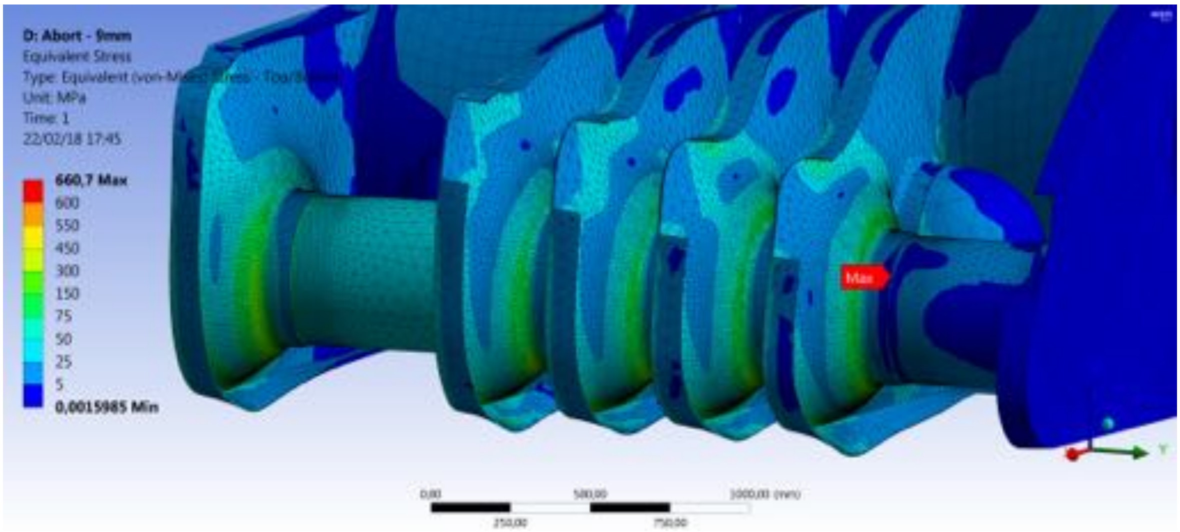

Figure 7.8: Abort 8g local model - detail of stress patterns for 11 mm thickness

mitigate the large displacements resulted in the previous analyses. This attempt was carried out just to see if the idea of an introducing direct-stress-component could solve the matter, so no specific considerations were done on the attachment points or accurate geometry was modeled for the rods.

Thus, they were fixed through two rings on the main tank, and attached to pressurized module and keel beams, respectively for the upper and lower rods. Rib thickness were lowered again to 9 mm since from a mechanical point of view the 11 mm solution did not produce relevant improvements to justify an increase of mass. The results of this attempt is reported distinctly for the main geometry and rods. The deformation field exhibits now net distinction colour pattern, that suggest rods are working, limiting the engine sliding displacement. The maximum one is reduced to 3, 3 mm on the rib n°13, same order of value for rod peak, that is 50% less than equivalent solution without rods.

Comparing to that, also stresses exhibits a general reduction with a uniform distribution, but with the difference that now point of maximum occurs on titanium tank despite in the narrow

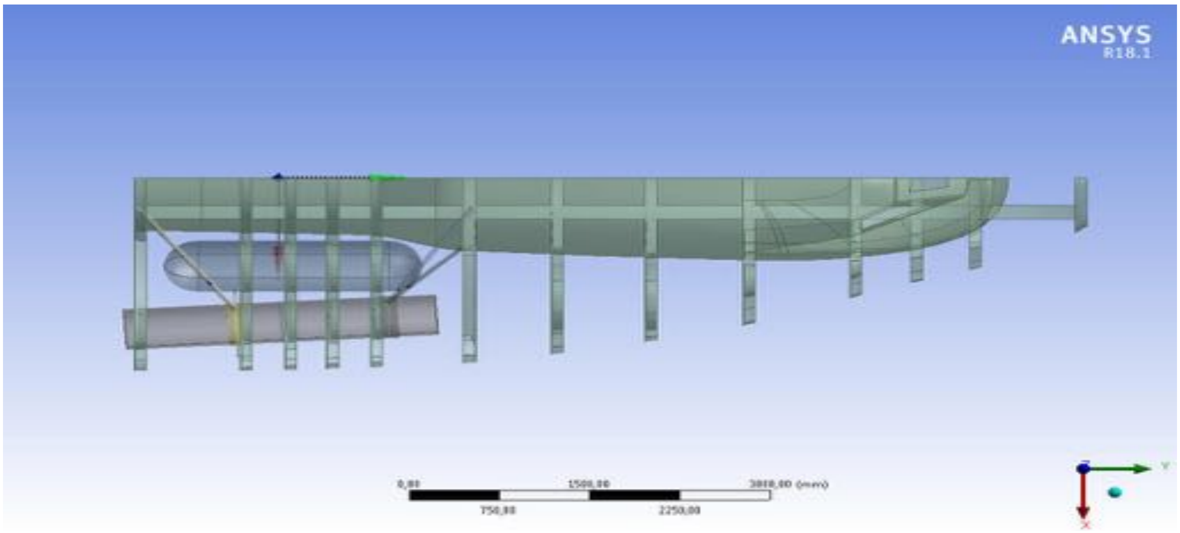
ANSYS
R18.1
0,00
1500,00
3000,00 (mm)
750,00
2250,00
Y
X

Figure 7.9: Abort 8g local model - diagonal rods layout.

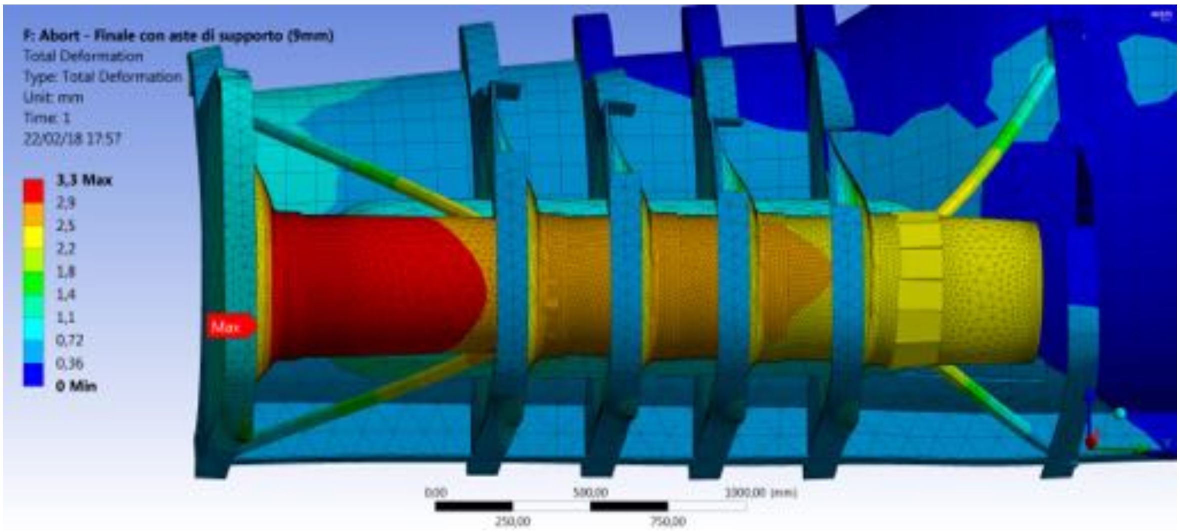
F: Abort - Finale con aste di supporto (9mm)
Total Deformation
Type: Total Deformation
Unit: mm
Time: 1
22/02/18 17:57
3,3 Max
2,9
2,5
2,2
1,8
1,4
1,1
0,72
0,36
0 Min
Max
0,00
500,00
1000,00 (mm)
250,00
750,00

Figure 7.10: Abort 8g local model - deformation patterns with diagonal rods frame.

rib strip. This is due to rod line attaching point, that as previously stated, was roughly modeled as a line beam with an assigned cross section (into the design modeler), generating in this way a point of local singularity. Although this mistake, 510 Mpa occurs instead of 660 Mpa, and now it has to be compared respect to the yield strength of titanium, that is higher than composite 3D-woven, resulting in an increase of global safety factor. Looking at the graph of the booms, it could be noticed that only one rod is mainly loaded (with a uniform stress at 54 MPa) in a tensile way, leaving the front side working in compressive. Still, it is not an acceptable concept, but again, this was just an attempt to move our considerations. All of that trials, in fact, led us to the conceptual idea that ribs has to be relieved by the working function of plates loaded out of plane, and pick up all the load to a supporting truss frame working only under direct stress. In this way external load is guided to the core of entire vehicle, the pressurized module, leaving the ribs carrying only the weight function. All this is explained in the next section.

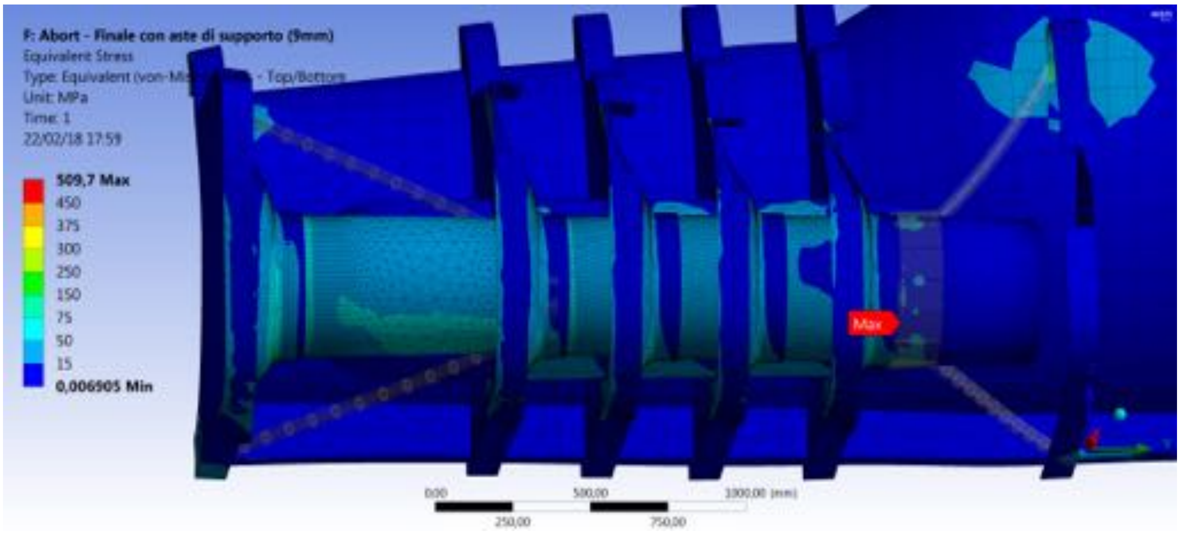
F: Abort - Finale con aste di supporto (9mm)
Equivalent Stress
Type: Equivalent (von-Mi - Top/Bottom
Unit: MPa
Time: 1
22/02/18 17:59
509,7 Max
450
375
300
250
150
75
50
15
0,006905 Min
Max
0,00
500,00
1000,00 (mm)
250,00
750,00

Figure 7.11: Abort 8g local model - equivalent stress patterns with diagonal rods frame.

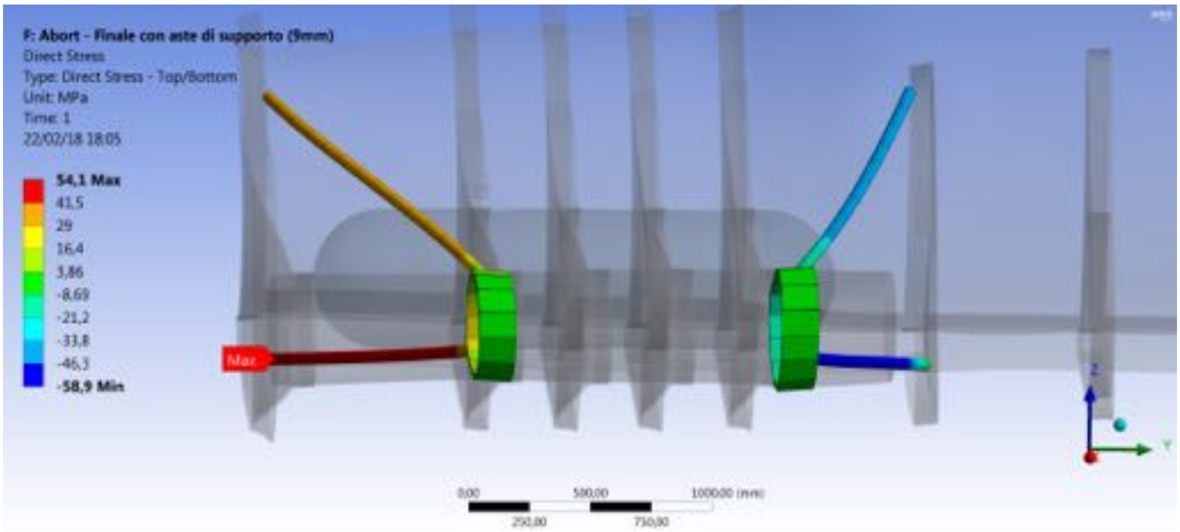
F: Abort - Finale con aste di supporto (9mm)
Direct Stress
Type: Direct Stress - Top/Bottom
Unit: MPa
Time: 1
22/02/18 18:05
54,1 Max
41,5
29
16,4
3,86
-8,69
-21,2
-33,8
-46,3
-58,9 Min
Max
Z
Y
0,00
500,00
1000,00 (mm)
250,00
750,00

Figure 7.12: Abort 8g local model - direct stress patterns on diagonal rods.

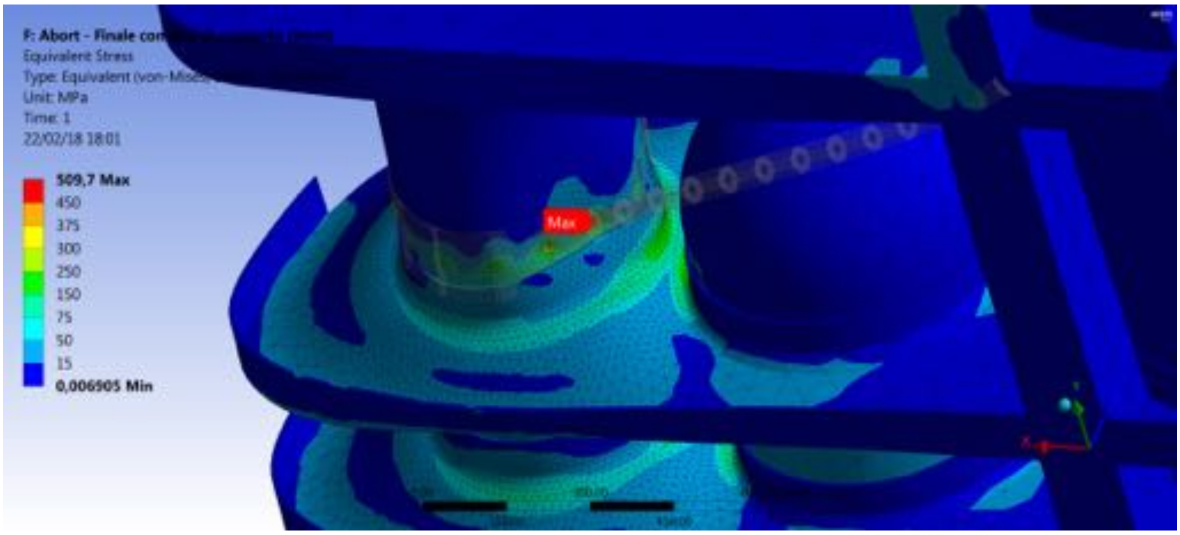
F: Abort - Finale co
Equivalent Stress
Type: Equivalent (von-Mises
Unit: MPa
Time: 1
22/02/18 18:01
509,7 Max
450
375
300
250
150
75
50
15
0,006905 Min
Max

Figure 7.13: Abort 8g local model - equivalent stress patterns with diagonal rods frame (detail).

7.3 Improved Concepts

7.3.1 Thrust Frame

The results of the launch abort analysis have underlined a significant deformation of main body frames that supports the strong load generated by the engines during this emergency maneuver. Regrading strength conditions, all the stresses around the attachment area of the engines and in the bonding interfaces between frames and pressurized module are within the range of safety factor. What is relevant, even if not critical for the structure, is the deformation of the frames, they are subjected to peak displacements of up to 9 mm, value near to the frame thickness which is 10 mm. With this level of deformation the assumed plate behavior is no more valid and membrane effects come into play. The resulting large deformations are ascribed to the structural concept of the engine attachment and the resulting load path. Frames are loaded normal to their plane therefore forced to assume a plate behavior. Together with frames also outer skin panels absorbs part of the total thrust but their contribution is lower than frames. Moreover, skin panels could be subjected to buckling (not covered in our analysis) due to the compressive load. The configuration of frames and skin panel in withstanding the abort thrust is not efficient in terms of load path, even if strength verification is satisfied and large deformation can be allowed for an emergence maneuver since it is expected that the vehicle will be extensively inspected before a new flight. The results of the simulations and the resulting conclusion explained so far led us to completely rethink about the structural concept of the engine attachment.

The main cause of large deformation is the transfer of thrust to primary structure through loads acting perpendicularly of frame plane. A better configuration is to transfer them through shear loads acting on the pressurized module. This is possible with the use of a thrust frame that decouple engines from main body frames. Thrust frames are extensively used in launchers and its operation has been validated since the beginning of the space era. The structure link the engine rack with the launcher primary structure and thrust loads are transferred by axial and radial forces acting respectively on longitudinal elements and frames. The thrust frame is essentially a truss structure, the interfaces with engine and launcher are done using lugs and pins. The proposed geometry for the new thrust frame of the Dream Chaser is composed of four circular rods made in unidirectional composite with lugs at their ends. Interface lugs are present on the pressurized module in order to link the frame on the central core of the primary structure and transfer thrust through shear loads. Adopting a lug configuration a fuselage-like frame within the pressurized module is needed, this will be clear afterwards. A similar configuration is adopted on the engine structure, an annular ring wrap the thrust chamber and provide the housing for lugs needed to fasten the engine on the thrust frame. Main body frame of the vehicle are still used, but only to support inertial loads of the engine through each flight attitude. Using an axially sliding join it is possible to decouple the action of the thrust and inertial loads. Thrust frame absorbs only the axial thrust and each frame carry inertial loads by in-plane loads. Joining of each part is performed by means of pins. Rendering of the thrust frame concept are reported in figures 7.14a and 7.14b with detailed views and the assembled structure mounted on the Dream Chaser in figures 7.15 and 7.16.

The conceptual analysis of the forces that are exchanged between each part of the new configuration shows that the new load path changed by the thrust frame is effectively the one that it was stated. Figure 7.17 shows the loads on each part, in particular the thrust generated by the engine is absorbed as axial loads on each rods. Then, these axial loads are transferred to pressurized module by means of lug-pin fastening. Loads on the pressurized module are decomposed along axial and radial directions.

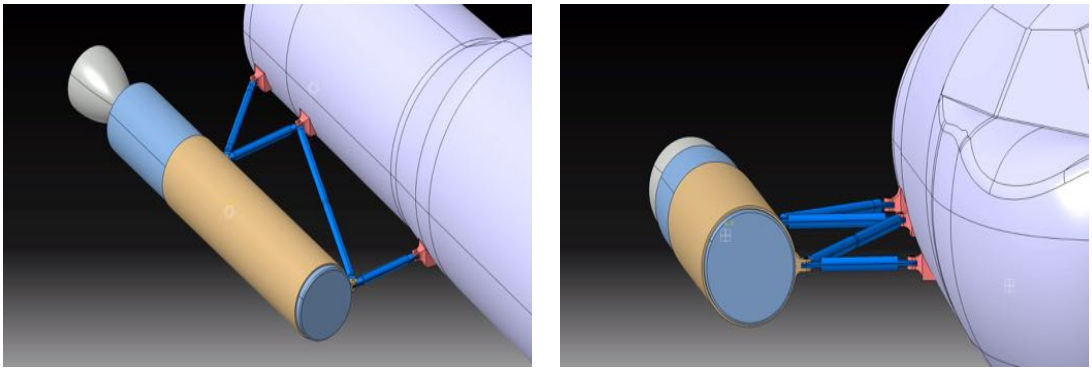

(a) Assembly of the Thrust Frame. **(b)** Frontal view of Thrust Frame assembled.

Figure 7.14: Rendering of the Thrust Frame concept.

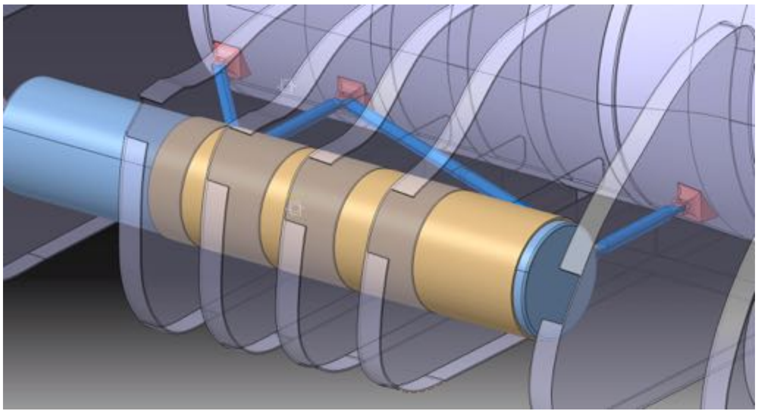

Figure 7.15: Lateral view with visible holes on the frames that allow the passage of the diagonal rod.

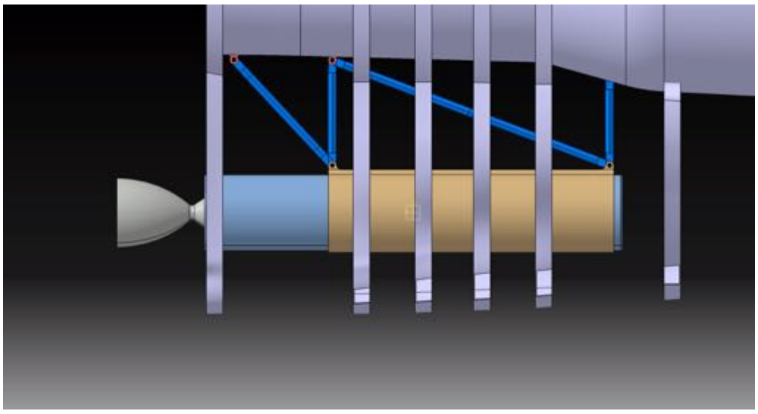

Figure 7.16: Top view of the Thrust Frame area.

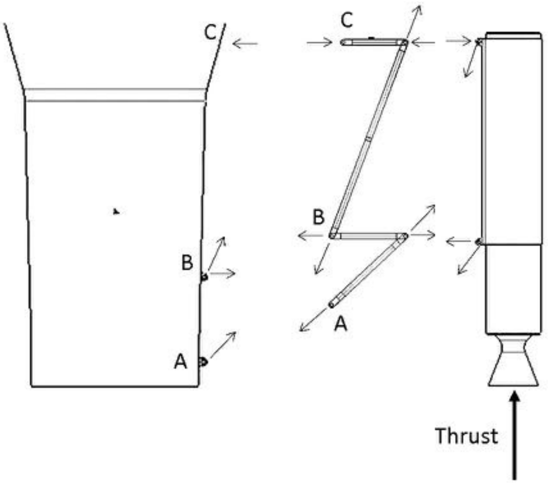

Figure 7.17: Schematic view of the forces acting on each part of the Thrust Frame during firing of the engine (only one side shown). Letters A, B, C represents points of attachments between rods and pressurized module

The axial components impose a compressive force on the module. The radial components acts inward on the surface and these are exactly shear loads required. In order for the pressurized module to support axial and radial components and to provide supports for the lugs, the pressurized module shell must be stiffened with annular frames and stringers. The truss structure including also engine annular ring is one time hyperstatic in terms of internal forces thus making the structure one time fail safe. For a preliminary estimation of the degree of redundancy of the structure, annular ring can be considered as a rod. The possible nodal displacements are related by the formula $n = 2N - R$ where N is the number of nodes and R is number of external reactions forces while the degree of redundancy is $i = M - n$ with M number of axial forces in the rods. For the thrust frame $N = 5, R = 6$ and $M = 5$ therefore $i = 1$. With the ideas exposed above, which we leave as future works due to a lack of time needed to perform a correct analysis, we are confident that the deformation will be lowered even in the case of abort and in general the thrust loads will be guided more efficiently during each engine burn.

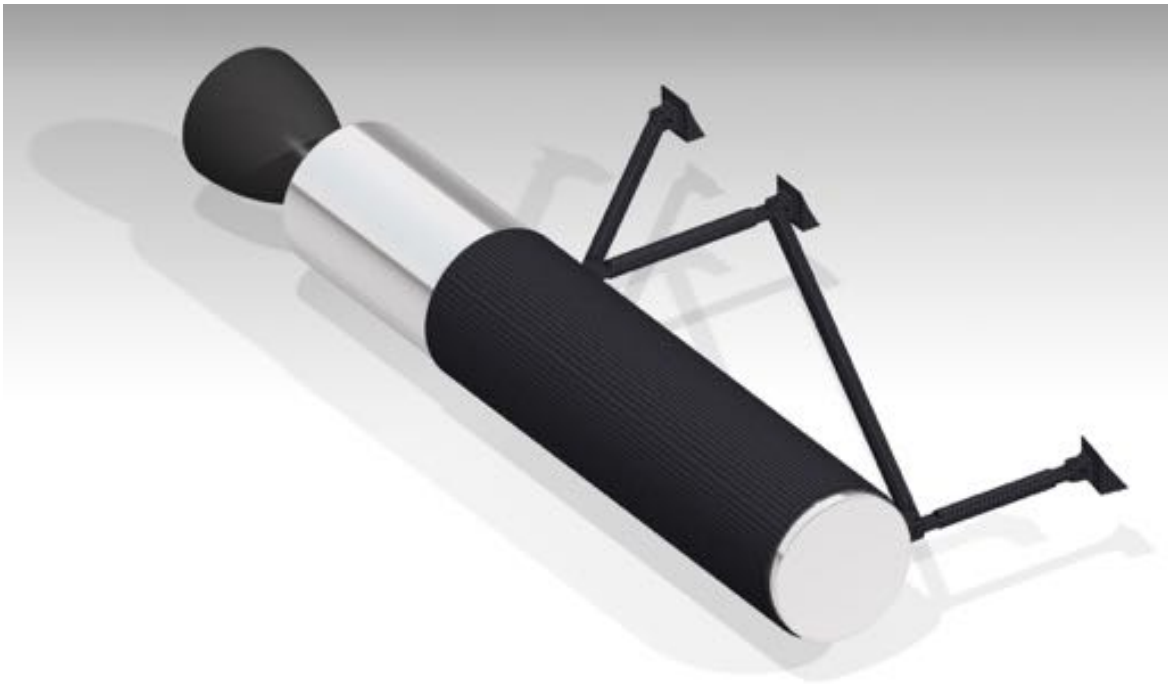

7.3.2 Wing Root Fittings

As for the case of the thrust frame, the previous configuration adopted for the wing root fittings have to be changed. Here the needs for a configuration change are not only about structural considerations but are driven also by manufacturing processes and assembly procedures used to build the entire system. Results of the FEM analysis in the pullup scenario shows a large deformation around fin trailing edge on root section attributed to the lack of a root rib. The resulting deformation is not tolerable therefore must be eliminated. Another issue is posed by the type of joining technology used to assemble fin spars with fin root junction plate and its compatibility with their materials. Using a riveted joint to fasten composite-Aluminum assembly have some drawbacks, either of structural and technological nature. In a multiple riveted or bolted joint the load path from one part to another cannot be completely determined and specific handbooks suggests different uncertainty factors applicable during joint design. In the chosen configuration this uncertainty is amplified due to the different directional properties of composites and Aluminum and, this would have required an increase uncertainty factors with implications on weight cost and dimensions of the joint. The use of different materials poses risks also regrading galvanic corrosion. Regarding manufacturing considerations, a first concern is the drilling of composite which is known to be a not easily machinable material, requiring specific tools and technologies and sometimes the final result is not comparable to drilling metal materials. Problems may arise during final assembly of the fin onto fuselage ribs since five different parts have to fit one to each other simultaneously, this requires tight tolerances and extreme manufacturing precision that are difficult to achieve.

Taking into consideration the issues discussed so far, the new concept of fin root fittings comprises a root bulkhead with lugs on fuselage side and five sockets on fin side that slots the spars.

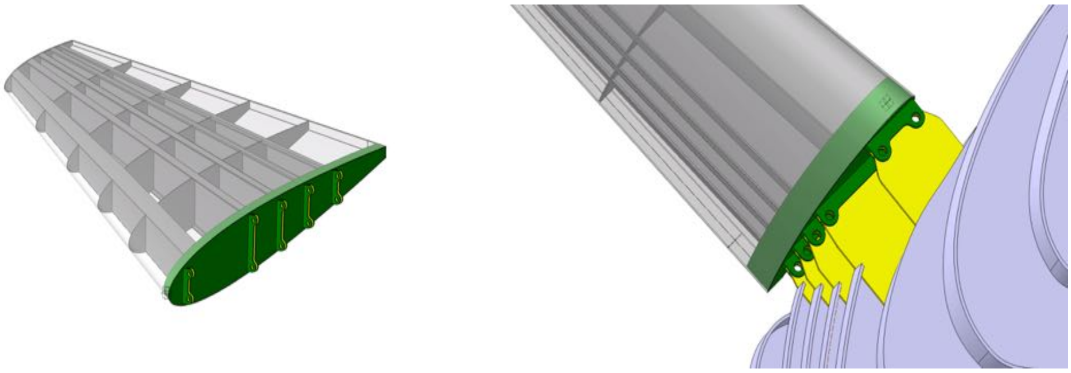

(a) View of the root bulkhead with spars assembled and lugs on the opposite side

(b) Detail of lug fittings between bulkhead and fuselage rib junction plates (no pins are shown)

Figure 7.18: Root bulkhead concept with view of its components (spar sockets not drawn)

The bulkhead placed at fin root section stiffen the root section thus eliminating the excessive deformation in that area. Sockets are meant to restrain the root end of the spar by embracing it, no drilling are then needed, providing a safe and rigid constraint. The important change is on the kind of fitting device between bulkhead and fuselage ribs. Five lug-pin joints are used in place of junction plates to transfer aerodynamic loads to fuselage structure, this type of configuration is extensively used in aeronautic structures.

On a backswept wing, as could be considered the outboard fins, all the type of stresses are acting on its structure. Loads on root section are the same as for the previous fitting configuration but now the manner in which they are transferred ribs is different. The new

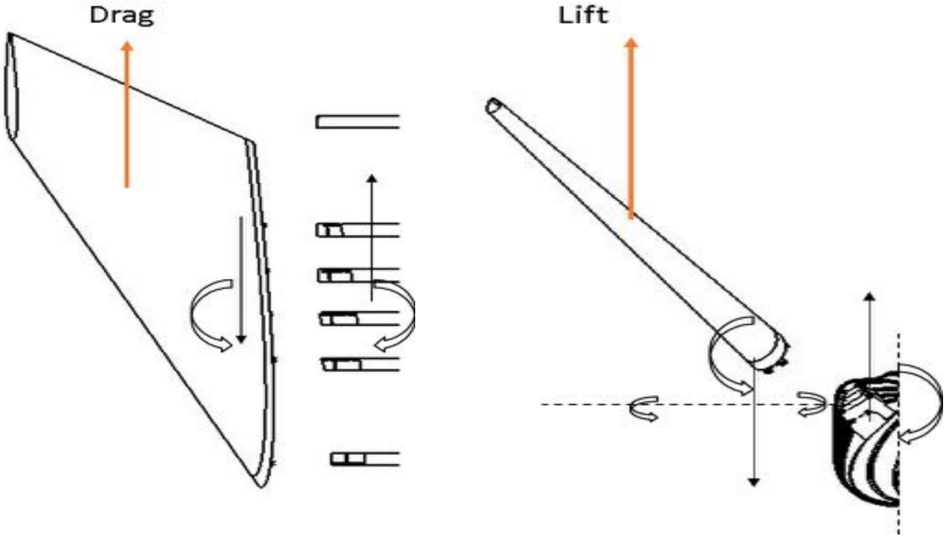

(a) Top view of wing root fitting area with forces caused by Drag

(b) Front view of wing root fitting area with forces and torque moment caused by Lift

Figure 7.19: Views of loads acting on bulkhead assembly and on junction plates

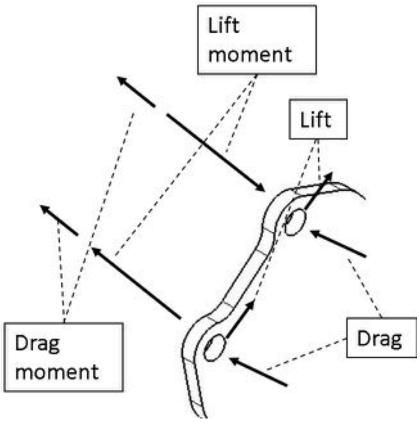

Figure 7.20: Representation of force components acting on a fuselage rib lug

situation is depicted in figure 7.18.

Stresses on skin and spars on fin root section are now absorbed by the stiff bulkhead and then passed on fuselage ribs through lug-pin joints. From the load scheme in figure 7.19 forces are distributed on each joint acting on fuselage rib plane and on its normal direction. Lift is transferred by shear of pins while Drag loads each joint in a plane normal to the ribs and generates bending on lug root section. Bending moments on fin root section are absorbed by each joint through alternate shear forces of pins, these moments are generated by Lift and Drag. The first one generates an alternate shear lying on each rib plane. The second one loads pins of one joint with evenly distributed shear loads in the same directions but shear loads are anti-symmetric on different joints with respect to a vertical axis passing through the center of the assembly, figure 7.19a shows this loading scheme. Torsion is transferred through multiple couple acting on a plane parallel to bulkhead and passing through lugs. This loading condition has the same effect as for the Drag load but forces are opposite to each other on a single joint.

Fuselage ribs are effective against in-plane loads which are the most severe. As explained before, ribs are not subjected only on in-plane loads but there are force components in out-of-plane directions. These components shall be much lower with respect to the others since ribs are not as effective as for in-plane loads and a further analysis, which we leave as future work, should confirm this. In the case of significant out-of-plane loads, modification on the design have to be done and a longitudinal element that react against normal loads must be designed.

The bulkhead is designed to be manufactured with composite materials. Rib sockets, lugs and bulkhead itself are all made with composites. Our proposed manufacturing process is to produce the fin structure and bulkhead separately and then bond the two pieces together in a single curing cycle. This new process avoid assembly issues of matching five different joint parts on their equivalents mounted on fuselage ribs. Now the fittings occurs between bulkhead lugs and ribs junction plates, this may seen a similar problem as in the previous wing root fitting configuration but with the use of lugs, the inevitable manufacturing imperfections could be compensated by variable tolerances given on each lug therefore promoting the assembly of fin into Dream Chaser central body.

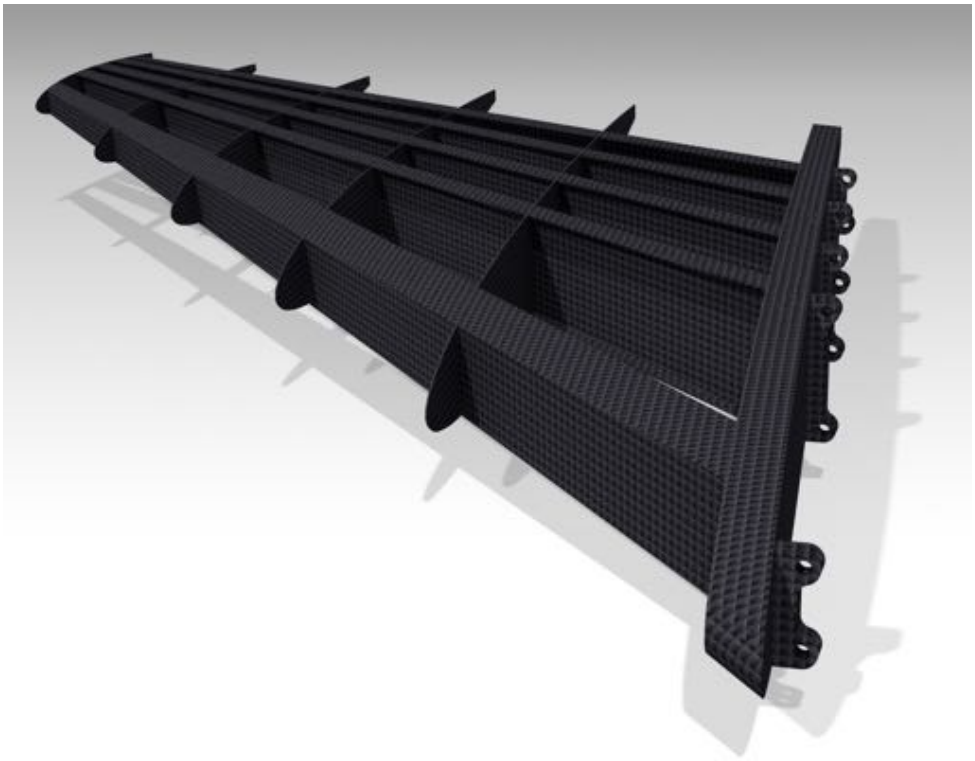

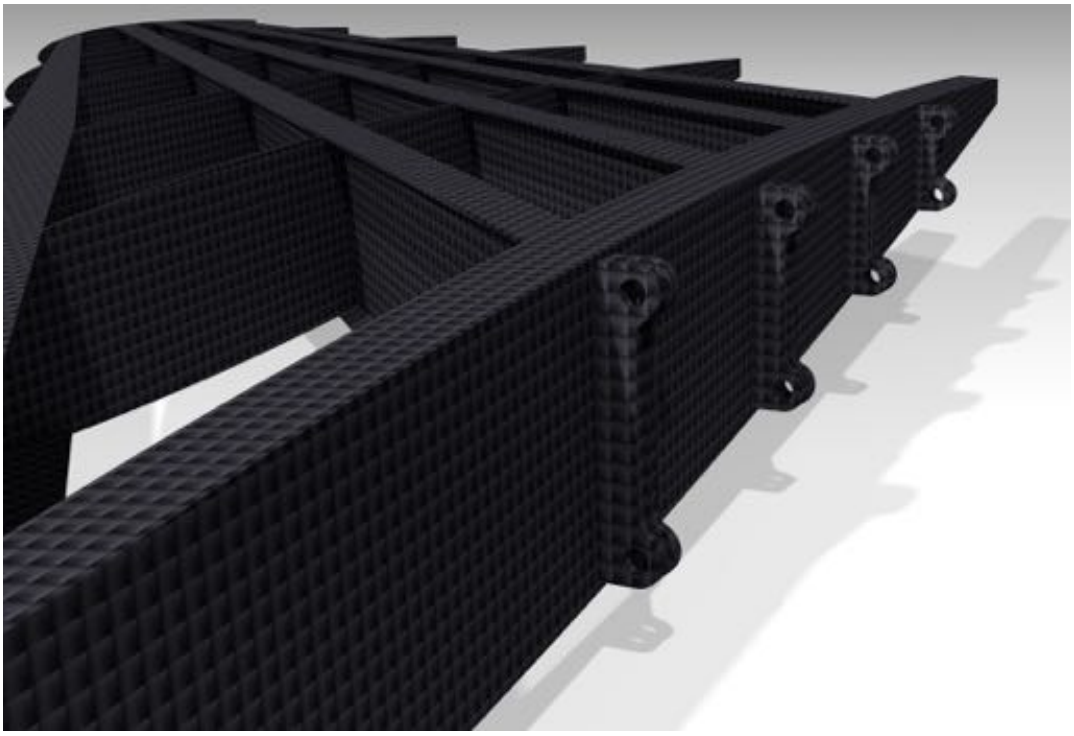

Chapter 8

Conclusions

At the end of our work, we found a paper [8] where most of our assumptions based from previous work on HL-20 have been validated. First of all the abort thrust is generated by Dream Chaser main engines, called therefore "integrated propulsion system". All the advantages regarding separation rates, cross-range coverage to reach landing site after separation and compliance with other requirements and constraints regarding aerothermodynamic loads and crew acceleration limits have been considered. Second, the Abort case analysed in our work has taken into account as one of a wider number of abort scenarios during Dream Chaser development. In figure 8.1 is listed the complete set of these investigated scenarios. Of particular interest are scenario AA-5 and AA-7, the same we described in section 4.2 and analysed in section6.1, even if one of our assumption did not match completely the result obtained by others and reported in literature. In reference [3] the Authors reported a 10 psi overpressure is not negligible and is instead the critical load for the lateral access panels. Few preliminary considerations should be taken in respect of this aspect. Actually, the aforementioned problem regards HL-20, since available informations do not prove the existence of such lateral access

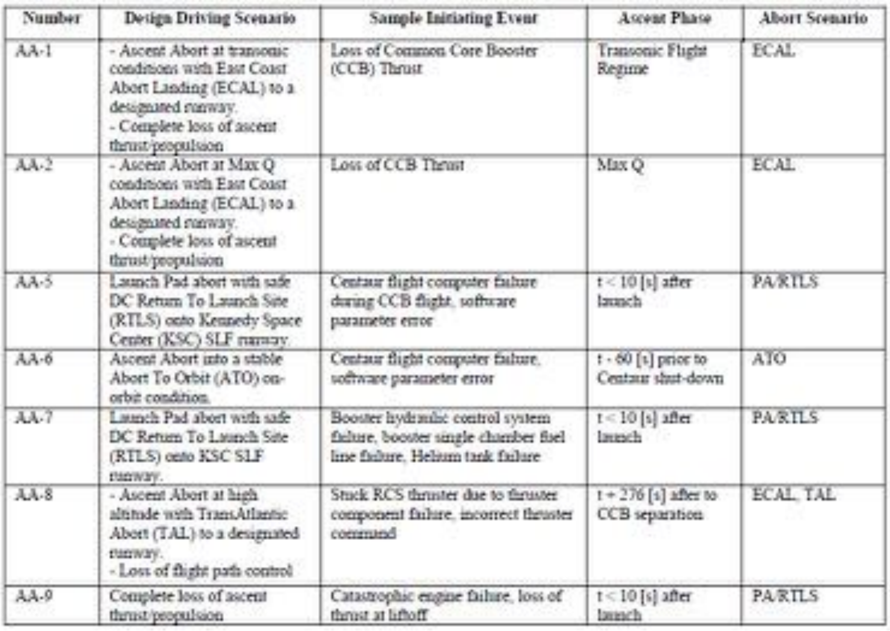

Number	Design Driving Scenario	Sample Initiating Event	Ascent Phase	Abort Scenario
AA-1	- Ascent Abort at transonic conditions with East Coast Abort Landing (ECAL) to a designated runway. - Complete loss of ascent thrust/propulsion	Loss of Common Core Booster (CCB) Thrust	Transonic Flight Regime	ECAL
AA-2	- Ascent Abort at Max Q conditions with East Coast Abort Landing (ECAL) to a designated runway. - Complete loss of ascent thrust/propulsion	Loss of CCB Thrust	Max Q	ECAL
AA-5	Launch Pad abort with safe DC Return To Launch Site (RTLS) onto Kennedy Space Center (KSC) SLF runway.	Centaur flight computer failure during CCB flight, software parameter error	t < 10 [s] after launch	PA/RTLS
AA-6	Ascent Abort into a stable Abort To Orbit (ATO) on-orbit condition.	Centaur flight computer failure, software parameter error	t - 60 [s] prior to Centaur shut-down	ATO
AA-7	Launch Pad abort with safe DC Return To Launch Site (RTLS) onto KSC SLF runway.	Booster hydraulic control system failure, booster single chamber fuel line failure, Helium tank failure	t < 10 [s] after launch	PA/RTLS
AA-8	- Ascent Abort at high altitude with TransAtlantic Abort (TAL) to a designated runway. - Loss of flight path control	Stuck RCS thruster due to thruster component failure, incorrect thruster command	t ≈ 276 [s] after to CCB separation	ECAL, TAL
AA-9	Complete loss of ascent thrust/propulsion	Catastrophic engine failure, loss of thrust at liftoff	t < 10 [s] after launch	PA/RTLS

Figure 8.1: Dream Chaser Abort scenarios with possible failures that may cause launch abort and where it could verify along ascent trajectory (adapted from [8])

panels in the Dream Chaser. Moreover, materials are different, the number of frames is higher and their spacing is lower: these factors can influence the issue highlighted by the Authors. Last proof is the recent, and specific, abort analysis[8] carried out by Sierra Nevada, where this problem is not mentioned. We believe that one of the future works should account for this aspect and investigate if the 10 psi overpressure could have the same effect on Dream Chaser static structural behaviour.

In conclusion of this report, we learnt the advantages composite materials display against conventional metals arrangements employed in the Aeronautical sector, even though the type of loads encountered are all the same, so as the theory one can apply to approach a design study, however complex it could be. Dream Chaser lifting-body concept features unique manufacturing and engineering solutions that made it a real challenge to deal with since the beginning of this project. Nevertheless, we demonstrated through hard, dedicated work and critical/engineer thought that everything can be reduced, at least in a context of a preliminary study, to simple but representative solutions in order to get useful insights on real structures behaviours.
In the end, a wing is always a wing, however it could be interfaced to a fuselage of an aircraft, or, to better say, a spaceplane. Of course, it was impossible to perform every kind of analysis necessary to fully assess the structural integrity of our vehicle concept during each phase of its typical mission; still, we provided a solid base of analyses methodologies to be exploited by further studies and future improvements/developments/implementations undertaken by anyone interested in this topic. Who knows, maybe we will inspire future young engineers like us to pursue the same path.

Appendix A

MATLAB codes

This appendix presents the MATLAB codes for the reentry analysis at Mach 10, the preliminary design of the structure and the design of outward fins with their root fittings.

A.1 Reentry phase at Mach 10

```
%==========================================================================
%       CALCOLO DELLE CONDIZIONI DI RIENTRO ATMOSFERICO A MACH 10
%==========================================================================
% data di ultima modifica: 22/01/2018
% autore modifica: Raffa
% -------------------------------------------------------------------
%
% - lun 22/01:  correttte le equazioni del moto lungo z. compariva il
%               cotributo di portanza delle superfici di controllo in
%               rollio, queste generano un momoento puro
%
% - lun 26/06:  aggiunte le equazioni di equilibrio al momento.
%               L'equilibrio in beccheggio considera contributi
%               diversi tra fins e upper body flaps.
%
% - mar 27/06: controllate e commentate le lunghezze di momento
%              aggiornati i dati aria a quota 53.25 km (ora errore del
%              1.33% e g = 1.15g)
%
%
%-------------------------------------------------------------------
clear; close all; clc;
% PARAMETRI AERODINAMICI (dati riferiti rispetto al sistema ASSI CORPO)
alfa=30;                % Angolo di attacco [°]
alfa_rad=alfa*pi/180;   % Angolo di attacco [rad]
beta=2;                 % Angolo di derapata [°]
beta_rad=beta*pi/180;   % Angolo di derapata [rad]
Re=1.06e6;              % Numero di Reynolds
% Dati aria (tabelle atmosfera standard - 1976 Standard Atmosphere Calculator)
h=53250;                % Quota [m]
ro=0.000661813;         % Densità [kg/m^3]
muv=0.0000169085;       % Viscosità [(N s)/m^2]
a=325.938;              % Velocità del suono [m/s]
T=264.350;              % Temperatura [K]
p=50.22;                % Pressione statica [N/m^2]
% Coefficienti aerodinamici (dati ottenuti mediante lettore digitale di
% immagini - WebPlotDigitizer)
CD=0.359564;            % Coefficiente di portanza
CL=0.467338;            % Coefficiente di resistenza
Cm_30=-0.014909;        % Coefficiente di momento di beccheggio @ 30°
```

```
Cm_23_5=-0.002322;      % Coefficiente di momento di beccheggio @ 23.5°
CY=0.011358;            % Coefficiente di devianza
Croll= 6.9e-3;          % Coefficiente di rollio
Cyaw= 6.4e-3;           % Coefficiente di imbardata
% CARATTERISTICHE GEOMETRICHE VEICOLO (valori di riferimento)
l=8.2;       % Lunghezza [m]
b=4.51;      % Larghezza [m]
S_ref=l*b;   % Area in pianta, ali escluse [m^2]
lt= 3.5;     % (Pitch) - Braccio longitudinale upper body flap
lr= 1.3;     % (Roll) - Braccio trasversale (dall'asse)
ly= 3.5;     % (Yaw) - Braccio longitudinale del timone
 % (per ora stimato pari a quello dei body flap)
lf= 4;       % (Pitch) - Braccio longitudinale alettoni ali
% Calcolo del peso locale
mug=3.986e14;            % Parametro gravitazionale della Terra [m^3/s^2]
mass=9000;               % Massa del veicolo [kg]
r=6378000+h;             % Distanza dal centro della Terra [m]
W=mass*mug/(r^2);        % Peso locale [N]
g=W/mass;                % Accelerazione gravitazionale locale [m/s^2]
% FORZE AERODINAMICHE
U=(muv*Re)/(ro*l);                % Velocità asintotica [m/s]
q=0.5*ro*(U^2);                   % Pressione dinamica [N/m^2]
L=q*S_ref*CL;                     % Portanza [N]
D=q*S_ref*CD;                     % Resistenza [N]
Y=q*S_ref*CY;                     % Devianza (o forza laterale) [N]
AE=L/D;                           % Efficienza aerodinamica
M_pitch_30=q*S_ref*Cm_30*l;       % Momento di beccheggio @ 30° [N m]
M_pitch_23_5=q*S_ref*Cm_23_5*l;   % Momento di beccheggio @ 23.5° [N m]
M_roll=q*S_ref*Croll*b;           % Momento di rollio [N m]
M_yaw=q*S_ref*Cyaw*b;             % Momento di imbardata [N m]
% Errore sul numero di Mach ottenuto rispetto a quello nominale
M=U/a;                          % Numero di Mach ottenuto = 10.0113
errore_abs=abs(M-10);           % Errore assoluto
errore_rel=errore_abs/10*100;  % Errore relativo percentuale

%% CALCOLO DEI CARICHI INERZIALI MEDIANTE L'EQUAZIONI DEL MOTO
%  (eq. della quantità di moto)
% ------------------------------------------------------------------
%   |F_aero + W + F_inerziali + F_controllo = 0
%   |
%   |M_aero + M_controllo = 0
%
%   -Forze inerziali considerate come carichi esterni
%   -Forze di controllo date dal contributo deportante in coda
% ------------------------------------------------------------------
Lr = - M_roll/lr;                       % Portanza di controllo in rollio
Lf = -M_pitch_23_5/(2*lf);              % Contributo di portanza di controllo...
in beccheggio per le fins
Lb = -(M_pitch_30 +(2*Lf*lf))/(2*lt);  % Contributo di portanza di controllo...
in beccheggio per i body flaps
Ly = - M_yaw/ly;                        % Portanza di controllo in imbardata
% Accelerazione longitudinale [m/s^2]
ax=(L*sin(alfa_rad)-D*(cos(alfa_rad)+cos(beta_rad))-W*sin(alfa_rad))/mass;
% Accelerazione laterale [m/s^2]
ay=(Y+D*sin(beta_rad)-Ly)/mass;
% Accelerazione verticale [m/s^2]
az=(-L*cos(alfa_rad)-D*sin(alfa_rad)+W*cos(alfa_rad)+Lb+Lf)/mass;
% Modulo accelerazione totale [m/s^2]
A=sqrt((ax^2)+(ay^2)+(az^2));
g0=9.80665;                 % Accelerazione gravitazionale a livello del suolo [m/s^2]
n=A/g0;                     % Tasso di decelerazione
nx=ax/g0;                   % Fattore di carico longitudinale
ny=ay/g0;                   % Fattore di carico laterale
nz=az/g0;                   % Fattore di carico verticale
%% Display dei risultati
disp('============================================================')
disp('                      INPUT DATA                            ')
disp('============================================================')
disp('            Aerodynamic parameters @ Mach=10                ')
disp('-----------------------------------------------------------------')
disp([sprintf(' Alpha (angle of attack) = %3.0f',alfa) '°'])
disp([sprintf(' Beta (sideslip angle) = %3.0f',beta) '°'])
disp([sprintf(' Re (lenght Reynolds number) = %0.5g',Re) ])
disp([sprintf(' CD (Drag Coefficient) = %3.5f',CD) ])
disp([sprintf(' CL (Lift Coefficient) = %3.5f',CL) ])
disp([sprintf(' CY (Side-force Coefficient) = %3.5f',CY) ])
disp([sprintf(' Cm (Pitching-Moment Coefficient) = %3.5f',Cm_30) ])
disp('                                                                 ')
disp('                                                                 ')
disp('                      Air data (ICAO)                            ')
disp('-----------------------------------------------------------------')
disp([sprintf(' h (Height) = %3.2f',h/1000) ' km'])
disp([sprintf(' rho (Density) = %3.5f',ro) ' kg/m^3'])
disp([sprintf(' mu (Dynamic viscosity) = %0.5g',muv) ' kg/m^3'])
disp([sprintf(' a (Sound speed) = %3.2f',a) ' m/s'])
disp([sprintf(' T (Static temperature) = %3.2f',T) ' K'])
disp([sprintf(' p (Static pressure) = %3.2f',p) ' Pa'])
disp('                                                                 ')
disp('                                                                 ')
disp('             DREAM CHASER geometrical features                   ')
disp('-----------------------------------------------------------------')
disp([sprintf(' l (Reference body lenght) = %3.2f',l) ' m'])
disp([sprintf(' b (Reference body span) = %3.2f',b) ' m'])
disp([sprintf(' Sref (Basic body planform area, fins excluded) = %3.2f',S_ref) ' m^2'])
disp('                                                                 ')
disp('                                                                 ')
disp('=================================================================')
disp('                           RESULTS                               ')
disp('=================================================================')
disp('                       Inertial loads                            ')
disp('-----------------------------------------------------------------')
disp([sprintf(' W (Local weight) = %3.2f',W) ' N'])
disp([sprintf(' ax (Longitudinal acceleration) = %3.2f',ax) ' m/(s^2)'])
disp([sprintf(' ay (Lateral acceleration) = %3.2f',ay) ' m/(s^2)'])
disp([sprintf(' az (Vertical acceleration) = %3.2f',az) ' m/(s^2)'])
disp([sprintf(' A (Absolute acceleration module) = %3.2f',A) ' m/(s^2)'])
disp([sprintf(' Deceleration rate = %3.2f',n) 'g'])
disp([sprintf(' nx (Longitudinal load factor) = %3.2f',nx) 'g'])
disp([sprintf(' ny (Lateral load factor) = %3.2f',ny) 'g'])
disp([sprintf(' nz (Vertical load factor) = %3.2f',nz) 'g'])
disp('                                                                 ')
disp('                                                                 ')
disp('                       Aerodynamic loads                         ')
disp('-----------------------------------------------------------------')
disp([sprintf(' L (Lift) = %3.2f',L) ' N'])
disp([sprintf(' D (Drag) = %3.2f',D) ' N'])
disp([sprintf(' L/D (Lift-to-Drag ratio) = %3.1f',AE)])
disp([sprintf(' Y (Side-Force) = %3.2f',Y) ' N'])
disp([sprintf(' Mroll (Rolling Moment) = %3.2f',M_roll) ' N m'])
disp([sprintf(' Mpitch (Pitching Moment) = %3.2f',M_pitch_30) ' N m'])
disp([sprintf(' Myaw (Yawing Moment) = %3.2f',M_yaw) ' N m'])
disp([sprintf(' Lr (Rolling control lift, lower body flaps) = %3.2f',Lr) ' N'])
disp([sprintf(' Lb (Pitching control lift, upper body flaps) = %3.2f',Lb) ' N'])
disp([sprintf(' Lf (Pitching control lift, fins) = %3.2f',Lf) ' N'])
disp([sprintf(' Ly (Yawing control lift, rudder) = %3.2f',Ly) ' N'])
disp('                                                                 ')
disp('                                                                 ')
disp('                    Data error analysis                          ')
disp('-----------------------------------------------------------------')
disp([sprintf(' Relative Error on Mach n° computation = %3.2f',errore_rel) '%'])
```

A.2 Preliminary Structural Analysis

The following code is used in Chapter 3 during the preliminary analysis of the structure

```
%---------------------------
%{
DIMENSIONAMENTO PRELIMINARE SPESSORI SEZIONE
%% Usare dopo aver runnato lo script reentry phase at mach 10%%
La sezione considerata è schematizzata nel file CATIA schema sezione con
relative dimensioni
-subfunction: tau_sys
-Ultima modifica: 12/07/2017 Raffo
%}
%---------------------------
%% DATI GEOMETRICI
R=0.860;         % raggio [m]
v=3.516;        % larghezza scafo [m]
h=0.100;         % altezza trave di chiglia [m]
b=0.150;          % larghezza trave di chiglia [m]
k=0.936;            % braccio tratto di base [m]
c=k-0.386;         % altezza baricentro sezione dalla base [m]
a=1.417;        % lunghezza tratto inclinato [m]
beta=(50*pi)/180;  % angolo inclinazione tratto obliquo [rad]
f=k-c-R;       % distanza tra baricentro e punto 6 [mm]
alpha3=13*pi/180;  % angolo tra punto 6 e punto 3 [mm]
alpha5=100*pi/180; % angolo tra punto 6 e punto 5 [mm]
p1=0.743;    % braccio del tratto obliquo [m]
A=0.692;     % area della cella [m2]
w=0.370;       % distanza tra travi di chiglia [m]
%% DATI MATERIALE
sigma=2700e6;    % [Pa]
tau=260e6;       % [Pa]
sf=2.5;        % fattore di sicurezza
%% proprietà geometriche della sconnessione %%
%assi riferiti come: z direzione muso, x direzione orizzontale della
%sezione trasversale, y direzione verticale della sezione trasversale verso
%l'alto
z=6.95; %[m] posizione della sconnessione per calcolo centina
y=2*R+h; %[m] altezza
A_pianta=v*z; %fattore correttivo dovuto al fatto che l'area in pianta non è un quadrato
%A_laterale=z*y*0.6; %fattore correttivo da stimare meglio
Gx=0; %[m]
Gz=1.687; %[m]
Gy=0.888; %[m]
G=[Gx,Gy,Gz];
Cp_y=0.3; %[m] posizione centro pressione
Cp_x=0; %[m]
Cp_z=2.363; %[m]
Cp=[Cp_x,Cp_y,Cp_z];
d=G-Cp; %vettore distanza tra baricentro e centro di pressione
d=norm(d);
theta=atan((Gy-Cp_y)/(Gz-Cp_z)); %angolo tra baricentro e centro di pressione
m_loc=mass*z/l; %massa del pezzo di aereo dal muso al punto sconnessione
%% calcolo carichi %%
D_loc_y=D*A_pianta/S_ref*sin(alfa_rad); %valore locale del carico di taglio
%dovuto a resistenza
D_loc_z=D*A_pianta/S_ref*cos(alfa_rad);
L_loc_y=L*0.5*A_pianta/S_ref*cos(alfa_rad); %valore locale del carico di taglio
%dovuto a portanza
L_loc_z=L*0.5*A_pianta/S_ref*sin(alfa_rad);
W_loc_y=m_loc*g*cos(alfa_rad);% peso locale
W_loc_z=m_loc*g*sin(alfa_rad);
%Y_loc=Y*0.3*A_laterale/S_ref; %valore locale del carico di taglio dovuto a devianza
F_inertia_y=m_loc*(-az); %carico inerziale lungo la verticale alla centina
F_inertia_z=m_loc*(-ax); %carico inerziale lungo l'asse orizzontale della centina
Sy=(L_loc_y-W_loc_y+D_loc_y+F_inertia_y);  % [N]
N=-(D_loc_z-L_loc_z)-W_loc_z+F_inertia_z;  % [N]
M_pitch_loc=-Sy*(z-Gx)+N*(Gy-h/2); %momento di beccheggio dovuto alla portanza locale
```

```
M_x=-M_pitch_loc; % [Nm]
%% MOMENTO FLETTENTE & CARICO ASSIALE
% dimensionamento di t1 (Navier)
% la tensione maggiore si ha sulle alette della sezione a C, per y=h/2
t1=((abs(M_x)*h)/(4*b*h^2+h^3/3)+abs(N)/(2*(2*b+h)))*sf/sigma;
%% TENSIONI DI TAGLIO
% centro del cerchio scelto come polo dei momenti per il calcolo di q0
% valori iniziali del ciclo
t2=1;
t3=1;
q0=5;
% SOLUZIONE SISTEMA NON-LINEARE
fun=@tau_sys;
x0=[t2,t3,q0];
options = optimoptions('fsolve','Display','iter','MaxFunctionEvaluations', 2000);
[x,fval] = fsolve(@tau_sys,x0,options);
t2=x(1);
t3=x(2);
q0=x(3);
```

The function tau_sys is a subfunction of the previous code needed to evaluate shear stresses in the cross section

```
function [F]=tau_sys(x)
%-----------definizione funzione sistema non lineare------------------
% t2=x(1)
% t3=x(2)
% q0=x(3)
%
% Ultima modifica: 12/07/2017 Raffo
%--------------------------------------------------------------------
%% DATI GEOMETRICI
R=0.860;         % raggio [m]
v=3.516;        % larghezza scafo [m]
h=0.100;         % altezza trave di chiglia [m]
k=0.939;            % braccio tratto di base [m]
c=k-0.386;         % altezza baricentro sezione dalla base [m]
a=1.417;        % lunghezza tratto inclinato [m]
beta=(50*pi)/180;  % angolo inclinazione tratto obliquo [rad]
f=k-c-R;       % distanza tra baricentro e punto 6 [mm]
alpha3=13*pi/180;  % angolo tra punto 6 e punto 3 [mm]
alpha5=100*pi/180; % angolo tra punto 6 e punto 5 [mm]
p1=0.743;    % braccio del tratto obliquo [m]
A=0.692;     % area della cella [m2]
w=0.370;       % distanza tra travi di chiglia [m]
t1=0.0054;       % spessore trave di chiglia [m]
%% DATI MATERIALE
tau=260e6;       % [Pa]
sf=2.5;        % fattore di sicurezza
%% CARICHI SULLA SEZIONE
Sy=-3.214*1e4;
%% SISTEMA NON-LINERE
alpha_bar=acos(f/R);
% termini dei flussi di taglio base per calcolo q0 [ equazione F(3) ]
B1=-p1*x(2)*(c*a^2/2-sin(beta)*a^3/6)+p1*x(2)*c*v/2*a;
B2=-x(1)*R^3*(f*0.5*(alpha5^2-alpha3^2)+R*(cos(alpha5-cos(alpha3))));
B3=-x(1)*R^3*(f*alpha3-R*sin(alpha3))*(alpha5-alpha3)-t1*R*(c*h-h^2/2)*(alpha5-alpha3);
B4=-(k*c*x(2)*(v-w)^2)/4-k*x(2)*c*w*(v-w)/4;
B=B1+B2+B3+B4;
% momenti d'inerzia geometrie sezione
Jxx_cerchio=(pi*x(1)*R^3)+2*pi*x(1)*(k-c)^2;
Jxx_setto=(t1*h^3)/12 + t1*h*(c-h/2)^2;
Jxx_base=v*x(2)*c^2;
Jxxa=(x(2)*(sin(beta)^2)*a^3)/12 + x(2)*a*(c-sin(beta)*(a/2))^2;
% momento d'inerzia sezione
J_xx=Jxx_cerchio+2*Jxx_setto+Jxx_base+2*Jxxa;
% formulazione sistema non-lineare [ F(x)=0 ]
F=[-x(1)*tau/sf+x(1).*(Sy./J_xx)*(f*(alpha_bar+alpha3)-R*(sin(alpha_bar)+sin(alpha3)))...
+x(1).*(Sy./J_xx)*t1*(c*h-h^2/2)+x(3);-x(2)*tau/sf+...
x(2).*(Sy./J_xx)*(c^2/sin(beta)+c*v/2)-x(3);B+2*A*x(3).*(J_xx/Sy)];
end
```

A.3 Fin Structural Design

This code performs a preliminary sizing of the main structural members of the fin

```
%-----------------------------------
%{
-- DIMENSIONAMENTO STRUTTURALE ALA (FIN) --
-carico di progetto: manovra di pullout a 2.5 g in fase di atterraggio
Data creazione: 06/08/2017 Raffo
Data ultima modifica: 01/11/2017 Raffo
%}
%-----------------------------------
%% DATI
% Dreamchaser
mass=9000;            % massa dreamchaser
n_z=2.5;              % fattore di carico pullout
%-- geometria ala e longheroni --
b=2.637;          % altezza ala [m]
% passo longheroni alla radice [m]
w1=0.260;
w2=0.770;
w3=0.370;
w4=0.350;
w5=0.370;
% altezza longheroni [m]
h1=0.177;
h2=0.239;
h3=0.220;
h4=0.188;
h5=0.144;
% freccia longheroni [rad]
beta1=52*pi/180;
beta2=46*pi/180;
beta3=44*pi/180;
beta4=41*pi/180;
beta5=40*pi/180;
% lunghezza tratti pareti [m]
l_110=h1;              % web longherone 1
l_1_10=0.569;          % curva bordo d’attacco
l_12=0.771;            % tratto skin
l_910=l_12;            % tratto skin
l_29=h2;               % web longherone 2
l_23=0.370;            % tratto skin
l_98=l_23;             % tratto skin
l_38=h3;               % web longherone 3
l_34=0.350;            % tratto skin
l_87=l_34;             % tratto skin
l_47=h4;               % web longherone 4
l_45=0.371;            % tratto skin
l_76=l_45;             % tratto skin
l_56=h5;               % web longherone 5
% area celle sezione di radice [m2]
AI=0.032;
AII=0.173;
AIII=0.085;
AIV=0.072;
AV=0.062;
%--------------------------------
% materiali
%{
== Da catalogo materiali Ansys: Epoxy carbon woven (230 GPa) Prepreg
-Moduli resistenza [MPa]:
E_x=61340
E_y=61340
E_z=6900
G_x=19500
G_y=2700
G_z=2700
-Tensione rottura [MPa]:
Trazione:
sigma_x=805
sigma_y=805
sigma_z=50
Compressione:
sigma_x=509
sigma_y=509
sigma_z=170
Taglio
tau_xy=125
tau_yz=65
tau_xz=65
%}
sigma_y=509*1e6;   % inserire la resistenza a compressione [Pa]
tau_y=125*1e6;     % [Pa]
E=61340*1e6;       % [Pa]
G=19500*1e6;       % [Pa]
sf=2.5;
% carichi aerodinamici Pullout, la portanza viene distribuità metà sulla
% fusoliera e metà sulle ali
L_tot=n_z*mass*9.81;   % portanza totale [N]
L_wing=L_tot/4;        % portanza su una ala [N]
Mx_root=-L_wing*b/2;   % momento alla radice [Nm]
%% DIMENSIONAMENTO BOOM
%{
% sistema non-lineare
fun=@boom_sys;
x0=1e-6*[5 8 7 2 2];
options=optimoptions(’fsolve’,’Display’,’iter’,’MaxFunctionEvaluations’, 2000);
x=fsolve(fun,x0,options);
%}
%{
% sistema lineare
B=[h1^2,h2^2,h3^2,h4^2,h5^2;h1^2,h2^2,h3^2,h4^2,h5^2;...
h1^2,h2^2,h3^2,h4^2,h5^2;h1^2,h2^2,h3^2,h4^2,h5^2;h1^2,h2^2,h3^2,h4^2,h5^2];
v=(Mx_root*sf/sigma_y)*[h1/cos(beta1);h2/cos(beta2);...
h3/cos(beta3);h4/cos(beta4);h5/cos(beta5)];
x=B\v;
%}
% x=abs(x);
% prima stima delle aree
x(1)=abs(Mx_root)*sf/(5*h1*cos(beta1)*sigma_y);
x(2)=abs(Mx_root)*sf/(5*h2*cos(beta2)*sigma_y);
x(3)=abs(Mx_root)*sf/(5*h3*cos(beta3)*sigma_y);
x(4)=abs(Mx_root)*sf/(5*h4*cos(beta4)*sigma_y);
x(5)=abs(Mx_root)*sf/(5*h5*cos(beta5)*sigma_y);
% soluzione area boom
disp(’ ---- BOOM AREA SIZING [m2] ---- ’)
A1=x(1)
A2=x(2)
A3=x(3)
A4=x(4)
A5=x(5)
disp(’ ------------------------------------------- ’)
% Verifica dimensionamento
Jxx=0.5*(x(1)*h1^2+x(2)*h2^2+x(3)*h3^2+x(4)*h4^2+x(5)*h5^2);
sigma1=Mx_root*h1/(Jxx*2*cos(beta1))
sigma2=Mx_root*h2/(Jxx*2*cos(beta2))
sigma3=Mx_root*h3/(Jxx*2*cos(beta3))
sigma4=Mx_root*h4/(Jxx*2*cos(beta4))
sigma5=Mx_root*h5/(Jxx*2*cos(beta5))
% forze sui boom superiori (sezione simmetrica)
disp(’ ---- FORCES ON UPPER BOOMS (SYM. SECTION) [N] ---- ’)
P1=sigma1*A1
P2=sigma2*A2
P3=sigma3*A3
P4=sigma4*A4
P5=sigma5*A5
```

```
disp(' ---- X COMPONENT [N] ---- ')
Px1=A1*Mx_root*h1/(Jxx*2)*tan(beta1)
Px2=A2*Mx_root*h2/(Jxx*2)*tan(beta2)
Px3=A3*Mx_root*h3/(Jxx*2)*tan(beta3)
Px4=A4*Mx_root*h4/(Jxx*2)*tan(beta4)
Px5=A5*Mx_root*h5/(Jxx*2)*tan(beta5)
disp(' ------------------------------------------- ')
disp(' ---- Z COMPONENT [N] ---- ')
Pz1=A1*Mx_root*h1/(2*Jxx)
Pz2=A2*Mx_root*h2/(2*Jxx)
Pz3=A3*Mx_root*h3/(2*Jxx)
Pz4=A4*Mx_root*h4/(2*Jxx)
Pz5=A1*Mx_root*h5/(2*Jxx)
disp(' ------------------------------------------- ')
%% DIMENSIONAMENTO SKIN E WEB LONGHERONI
A=A1+A2+A3+A4+A5;    % area totale boom
Jxx=0.5*(x(1)*h1^2+x(2)*h2^2+x(3)*h3^2+x(4)*h4^2+x(5)*h5^2);   % momento inerzia sezione
Sy=L_wing;    % taglio
x_bar=(A2*w2+A3*w3+A4*w4+A5*w5)/A;   % posizione baricentro sezione
% calcolo flussi di taglio base ( sconnessione su skin superiore e bordo
% d'attacco )
disp(' ---- BASIC SHEAR FLOW ON ROOT SECTION [N/m] ---- ')
qb_110=-A1*h1*Sy/(2*Jxx);
qb_29=-A2*h2*Sy/(2*Jxx);
qb_38=-A3*h3*Sy/(2*Jxx);
qb_47=-A4*h4*Sy/(2*Jxx);
qb_56=-A5*h5*Sy/(2*Jxx);
disp(' ------------------------------------------- ')
% calcolo flussi di taglio correttivi nelle 5 celle
% PROCEDURA ITERATIVA
% inizializzazione
t1=3.5e-3;
t2=2.5e-3;
t3=2.5e-3;
t4=2.5e-3;
t5=3.5e-3;
tskin=2e-3;
dt1=1;
dt2=1;
dt3=1;
dt4=1;
dt5=1;
dtskin=1;
n=1;            % contatore iterazioni
 while (((dt1>=1e-4 || dt2>=1e-4) || (dt3>=1e-4 || dt4>=1e-4)) ||...
  (dt5>=1e-4 || dtskin>=1e-4)) && n<26
% sistema per il calcolo di dtheta/dz e flussi correttivi
C1=[l_1_10/tskin + l_110/t1,0,0,0,0,-2*AI*G];
C2=[-l_110/t1,l_12/tskin + l_110/t1 + l_910/tskin + l_29/t2,-l_29/t2,0,0,-2*AII*G];
C3=[0,-l_29/t2,(l_23+l_98)/tskin + l_29/t2 + l_38/t3,-l_38/t3,0,-2*AIII*G];
C4=[0,0,-l_38/t3,(l_34+l_87)/tskin+l_38/t3+l_47/t4,-l_47/t4,-2*AIV*G];
C5=[0,0,0,-l_47/t4,(l_45+l_76)/tskin + l_47/t4 + l_56/t5,-2*AV*G];
somma_Px=Px1*h1+Px2*h2+Px3*h3+Px4*h4+Px5*h5;
C=[C1;C2;C3;C4;C5;AI,AII,AIII,AIV,AV,0];
qb=[qb_110*l_110/t1;qb_29*l_29/t2 - qb_110*l_110/t1;...
  qb_38*l_38/t3-qb_29/t2;qb_47*l_47/t4-qb_38*l_38/t3;...
  qb_56*l_56/t5-qb_47*l_47/t4;...
  (qb_29*w2+qb_38*w3+qb_47*w4+qb_56*w5+Sy*(x_bar-w1)+somma_Px)/2];
q0=C\qb;
% flussi totali
q_110=qb_110-q0(1)+q0(2);
q_29=qb_29-q0(2)+q0(3);
q_38=qb_38-q0(3)+q0(4);
q_47=qb_47-q0(4)+q0(5);
q_56=qb_56-q0(5);
% calcolo spessori
t_1=sf*abs(q_110)/tau_y;
t_2=sf*abs(q_29)/tau_y;
t_3=sf*abs(q_38)/tau_y;
t_4=sf*abs(q_47)/tau_y;
t_5=sf*abs(q_56)/tau_y;
```

```
t_skin=sf*max(abs(q0(1:5)))/tau_y;
% differenza valori spessori rispetto a iterazione precedente
dt1=abs(t_1-t1);
dt2=abs(t_2-t2);
dt3=abs(t_3-t3);
dt4=abs(t_4-t4);
dt5=abs(t_5-t5);
dtskin=abs(t_skin-tskin);
% aggiornamento valori spessori per iterazione successiva
t1=t_1;
t2=t_2;
t3=t_3;
t4=t_4;
t5=t_5;
tskin=t_skin;
n=n+1; % conteggio nuova iterazione
 end
%{
n2=1;            % contatore iterazioni
while dt2>=1e-4 && n2<2000 %&& dt3>=1e-4 && dt4>=1e-4 && dt5>=1e-4 && dtskin>=1e-4
% sistema per il calcolo di dtheta/dz e flussi correttivi
C1=[l_1_10/tskin + l_110/t1,0,0,0,0,-2*AI*G];
C2=[-l_110/t1,l_12/tskin + l_110/t1 + l_910/tskin + l_29/t2,-l_29/t2,0,0,-2*AII*G];
C3=[0,-l_29/t2,(l_23+l_98)/tskin + l_29/t2 + l_38/t3,-l_38/t3,0,-2*AIII*G];
C4=[0,0,-l_38/t3,(l_34+l_87)/tskin+l_38/t3+l_47/t4,-l_47/t4,-2*AIV*G];
C5=[0,0,0,-l_47/t4,(l_45+l_76)/tskin + l_47/t4 + l_56/t5,-2*AV*G];
somma_Px=Px1*h1+Px2*h2+Px3*h3+Px4*h4+Px5*h5;
C=[C1;C2;C3;C4;C5;AI,AII,AIII,AIV,AV,0];
qb=[qb_110*l_110/t1;qb_29*l_29/t2 - qb_110*l_110/t1;...
qb_38*l_38/t3-qb_29/t2;qb_47*l_47/t4-qb_38*l_38/t3;...
qb_56*l_56/t5-qb_47*l_47/t4;(qb_29*w2+qb_38*w3+...
qb_47*w4+qb_56*w5-Sy*(x_bar-w1)+somma_Px)/2];
q0=C\qb;
% flussi totali
q_110=qb_110-q0(1)+q0(2);
q_29=qb_29-q0(2)+q0(3);
q_38=qb_38-q0(3)+q0(4);
q_47=qb_47-q0(4)+q0(5);
q_56=qb_56-q0(5);
% calcolo spessori
t_2=sf*abs(q_29)/tau_y;
t_3=sf*abs(q_38)/tau_y;
t_4=sf*abs(q_47)/tau_y;
t_5=sf*abs(q_56)/tau_y;
t_skin=sf*max(abs(q0(1:5)))/tau_y;
% differenza valori spessori rispetto a iterazione precedente
dt2=abs(t_2-t2);
% aggiornamento valori spessori per iterazione successiva
t2=t_2;
t3=t_3;
t4=t_4;
t5=t_5;
tskin=t_skin;
n2=n2+1; % conteggio nuova iterazione
end
disp(' ---- BASIC SHEAR FLOW ON ROOT SECTION [N/mm] ---- ')
qb_110=qb_110*1e-3
qb_29=qb_29*1e-3
qb_38=qb_38*1e-3
qb_47=qb_47*1e-3
qb_56=qb_56*1e-3
disp(' -------------------------------------------- ')
disp(' ---- TOTAL SHEAR FLOW ON ROOT SECTION [N/m] ---- ')
q_1_10=q0(1)
q_110
q_21=q0(2)
q_29
q_32=q0(3)
q_38
q_43=q0(4)
q_47
q_54=q0(5)
q_56
disp(' ------------------------------------------ ')
disp('       ')
disp(' ---- WALL THICKNESSES [mm] ---- ')
t1=t1*1e3
t2=t2*1e3
t3=t3*1e3
t4=t4*1e3
t5=t5*1e3
tskin=tskin*1e3
disp(' ------------------------------------------ ')
disp('       ')
disp(' ---- RESIDUES ---- ')
dt1
dt2
dt3
dt4
dt5
dtskin
num_iterazioni=n
disp('-------------------------------------------')
%}
```

A.4 Wing Root Fittings Design

The following MATLAB code evaluates the dimensions of the junction plates and bolt diameters in the first fin root fitting configuration

```
%----------------------
%{
  DIMENSIONAMENTO ATTACCO ALARE
-carico di progetto: manovra di pullout a 2.5 g in fase di atterraggio
dati di input da script: dimensionamento_ala
Data creazione: 21/08/2017 Raffo
Data ultima modifica: 21/08/2017 Raffo
%}
%-----------------------------------
%% DATI MATERIALE ATTACCO
% bulloni: Acciaio classe resistenza 8.8
sb_y=600e6; % tensione snervamento [Pa]
sb_u=800e6; % tensione rottura [Pa]
% attacco: Alluminio 7075-T6 (TBC)
sa_y=503e6;   % tensione snervamento [Pa]
sa_u=572e6;   % tensione rottura [Pa]
tau_y=331e6;  % tensione taglio [Pa]
kt_a=3;       % fattore concentrazione sforzi
% safety factor sf=2.5;
%% GEOMETRIA ATTACCHI
% interasse bulloni: calcolato come 1.5 volte l'altezza di ciascun
% longherone
v=1.3*[h1 h2 h3 h4 h5];     % [m]
h=[h1 h2 h3 h4 h5];         % altezze longheroni in vettore [m]
% forza trazione su bulloni [N]
F1=P1*h1/v(1);
F2=P2*h2/v(2);
F3=P3*h3/v(3);
F4=P4*h4/v(4);
F5=P5*h5/v(5);
P=abs([P1 P2 P3 P4 P5]);
F=abs([F1 F2 F3 F4 F5]);
% forza taglio su bulloni
S=Sy/5; % taglio totale ripartito equamente su ciascun attacco [N]
Sb=S/2; % taglio su ciascun bullone [N]
%% DIMENSIONAMENTO BULLONI
% [m2]
Ab1=sqrt(F(1)^2 + 3*(Sb)^2)/(sb_y/sf);
Ab2=sqrt(F(2)^2 + 3*(Sb)^2)/(sb_y/sf);
Ab3=sqrt(F(3)^2 + 3*(Sb)^2)/(sb_y/sf);
```

```
Ab4=sqrt(F(4)^2 + 3*(Sb)^2)/(sb_y/sf);
Ab5=sqrt(F(5)^2 + 3*(Sb)^2)/(sb_y/sf);
% [m]
D1=sqrt((4*Ab1)/pi);
D2=sqrt(4*Ab2/pi);
D3=sqrt(4*Ab3/pi);
D4=sqrt(4*Ab4/pi);
D5=sqrt(4*Ab5/pi);
D=[D1 D2 D3 D4 D5];
%% DIMENSIONAMENTO PIASTRE COLLEGAMENTO
% piastra con carico uniforme p(i)=F(i)/area e incastrata sui lati lunghi e
% su un lato corto
% lati a(i) pari alla larghezza di ciascun longherone e b(i)=(v(i)-h(i))/2
% larghezza piastra attacco = larghezza flangia  [m]
a=1e-3*[100 55 56 60 68];
e=1.5*D;                      % lunghezza bordo libero [m]
b=(v-h)/2 + e;                % altezza piastra [m]
p=F./(a.*b);                  % carico distribuito [Pa]
k=17;                         % coeff. vincoli piastra
for i=1:5
    px(i)=p(i)*(a(i)^4)/(k*b(i)^4+a(i)^4);
    py(i)=p(i)-px(i);
    my_max(i)=(px(i)*b(i)^2)/2;
    mx_max(i)=(py(i)*a(i)^2)/12;
    ta(i)=sqrt((6*max(mx_max(i),my_max(i)))/(sb_y/sf));
end
%% COLLEGAMENTO ATTACCO LONGHERONE
% dati rivetti: HI-LOCK 3/16 (rivetti in titanio Ti-6Al-4V usati per compositi)
D_b=4.763e-3;                        % diametro gambo [m]
su_b=950e6;                          % carico rottura rivetto [Pa]
sy_b=880e6;                          % carico snervamento rivetto [Pa]
tau_b=655e6;                         % taglio rivetto [Pa]
Fbmax=tau_b*pi*(D_b^2)/4;            % forza di taglio massima trasmessa dal rivetto [N]
f=[0.1 0.0275 0.028 0.03 0.068];     % larghezza flange [m]
% longheroni a T
n_b=round(P(2:4)/(2*Fbmax));               % numero bulloni su ciascuna fila
ts=P(2:4)./(2*(sa_y/sf)*(f(2:4)-D_b));     % spessore piastra giunzione
es=P(2:4)./(4*(tau_y/sf)*ts.*n_b);         % distanza foro-bordo libero
% longheroni a C
n_bc1=round(P(1)/2*Fbmax);            % numero bulloni longherone 1
n_bc5=round(P(5)/2*Fbmax);            % numero bulloni longherone 5
ts1=P(1)/((sa_y/sf)*(f(1)-D_b));      % spessore piastra giunzione 1
ts5=P(5)/((sa_y/sf)*(f(5)-D_b));      % spessore piastra giunzione 5
es1=P(1)/(2*(tau_y/sf)*ts1*n_bc1);    % distanza foro-bordo libero longherone 1
es5=P(5)/(2*(tau_y/sf)*ts5*n_bc5);    % distanza foro-bordo libero longherone 5
```

Bibliography

[1] (2015). Adamworks - composite structures from concepts to certification, [Online]. Available: `http://adamworksinc.com/`.

[2] L. B. Bush, J. C. Robinson, and D. M. Wahls, "Preliminary structural evaluation and design of the hl-20", *Journal of Spacecraft and Rockets*, vol. 30, no. 5, pp. 567–572, 1993.

[3] L. B. Bush, D. M. Wahls, and J. C. Robinson, "Hl-20 structural design comparison-conformal shell versus cylindrical crew compartment", in *AIAA/ASME/ASCE/AHS/ASC 34th Structures, Structural Dynamics, and Materials Conference*, 1993.

[4] C. F. Ehrlich, "Hl-20 concept: Design rationale and approach", *Journal of Spacecraft and Rockets*, vol. 30, no. 5, 1993.

[5] "Engaging the private sector in space exploration – an esa approach", in *Proc of IAC Space 2016 Conference & Exposition, Guadalajara, Mexico*, 2016.

[6] E. B. Jackson, R. A. Rivers, R. S. Chowdhry, W. Ragsdale, and D. W. Geyer, "Launch-pad abort capabilities of the hl-20 lifting body", 1994.

[7] R. C. Juvinall and K. M. Marshek, *Fundamentals of machine component design*. Wiley New York, 2011.

[8] Z. C. Krevor, R. D. Howard, T. Mosher, M. Sanchez, and J. Curry, "Achieving full ascent abort coverage with the dream chaser space system", in *Proc of AIAA Space 2011 Conference & Exposition, Long Beach, CA*, 2011.

[9] R. D. Launius and D. R. Jenkins, *Coming home: reentry and recovery from space*. Government Printing Office, 2012.

[10] H.-H. Lee, *Finite Element Simulations with ANSYS Workbench 17*. SDC publications, 2017.

[11] T. H. G. Megson, *Aircraft structures for engineering students*. Elsevier, 2012.

[12] D. R. Mulville, "Structural design and test factors of safety for spaceflight hardware", Technical Report NASA-STD-5001, NASA, Tech. Rep., 1996.

[13] K. Peter, "Ansys theory reference manual, release 5.6", *Ansys Inc*, 1994.

[14] R. D. Reed and D. Lister, *Wingless flight: the lifting body story*. University Press of Kentucky, 2015.

[15] T. P. Sarafin and W. J. Larson, "Spacecraft structures and mechanisms: From concept to launch", 1995.

[16] W. I. Scallion, "Aerodynamic characteristics and control effectiveness of the hl-20 lifting body configuration at mach 10 in air", 1999.

[17] E. Secretariat, "Space engineering structural factors of safety for spaceflight hardware", ECSS-E-ST-32-10C, European Cooperation For Space Standardization (ECSS), ESA-ESTEC, Noordwijk, The Netherlands, Tech. Rep., 2009.

[18] B. Spencer Jr, C. H. Fox, and J. K. Huffman, "A study to determine methods of improving the subsonic performance of a proposed personnel launch system (pls) concept", 1995.

[19] H. Stone and I. MacConochie, “Hl-20 subsystem design”, *Journal of Spacecraft and Rockets*, vol. 30, no. 5, 1993.

[20] T. A. Talay, “The hl-20 personnel launch system”, in *AIAA Space Programs and Technologies Conference, Huntsville, Ala*, 1992, pp. 24–27.

[21] F. W. Taylor, C. J. Allison, C. L. Lee, and K. R. Ibold, “Challenges and opportunities related to landing the dream chaser® reusable space vehicle at a public-use airport”, 2014.

[22] G. M. Ware, “Supersonic aerodynamic characteristics of a proposed assured crew return capability (acrc) lifting-body configuration”, *NASA Technical Memorandum 4136*, 1989.

[23] ——, “Transonic aerodynamic characteristics of a proposed assured crew return capability (acrc) lifting-body configuration”, *NASA Technical Memorandum 4117*, 1989.

[24] (2012). From hl-20 to dream chaser - the long story of a little spaceplane, [Online]. Available: `https://forum.nasaspaceflight.com/`.

[25] W. C. Young and R. G. Budynas, *Roark’s formulas for stress and strain.* McGraw-Hill New York, 2002, vol. 7.

View publication stats